MATEMATICKO-FYZIKÁLNÍ
FAKULTA
Univerzita Karlova

DISERTAČNÍ PRÁCE

RNDr. Michal Vališka

Magnetismus 5f-elektronů v intermetalických sloučeninách uranu

Katedra fyziky kondenzovaných látek

Vedoucí disertační práce: prof. RNDr. Vladimír Sechovský, DrSc.

Studijní program: Fyzika

Studijní obor: Fyzika kondenzovaných látek a materiálový výzkum

Praha 2018

FACULTY
OF MATHEMATICS
AND PHYSICS
Charles University

DOCTORAL THESIS

RNDr. Michal Vališka

5f-electron Magnetism in Intermetallic Uranium Compounds

Department of Condensed Matter Physics

Supervisor of the doctoral thesis: prof. RNDr. Vladimír Sechovský, DrSc.

Study programme: Physics

Specialization: Physics of Condensed Matter and Materials Research

Prague 2018

I declare that I carried out this doctoral thesis independently, and only with the cited sources, literature and other professional sources.

I understand that my work relates to the rights and obligations under the Act No. 121/2000 Sb., the Copyright Act, as amended, in particular the fact that the Charles University has the right to conclude a license agreement on the use of this work as a school work pursuant to Section 60 subsection 1 of the Copyright Act.

In Prague date 19.10.2018

RNDr. Michal Vališka

First of all I would like to thank very much to my supervisor prof. RNDr. Vladimír Sechovský, DrSc. for his helpful support, time, advice and indispensable guidance in my whole PhD study. I have benefited from valuable collaboration with my colleagues from Charles University. It was valuable experience to share office with Ing. Barbora Vondráčková and RNDr. Petr Opletal being not only my colleagues, always willing to help me with laboratory work, but also friends and advisers. Theoretical calculations in this work were done by doc. RNDr. Martin Diviš, CSc. whom I would like to thank for his support. Various experimental and other difficulties of this work would not be possible to overcome without the help of RNDr. Jan Prokleška, Ph.D., RNDr. Jaroslav Valenta, RNDr., Mgr. Martin Míšek, Ph.D., Milan Klicpera, Ph.D., RNDr. Jiří Prchal, Ph.D., Mgr. Petr Proschek, RNDr. Klára Uhlířová, Ph.D., RNDr. Jiří Pospíšil, Ph.D. and RNDr. Petr Doležal and head of our department prof. Mgr. Pavel Javorský, Dr. Tight connection with the group of prof. Hiroshi Amitsuka from Hokkaido University resulted in valuable and very friendly collaboration with Hiraku Saito, Ph.D., Chihiro Tabata, Ph.D. and Tatsuya Yanagisawa, Ph.D. who is also author of the high-field magnetization measurements at Dresden High Magnetic Field Laboratory. I would also like to thank prof. Dr. Frank Roelof de Boer for his critical reading of the thesis and to Ross Harvey Colman, Dr. for language corrections.

It was a great honor for me to be supervised by Paul Steffens, Ph.D. and Martin Böhm, Ph.D. during my stay at ILL Grenoble. Further great assistance during the neutron diffraction experiments at ILL was given to me by Anne Stunault, Ph.D., Oscar Ramon Fabelo Rosa, Ph.D., Bachir Ouladdiaf, Ph.D. and Stéphane Rols, Ph.D. Excellent assistance during the neutron-diffraction experiments was also given at HZB Berlin by Dr. Oleksandr Prokhnenko and Dr. Maciej Bartkowiak.

Last but not least, I would like to thank to my great family. It would be impossible to go through the whole journey of the doctoral study without the warm and safe environment of my close relatives. The highest acknowledgment belongs to my wife, daughter and mother being three most important women in my life.

Název práce: Magnetismus 5f-elektronů v intermetalických sloučeninách uranu

Autor: RNDr. Michal Vališka

Katedra / Ústav: Katedra fyziky kondenzovaných látek

Vedoucí disertační práce: prof. RNDr. Vladimír Sechovský, DrSc., KFKL

Abstrakt: Tato práce je zaměřená na studium magnetických vlastností tří různých sloučenin na bázi uranu obsahujících 5f elektrony ($U_4Ru_7Ge_6$, UAu_2Si_2 a UIrGe). V rámci této práce byly, za pomoci různých metod, připraveny vysoce kvalitní krystaly těchto sloučenin. Vlastnosti těchto systémů byly studovány různými objemovými metodami (magnetizace, měrné teplo, teplotní roztažnost, elektrický transport) a také neutronovým a rentgenovým rozptylem při širokém spektru vnějších podmínek (nízká teplota, vysoké magnetické pole, vysoký tlak). Kombinace těchto metod odhalila komplexní chování těchto systémů a pomohla sestrojit jejich magnetické fázové diagramy.

První studovanou sloučeninou je feromagnet $U_4Ru_7Ge_6$vykazující velmi nízkou magnetokrystalovou anizotropii, která je neočekávaná pro sloučeninu na bázi uranu. To se promítá do izotropní závislosti téměř všech měřených fyzikálních vlastností. Bylo zjištěno, že osa snadné magnetizace se mění v uspořádaném stavu a tento jev je spojen s anomáliemi v teplotní roztažnosti ukazující na možnou rhomboedrickou distorzi. Ta vede k vytvoření dvou odlišných pozic uranu s odlišným magnetickým momentem. Tato předpověď byla potvrzena teoretickými výpočty a pomocí polarizované neutronové difrakce. Rozdíl magnetických momentů na dvou odlišných uranových pozicích je způsoben malou změnou v jejich lokální symetrii.

Druhým případem studovaným v této práci je UAu_2Si_2. První monokrystal této sloučeniny vypěstovaný vůbec, nám umožnil osvětlit předchozí rozporuplné popisy vlastností této sloučeniny. Měření magnetizace, magnetostrikce kombinované s neutronovou difrakcí jasně potvrzuji základní stav v podobě nevykompenzovaného antiferomagnetu společně se slabou feromagnetickou složkou. Vysokopolní studie sledovaly fázovou hranici základního stavu ke trikritickému bodu, kde se fázový přechod mění z prvního druhu na druhý. Detailní měření teplotní roztažnosti odhalili pokles objemu v uspořádaném stavu společně s možnou distorzí bazální roviny původní tetragonální struktury.

Poslední část je věnována ortorhombickému antiferomagnetu na bázi uranu – UIrGe. Studium teplotní roztažnosti této sloučeniny odhalilo silně anizotropní změny mříže pro všechny tři základní směry pod Néelovou teplotou. Takřka nulová objemová změna vede k velmi slabé tlakové závislosti teploty uspořádání. Vnější magnetické pole aplikované podél osy c má významný efekt na strukturu antiferomagnetického základního stavu a vede k metamagnetickému přechodu. Néelova teplota této sloučeniny je silně potlačena pro vyšší pole a byly zde pozorovány známky přítomnosti trikritického bodu.

Klíčová slova: uranové sloučeniny, feromagnetismus, antiferomagnetismus, trikritický bod, anisotropie

Title: 5f-electron Magnetism in Intermetallic Uranium Compounds

Author: RNDr. Michal Vališka

Department: Department of Condensed Matter Physics

Supervisor: prof. RNDr. Vladimír Sechovský, DrSc., DCMP

Abstract: This thesis if focused on the study of magnetic properties of three different uranium-based 5f-electron compounds ($U_4Ru_7Ge_6$, UAu_2Si_2 and UIrGe). High quality single crystals of these systems were grown by various methods as a part of this work. Properties of these compounds were studied by multiple bulk methods (magnetization, specific heat, thermal expansion, electrical transport) and by neutron and x-ray diffraction under various external conditions (low temperature, high magnetic field, high pressure). Combination of these methods revealed complex behaviors of the systems and helped to construct their magnetic phase diagrams.

The first studied compound, $U_4Ru_7Ge_6$ is ferromagnet, that exhibits an extremely low magentocrystalline anisotropy, which is unexpected for uranium-based system. It is evidenced by very isotropic dependence of almost all measured physical quantities. It was found, that the magnetic easy axis is changed in the ordered state and such an effect is connected with anomalies in thermal expansion, pointing to a possible rhombohedral distortion. It leads to the creation of two different U sites with unequal magnetic moments. This prediction was confirmed by theoretical calculations and by polarized neutron diffraction. The difference of magnetic moments on two distinct U sites is caused by a small change in their local symmetry.

The second case investigated in this thesis is UAu_2Si_2. The first single crystals of this compound ever grown allowed us to shed more light on the previous inconsistent reports about its properties. Magnetization and magnetostriction measurements combined with neutron-diffraction experiments clearly confirm the uncompensated antiferromagnetic ground state together with the weak ferromagnetic component. High-field studies traced the phase boundary of the ground-state phase towards the tricritical point, where the transition changes from the first- towards the second-order type. Detailed thermal-expansion measurements revealed volume collapse in the ordered state together with the possible basal-plane distortion of the former tetragonal structure.

The last part is focused on the orthorhombic uranium-based antiferromagnet UIrGe. Thermal-expansion studies of this compound revealed strongly anisotropic lattice changes of all three principal axes of the unit cell below the Néel temperature. Its almost zero volume-change leads to very weak pressure dependence of the ordering temperature. An external magnetic field applied along the c axis has a strong effect on the antiferromagnetic ground-state structure and causes a metamagnetic transition. The Néel temperature of the compound is rapidly suppressed by higher fields, and signs for the presence of a tricritical point were also observed.

Keywords: uranium-based compound, ferromagnetism, antiferromagnetism, tricritical point, anisotropy

Contents

Part I
Introduction

Studies of f-electron systems belongs to the keystones of the actual condensed-matter research. The enormously broad set of their structural, magnetic and physical properties in general makes them ideal target both for experimental and theoretical work. Their most valuable experimental studies are typically performed on single crystals that makes the crystal growth an essential step of the research. Single crystals allows us to focus on anisotropy of the physical quantities and beside that enables higher sample-quality than polycrystalline materials. Typical bulk methods like specific-heat, electrical-transport, thermal-expansion or magnetization measurements can give detailed information about studied material, but their combination with appropriate microscopic experiments like neutron diffraction/scattering, x-ray diffraction/scattering or muon spin spectroscopy can help to finalize the overall picture and completely describe the studied case.

The present thesis reports experimental work using a broad set of bulk and microscopic measurements for detailed investigation of selected systems in the form of high-quality and well-characterized single crystals which were also prepared within the present work.

Two first systems, which have been selected as subjects of the current study ($U_4Ru_7Ge_6$ and UAu_2Si_2), have a common denominator in the form of the well known URu_2Si_2, that has attracted the attention of the scientific community for more than three decades. The first system, $U_4Ru_7Ge_6$, is in fact the closest, Ge analog of this famous compound. Nevertheless, the present study of $U_4Ru_7Ge_6$, being the first work focused on a single crystal of this compound, reveals that these two systems have only little in common. The physical properties of $U_4Ru_7Ge_6$ are exceptionally isotropic but not less interesting. On the other hand, the second case in the row, UAu_2Si_2, can be rightfully understood as a sister compound of URu_2Si_2. Results of various experiments in this study prove, that specially the high-field phase of URu_2Si_2 is very similar to the behavior of UAu_2Si_2. It has to be noticed, that there are still many interesting and unsolved questions in the physics of UAu_2Si_2 due to the long-lasting lack of single crystals of this compound and some of them are addressed in this thesis. The last uranium-based compound that was selected to be investigated within this thesis is UIrGe. Some of the older studies focused on the single crystals of this compound brought inconsistent magnetic phase diagrams. Detailed experiments, that were performed within this work, confirm the type of phase diagram from the latest studies and agree with the concept of a tricritical point. This phase point, that separates the first-order and second-order transition in the phase diagram, is suggested to be present also in the phase diagram of UAu_2Si_2.

The thesis is organized into five parts. This first part, revealing the general motivation and organization of the thesis, is followed by the theoretical background. That part brings a brief outlook of magnetism, magnetic interactions, types of magnetic ordering and magnetic phase transitions with a special focus on the $4f$- and $5f$-electron systems and particularly uranium-based compounds. The third part describes the

experimental techniques that were used within this thesis. It includes crystal-growth methods, sample-characterization approaches, neutron-scattering techniques and, finally, methods for the study of bulk properties. These experimental descriptions are supplemented by appropriate relations, models and equations that are typically used for the data treatment. The main fourth part contains the results of the present thesis. It is divided into three separate chapters, which correspond to the studies of the $U_4Ru_7Ge_6$, UAu_2Si_2 and UIrGe compounds. Each chapter has its own introduction, results and discussion section. A general discussion together with the conclusion and future plans of all studied cases are presented in the fifth last part.

Part II
Theoretical aspects

1 Basic concepts of magnetism

1.1 Magnetic moments of atoms

Magnetic moments of individual atoms arise from properties of their electrons. The position of each electron is given by the vector $\boldsymbol{r}$ and its motion is described by the momentum $\boldsymbol{p}$. It thus results in the orbital angular momentum $\boldsymbol{r} \times \boldsymbol{p}$. The electron also has its own spin angular momentum $\boldsymbol{s}$. The angular momentum of the whole atom is a sum of all angular moments of electrons from not fully occupied shells

$$\boldsymbol{L} = \frac{1}{\hbar} \sum_{i=1}^{Z} \boldsymbol{r_i} \times \boldsymbol{p_i} \,. \tag{1.1}$$

The corresponding total spin angular momentum $\boldsymbol{S}$ is the sum of individual momentum $\boldsymbol{s}$ from not fully occupied shells. For the atom, at first the nucleus can be treated as fixed and possible corrections can be accounted by perturbation theory. The electrons are fermions so the total many-particle wave function must be antisymmetric with respect to interchange of particles. Thus the effective single-particle wave functions should form Slater determinant. Using variational principle the Dirac-Hartree-Fock or density functional methods can be applied to obtain effective single-particle Hamiltonian.

In the absence of an external magnetic field, the Hamiltonian for an isolated atom can be written as

$$\widehat{\mathcal{H}_0} = \sum_{i=1}^{Z} \left(\frac{p_i^2}{2m_e} - \frac{p_i^4}{8m_e^3 c^2} + V_i \right) , \tag{1.2}$$

where $\frac{p_i^2}{2m_e}$ is the kinetic energy, $\frac{p_i^4}{8m_e^3c^2}$ is the relativistic kinetic-energy correction and V_i is the effective potential energy of the i^{th} electron including Darwin correction and spin-orbit interaction since we are dealing with heavy atoms like U, Ir and Au [1]. The Equation (1.2) is valid up to the order v^2/c^2.

Adding the influence of the external magnetic field $\boldsymbol{B}$ introduces two additional terms

$$\widehat{\mathcal{H}} = \widehat{\mathcal{H}_0} + \mu_B \left(\boldsymbol{L} + g\boldsymbol{S} \right) \boldsymbol{B} + \frac{e^2}{8m_e} \sum_{i=1}^{Z} \left(\boldsymbol{B} \times \boldsymbol{r_i} \right)^2 , \tag{1.3}$$

where g is the *g-factor* [2] and m_e the electron mass and the relativistic kinetic-energy from Equation (1.2) is neglected. The first additional term $\mu_B \left(\boldsymbol{L} + g\boldsymbol{S} \right) \boldsymbol{B}$ quantifies the magnetic moment of the atom itself and is called the *paramagnetic term*. μ_B is the Bohr magneton, that describes the magnetic moment of the electron. The last term $\frac{e^2}{8m_e} \sum_{i=1}^{Z} \left(\boldsymbol{B} \times \boldsymbol{r_i} \right)^2$ is called the *diamagnetic term*.

The atoms with unpaired electrons in the outer shell have L or S (or both) non-zero. The *paramagnetic term* reflects the existence of magnetic moments present even in zero external magnetic field. If a magnetic field is applied, it tends to align the magnetic moments in the paramagnetic system parallel to its direction. It can be expected, that a higher magnetic field will more easily align the moments and increase the magnetization. On the other hand, the thermal motion will decrease the alignment of the moments and lead to a reduction of the magnetization. In that sense, the magnetization should be proportional to the ratio $\frac{B}{T}$.

A quantum-mechanical and statistical-physics treatment of the second term in Equation (1.3) yields a magnetization according to to the so called Brillouin function in the form

$$B_J(y) = \frac{2J+1}{2J}\coth\left(\frac{2J+1}{2J}y\right) - \frac{1}{2J}\coth\frac{y}{2J}, \tag{1.4}$$

where $y = \frac{g_J \mu_B J \mu_0 H}{k_B T}$, g_J the Landé *g-factor* , J the total angular momentum quantum number and k_B the Boltzmann constant.

The magnetic susceptibility for $y \ll 1$ is inversely proportional to the temperature, which is expressed by Curie's law (1.5)

$$\chi = \frac{n\mu_0\mu_{\text{eff}}^2}{3k_B T} = \frac{C}{T} \tag{1.5}$$

where the proportionality is given by the effective moment

$$\mu_{eff} = g_J \mu_B \sqrt{J(J+1)} = \sqrt{\frac{3k_B C}{N_A \mu_0 \mu_B^2}}. \tag{1.6}$$

The susceptibilities mentioned above were not taking into account the contribution of conduction electrons. This has to be included when an ion is embedded in the metallic lattice. Each electron in the metal is polarized either spin-up or spin-down. When an external magnetic field is applied, the energy of the electron would be lowered or raised depending on the orientation of its spin with respect to the direction of the magnetic field. This is the basis of the so-called *Pauli paramagnetism*. The magnetization of this system is given as a difference between the number of spin-up $n_\uparrow$ and spin-down $n_\downarrow$ electrons with density of states at the Fermi level $g(E_F)$

$$M = \mu_B (n_\uparrow - n_\downarrow) = \mu_B^2 \mu_0 H g(E_F) . \tag{1.7}$$

It leads to an almost temperature independent susceptibility

$$\chi_P = \frac{M}{H} = \mu_B^2 \mu_0 g(E_F) . \tag{1.8}$$

The electrons in the unfilled shells of an atom can combine to give a non-zero spin ($\boldsymbol{S}$) and orbital ($\boldsymbol{L}$) angular momentum. For this case $(2S+1)(2L+1)$ possible combinations exist with different energies. In the case of non-negligible spin-orbit coupling the total angular moment $\boldsymbol{J}$ should be introduced. The lowest energy state, that will be the most favorable, can be obtained on the basis of three empirical rules - *Hund's rules*[2].

- The first one accents minimizing of the Coulomb energy expressed by the Pauli exclusion principle. Reduction of the Coulomb repulsion between the electrons is acquired by maximizing the quantum number of the *spin angular momentum* $\boldsymbol{S}$.

- The second rule points at the lowering of energy for the electrons with the same direction of rotation in the orbits. It can be expressed by reduction of the Coulomb repulsion that is achieved by maximizing the *orbital angular momentum* $\boldsymbol{L}$.

- Minimizing of the spin-orbit energy is a fundamental point of the third Hund's rule. It states, that $\boldsymbol{J}$ is equal to $|\boldsymbol{L}-\boldsymbol{S}|$ if the shell is less than half filled and $|\boldsymbol{L}+\boldsymbol{S}|$ for the shell filled more than half.

Hund's rules express the situation of Russell-Saunders or LS coupling, which is realized when the interatomic electrostatic interaction is stronger than the spin-orbit interaction. In heavy atoms the spin-orbit interaction may become stronger than the electrostatic interaction. Then j-j coupling or some intermediate coupling may occur. In case of j-j coupling the spin and orbital angular momentum of each electron couple separately and, consequently, a weaker electrostatic interaction couples the total angular angular momentum j of the electrons[2].

1.2 Exchange interactions

The formation of long-range magnetic ordering is governed by exchange interactions which correlate the magnetic moments. The exchange-interaction energy exceeds the energy of the thermal motion of the magnetic moments and, below some characteristic energy, long-range order takes place. The *exchange interactions* have to be treated as a quantum mechanical effect. They can be usually described by the Heisenberg Hamiltonian[2]

$$\widehat{\boldsymbol{\mathcal{H}}}_{\boldsymbol{ex}} = -\sum_{i,j} J_{ij}\boldsymbol{S}_i\boldsymbol{S}_j\,, \tag{1.9}$$

where J_{ij} is the exchange integral and $\boldsymbol{S_i}$ and $\boldsymbol{S_j}$ localized-magnetic-spin vectors.

They can be sorted into three different categories:

Direct exchange The first one, direct exchange, acts directly without the need for any kind of intermediary. This type of interaction is often present in the case of $3d$, $4d$, $5d$ or $5f$ elements (Fe, Co, Ni, some U compounds, etc.) where substantial overlap of the wave functions of neighboring magnetic ions is found. It leads to a resulting value of the exchange integral J_{ij} around $10^2 - 10^3\,\mathrm{K}$.

Indirect exchange - superexchange The indirect exchange (superexchange) is exchange interaction acting between non-neighboring magnetic ions while the interaction itself is via non-magnetic ions in between of them. The exchange integral in this case is typically lower and reaches value of approximately$1 - 100\,\mathrm{K}$. Similar to

the case of direct exchange, it can be observed in $3d$, $4d$, $5d$ and $5f$ compounds, but it is also present in the case of $4f$ compounds with p and d elements.

RKKY interaction In metals we meet a special type of indirect interaction called RKKY (after the authors of the theoretical description Ruderman, Kittel, Kasuya and Yosida)[3–5]. This type of interaction is mediated by polarized conduction electrons which interact with the magnetic moments of the $4f$ ions. The exchange integral is modulated with increasing distance r in oscillatory character described by equation the[2]

$$J_{\mathrm{RKKY}} \propto \frac{\cos(2k_{\mathrm{F}}r)}{r^3}\,, \tag{1.10}$$

where k_{F} is the radius of the Fermi surface. The indirect interaction has a much longer-range character than in the previous cases. It is a favorable interaction in the $4f$ metals and their intermetallics.

Dzyaloshinskii-Moriya exchange interaction The magnetic properties of some materials are strongly influenced by the antisymmetric Dzyaloshinskii-Moriya exchange interaction, which is generally described by a vector product formed by spins S_i and S_j of two magnetic ions

$$\widehat{\mathcal{H}}_{DM} = d_{ij}\,(S_i \times S_j) \tag{1.11}$$

with the so-called Dzyaloshinskii vector d_{ij}[6,7]. It was introduced by Dzyaloshinskii to explain the observation of a small net magnetization in a number of antiferromagnets, a phenomenon called weak ferromagnetism[8], which is due to a slight deviation of the sublattice magnetizations from antiparallel arrangement. Extending Anderson's theory of super-exchange, Moriya later found a microscopic mechanism due to spin–orbit interaction that is responsible for the interactions. They arise in certain groups of magnetic materials with low symmetry where the effects of coupling do not cancel.

1.3 Magnetic ordering

The presence of the exchange interactions between pairs of magnetic moments in the lattice leads to spontaneous long-range order. In principle, there are two basic types of the magnetic ordering that are discussed below. More complex types of magnetic ordering exhibit unique dependencies of their magnetic properties (susceptibilities, etc.) and have to be treated and described individually.

Ferromagnetism Ferromagnetism is characterized by spontaneous arrangement (in the simplest case parallel) of all moments leading to spontaneous magnetization.

This ordered state can be described by the exchange interaction playing the role of a so-called effective field. This is also denoted as the Weiss molecular field B_{mf}.

The strength of this field can be parameterized by the temperature independent constant λ there is a linear dependence of molecular field on the magnetization

$$\boldsymbol{B}_{\mathrm{mf}} = \lambda \boldsymbol{M}\,. \tag{1.12}$$

Now, the molecular field can be enlarged by the external magnetic field $\boldsymbol{B}_{\mathrm{e}}$ and the Curie law for the paramagnetic susceptibility from (Equation (1.5)) should be rewritten as

$$\chi = \frac{\mu_0 M}{(B_{\mathrm{e}} + B_{\mathrm{mf}})} = \frac{C}{T}\,. \tag{1.13}$$

So that

$$\chi = \frac{M}{\mu_0 B_{\mathrm{e}}} = \frac{C}{T - C\lambda}\,. \tag{1.14}$$

The temperature $C\lambda = \theta_{\mathrm{P}}$ is called the Weiss temperature. We can rewrite Equation (1.14) in the form of the well known Curie-Weiss law [2]

$$\chi = \frac{C}{T - \theta_{\mathrm{P}}}\,. \tag{1.15}$$

It describes the temperature dependence of the paramagnetic susceptibility above the ordering temperature. We can also define the modified Curie-Weiss law

$$\chi = \frac{C}{T - \theta_{\mathrm{P}}} + \chi_0\,, \tag{1.16}$$

where χ_0 represents a temperature-independent contribution to the paramagnetic susceptibility. In the case of simple ferromagnets, the paramagnetic Curie temperature $\theta_{\mathrm{P}} \approx T_{\mathrm{C}}$, the called Curie temperature. The typical temperature dependence of the spontaneous magnetization, paramagnetic susceptibility and inverse paramagnetic susceptibility for a ferromagnet are plotted in Figure 1.1.

Non-zero spontaneous magnetization is characteristic also for ferrimagnets, uncompensated antiferromagnets or weak ferromagnets (see the paragraph Dzyaloshinskii-Moriya exchange interaction).

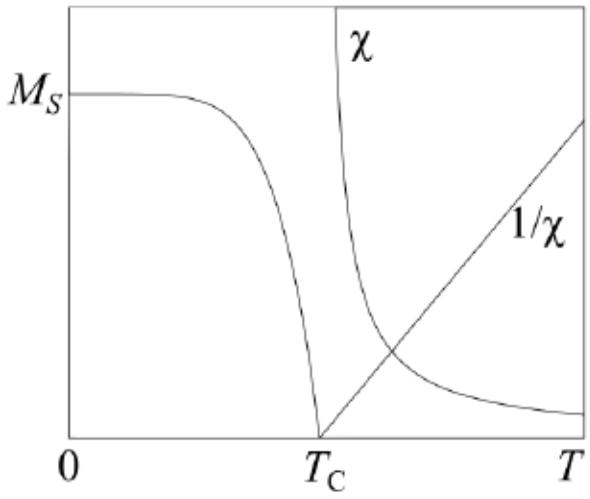

Figure 1.1: Temperature dependence of the susceptibility, inverse susceptibility and the spontaneous magnetization of a ferromagnetic material. T_C is the Curie temperature.

Antiferromagnetism The simplest antiferromagnetic order is characterized by an antiparallel alignment of the adjacent magnetic moments. This is established at temperatures below the Néel temperature (T_{N}). Such a simple antiferromagnet can be considered as being composed of two ferromagnetic and equivalent sublattices where the magnetic moments of one sublattice points up and of the second one down, being collinear. More complicated noncollinear periodic arrangements of magnetic moments can also result in zero spontaneous magnetic moment.

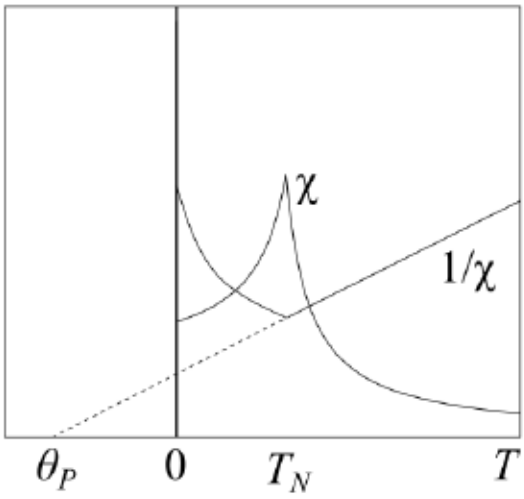

Figure 1.2: Temperature dependence of the susceptibility and inverse susceptibility of an antiferromagnetic material. θ_{P} is the Weiss temperature.

The typical temperature dependence of the magnetization and susceptibility for the antiferromagnet is plotted in Figure 1.2.

The relations for the susceptibilities of paramagnets, ferromagnets and antiferromagnets can be generalized by the general *Curie - Weiss law*

$$\chi \propto \frac{1}{T-\theta_{\mathrm{p}}}\,. \tag{1.17}$$

Paramagnets are usually characterized by $\theta_{\mathrm{p}}=0$, ferromagnets usually exhibit $\theta_{\mathrm{p}}>0$ with $\theta_{\mathrm{p}}\approx T_{\mathrm{C}}$ and antiferromagnets have typically $\theta_{\mathrm{p}}<0$ with $\theta_{\mathrm{p}}\approx -T_{\mathrm{N}}$. The actual relation between the Weiss temperature and the ordering temperature in materials is not as simple and straightforward. It strongly depends on the hierarchy of the exchange interactions in a particular case.

2 Magnetic ions in metals

2.1 Localized vs. itinerant magnetism

The relations derived in Section 1 for a free atom describe well the systems with well-localized d or f electrons. This approximation has its counterpart in the model for itinerant electrons. However, these concepts can be successfully applied only on a limited number of cases. Most of the actual systems lie in between these limits.

The localized model is well applicable on the majority of the $4f$-electron systems where the incomplete $4f$ shells are behind their magnetic properties. The outer s and d shells are involved in the chemical bonding. The localized nature of the magnetic moments leads to very good agreement of the real effective moments of $4f$ electron of rare earth ions in intermetallics with the values calculated values using Equation (1.6) with the total angular momentum J resulting from Hund's rules.

Itinerant-electron magnetism is ruled by the large overlap of charge distribution of neighboring atoms. This can be observed in the family of the d-electron transition metals, their compounds and also in some light actinides ($5f$ electron systems). Delocalization of the d (or f) electrons causes that they contribute both to the conductivity and to the chemical bonding. In the case of d-electron systems, wide energy bands are formed and they are occupied according to the Pauli exclusion principle. It can be shown, that under certain conditions, the spin-up and spin-down bands can spontaneously split, leading to the occurrence of ferromagnetism in the system. Moving electrons (from the energy level δE around the Fermi energy E_F) from the spin-up to the spin-down band will cost kinetic energy. Which will be equal to

$$\Delta E_k = g\left(E_\mathrm{F}\right)\delta E^2\,, \tag{2.1}$$

where $g\left(E_\mathrm{F}\right)$ is the density of states at the Fermi level. This action itself would be energetically unfavorable, but interaction of the arisen magnetization with the molecular field leads to an energy reduction connected with the modification of the exchange energy of

$$\Delta E_{exc} = Ug^2\left(E_\mathrm{F}\right)\delta E^2\,, \tag{2.2}$$

where U is the Coulomb parameter. Spontaneous splitting of the bands is then realized under the condition

$$\Delta E_k \leq \Delta E_{exc} \tag{2.3}$$

leading to the well-known Stoner criterion for ferromagnetism

$$Ug\left(E_F\right) \geq 1\,, \tag{2.4}$$

which is a measure whether spontaneous band splitting is energetically favorable and thus realized. If this criterion is not fulfilled, the susceptibility of the system will be

$$\chi_S = \frac{\mu_0\mu_\mathrm{B}^2 g\left(E_f\right)}{1 - Ug\left(E_f\right)} = \frac{\chi_P}{1 - Ug\left(E_F\right)}\,, \tag{2.5}$$

that is in fact the Pauli susceptibility (Equation (1.8)) enhanced by the enhancement factor $\frac{1}{1-Ug(E_F)}$. The Stoner model can partly explain the ferromagnetic order caused

by spontaneous spin-splitting. Details of the magnetic ordering will be discussed in the following chapters.

$3d$ transition metals can be taken as representatives of the itinerant magnetism. Nevertheless, pure itinerant electron magnetism is rare and hardly observed. Really close to this ideal state are for example $ZrZn_2$[9] or Ni_3Al[10]. In other actual materials a certain degree of localization exists and therefore has to be taken into account.

2.2 $5f$ electrons in uranium intermetallic compounds

In general, the magnetism of compounds containing $5f$ electrons is between the localized and itinerant description. Compounds containing lighter actinides show rather itinerant character of the $5f$ electrons and heavier actinides can be described better by localized $5f$ electrons.

The largest contrast between the lanthanide $4f$ states and the uranium $5f$ states is the spatial extent of the corresponding f-electron wave functions. It falls within the general trend of localization of electron states

$$5d < 4d < 3d < 5f < 4f\,. \tag{2.6}$$

This is governed by two major influences. The first one is the fact, that orbitals with higher principle quantum number contain more nodes and therefore are more delocalized. The second is the shift from d- to f-electron orbitals where the increased nuclear charge attracts the orbitals towards the nucleus. Combinations of these two trends are illustrated in the Kmetko-Smith diagram (Figure 2.1)[11,12].

Moving up and to the right in Figure 2.1 observes a trend of increased localization. This corner contains system with localized electrons usually leading to magnetic compounds. The bottom left side of the diagram is occupied by metals where highly itinerant d orbitals participate in the bonding and give rise to conventional superconductivity at low temperatures. The most interesting is the crossover region on the diagonal, which covers cerium and uranium materials and also iron-based superconductors.

As has already been mentioned, the $5f$ electrons of the uranium-based compound are delocalized, participate in the chemical bonding and considerably hybridize with the states of the neighboring atoms. This leads to the formation of a rather narrow $5f$ band (several eV) which is located at the Fermi energy (E_F). The typical high density of these $5f$ states at E_F is manifested in the enhanced value of the low-temperature specific-heat coefficient γ (explained in Equation (3.5)). The large hybridization results in highly anisotropic transport properties and the two-ion $5f-5f$ interaction gives rise to the typically strong magnetic anisotropy. Another effect of the delocalization of the $5f$ states is the low magnetic moment of U in the compounds compared to the free U^{3+} and U^{4+} moments.

The direct overlap of the $5f$ wave functions leads to the formation of a band, which is naturally controlled by the inter-uranium spacing d_{U-U}. Compounds, in which this key distance is small are often superconducting and these with larger d_{U-U} have typically a magnetic ground state. It demonstrates the "balancing" on the edge of the crossover region in the Kmetko-Smith diagram (Figure 2.1). The

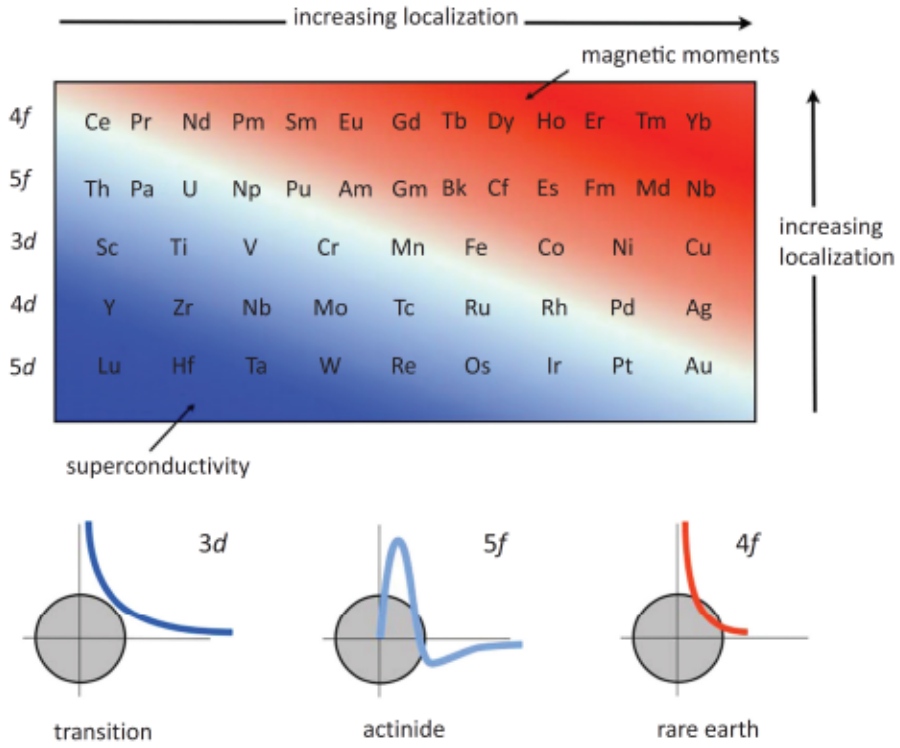

Figure 2.1: Kmetko-Smith diagram, showing the broad trends of increasing electron localization in d- and f-electron systems. After[11]

critical distance for $d_{\mathrm{U-U}}$ is called Hill limit[13] and is approximately 3.5 Å. Whether the system will have magnetic ground state or not is decided on the basis of the Stoner criterion Equation (2.4). The Coulomb interaction term U varies only little for the uranium-based intermetallics, since the number of the $5f$ electrons is always between 3 (U^{3+}) and 2 (U^{4+}). Therefore, the main influence comes from the density of states at E_F that is connected with the width of the $5f$ band itself (W_{5f}). The dependence of the bandwidth W_{5f} was shown to scale with the interatomic distance R as $W_{5f} \sim R^{-6}$(Ref.[14–16]) and reveals the origin of the sensitivity of the uranium-based compounds to pressure and alloying.

Nevertheless, there exist uranium-based compounds that have a non-magnetic ground state despite the fact that their $d_{\mathrm{U-U}}$ is larger than the Hill limit. For these systems, the hybridization of the $5f$ electrons with ligands plays dominant role[17,18].

The most striking difference between the itinerant $5f$ uranium and $3d$ transition-metal magnetism, otherwise similar, is the role of the spin-orbit interaction $E_{\mathrm{s-o}}$. While the energy width of the $3d$ band (W_{3d}) is much larger than $E_{\mathrm{s-o}}$ ($W_{3d} \gg E_{\mathrm{s-o}}$), W_{5f} is comparable to $E_{\mathrm{s-o}}$ ($W_{5f} \sim E_{\mathrm{s-o}}$). Such large spin-orbit interaction of the uranium-based compounds leads to the emergence of a large orbital magnetic moment that is antiparallel to the spin moment (as expected from Hund's rule)[19].

The typical common property of uranium-based compounds is their strong and anisotropic bonding of the magnetic moments to the crystallographic directions - *the magnetocrystalline anisotropy*. For the $4f$ systems, it can be understood as a

single-ion interaction with the crystalline field. The situation for the delocalized $5f$ electrons is different and can be described as a two-ion interaction with a dominant role of the strong spin-orbit interaction. In magnetically anisotropic systems, there exist a direction in which the applied external magnetic field leads to a rapid increase of magnetization - *the magnetic easy axis* - and a direction with small and linear response of the magnetization to the applied field - *the magnetic hard axis*. The intercept field of these two dependencies (typically extrapolated above the limit of the experimentally accessible range) is the estimation of the anisotropy field. This anisotropy field can reach very large values of the order of $10^2 - 10^3$ T[20–22] for uranium-based compounds. It was observed, that the direction of the magnetic easy axis depends on the direction of the shortest $d_{\mathrm{U-U}}$ distance. If this orientation is well defined in the structure, the magnetic easy axis is perpendicular to this direction. It leads to easy-axis anisotropy for the compounds with planar arrangement of the uranium ions (separated by $d_{\mathrm{U-U}}$) and to easy-plane anisotropy if the uranium ions form chains with inter-chain distance $d_{\mathrm{U-U}}$ and significantly larger intra-chain separation. This strong anisotropy is observed both in the ordered and the paramagnetic state of these compounds [22].

2.3 Magnetic phase transitions

One of the most straightforward approaches to treat phase transitions is the Landau concept of thermodynamic potentials[23]. Within the Landau theory, the thermodynamic potentials (mostly the free energy) are expanded in terms of powers of an order parameter. The order parameter is a function of temperature and by definition is zero in the high symmetry phase (disordered phase at high temperature) and nonzero in the ordered, lower symmetry phase below a certain critical temperature T_{c}. A typical example of the order parameter is the spontaneous magnetization of a ferromagnet.

According to Ehrenfest's classification scheme, the order of a phase transition is defined by the lowest discontinuous derivative of the free-energy function of the system. The first-order phase transition shows a discontinuity in the first derivative of the free energy, i.e. in the volume, entropy, magnetization etc. The change in entropy corresponds to the latent heat. The second-order phase transitions, also called continuous phase transitions, are discontinuous in the second derivative of the free energy. It means that they show step in the thermal expansion coefficients, compressibility, heat capacity, etc. This type of the phase transition is not connected with the presence of latent heat.

The physical quantities in the vicinity of the critical temperature T_{c} show some sort of so-called critical behavior. In terms of the reduced variable

$$t = \frac{T - T_{\mathrm{c}}}{T_c}, \tag{2.7}$$

it leads to various relations, for example

$$\begin{array}{c} C_V \sim |t|^{-\alpha} \\ M \sim |t|^{-\beta}\,,\; M \sim |\mu_0 H|^{1/\delta} \\ \chi \sim |t|^{-\gamma} \\ \xi \sim |t|^{-\nu} \end{array} \quad , \tag{2.8}$$

where C_V is the specific heat at constant volume, M the magnetization (also with the relation for the field dependence), χ the susceptibility and ξ the correlation length. The power law exponents α, β, γ, δ and ν are usually called critical exponents. It can be shown that, very close to the ordering temperature T_c (i.e. $|t| \to 0$), these exponents are bound together by a set of scaling relations [24]:

$$\begin{array}{c} \alpha + 2\beta + \gamma = 2 \\ \delta = 1 + \frac{\gamma}{\beta} \\ \nu \mathrm{d} = 2 - \alpha \end{array} \quad , \tag{2.9}$$

where d is the dimension of the system [25]. Various theoretical models predict the different critical exponents. Resulting values are listed in Table 2.1.

Table 2.1: Some values of the critical exponents for several theoretical models [25,26].

Model	α	β	γ	δ	ν
Mean field	0	1/2	1	3	1/2
Ising (2D)	0	1/8	7/4	15	1
Ising (3D)	0.11	0.325	1.240	4.816	0.630
Heisenberg (3D)	-0.115	0.365	1.387	4.803	0.705

The above mentioned phase transitions were treated on the basis of the temperature dependence. In this case the transition occurs when the temperature reaches a critical value - critical temperature T_c. In general, a phase transition can be realized when a different thermodynamic parameter (e.g., pressure, stress, magnetic field) is varied. Within the phase diagram defined by the set of these thermodynamic parameters, the usual critical point transforms to a critical line or even surface. The point where three critical lines come together is called the tricritical point (TCP) and is connected with a change of the order of the transition from first to second order [27,28].

3 Impact of magnetism on physical properties

3.1 Heat capacity and magnetic entropy

The heat capacity can be written as a sum of different contributions

$$C_{\mathrm{p}}(T) = C_{\mathrm{ph}}(T) + C_{\mathrm{el}}(T) + C_{\mathrm{mag}}(T) + \widetilde{C}\,, \tag{3.1}$$

where $C_{\mathrm{ph}}(T)$ is the lattice (phonon) contribution, $C_{\mathrm{el}}(T)$ the electron contribution and $C_{\mathrm{mag}}(T)$ the magnetic (magnon) contribution. The other contributions are included in the $\widetilde{C}$ term.

At low temperatures, the contribution of the lattice is well described by the Debye model. In this simplification, the crystal is treated as an isotropic elastic medium which allows collective modes (phonons) to propagate in it. These vibrations have a continuum of possible frequencies with a quadratic distribution up to some maximal limit called the Debye frequency ω_{D}, that can be translated to the Debye temperature $\Theta_{\mathrm{D}} = \frac{\hbar\omega_{\mathrm{D}}}{k_{\mathrm{B}}}$, where k_{B} is the Boltzmann constant. It leads to a lattice contribution of the heat capacity[29], that is expressed as

$$C_{\mathrm{ph}}(T) = 9N_{\mathrm{A}}k_{\mathrm{B}}\left(\frac{T}{\Theta_{\mathrm{D}}}\right)^3 \int_0^{\frac{\Theta_{\mathrm{D}}}{T}} \frac{e^x x^4}{\left(e^x-1\right)^2}\mathrm{d}x\,, \tag{3.2}$$

where N_{A} is the Avogadro constant. This integral gives the correct Dulong-Petit law of $C \approx 3k_{\mathrm{B}}N_{\mathrm{A}}$ for the high-temperature limit and, at low temperatures, it varies as T^3 which is usually simplified as

$$C_{\mathrm{ph}}(T) = \beta T^3,\ \beta = \frac{12\pi^4 N_{\mathrm{A}}k_{\mathrm{B}}}{5\Theta_{\mathrm{D}}^3}\,. \tag{3.3}$$

In contrast to the large contribution of the lattice to the heat capacity, only a small fraction of the electrons contributes to the $C_{\mathrm{el}}(T)$ term. As described by the Fermi-Dirac statistics, there is only limited number of electrons that have their energy within the interval of the thermal energy $k_{\mathrm{B}}T$ ($\approx 0.86\,\mathrm{meV}$ at $10\,\mathrm{K}$) around the Fermi energy E_{F} ($7\,\mathrm{eV}$ for coppera[29]). Thus it is only important at low temperatures, where the T^3-dependent term of the phonon contribution is also small. The electron contribution can be described as[29]

$$C_{\mathrm{el}}(T) = \frac{\pi^2 N_{\mathrm{A}}k_{\mathrm{B}}^2}{2E_{\mathrm{F}}}T = \frac{\pi^2}{3}D(E_{\mathrm{F}})\,k_{\mathrm{B}}^2 T = \gamma T\,, \tag{3.4}$$

where $D(E_{\mathrm{F}})$ is the density of states at the Fermi level and γ the Sommerfeld coefficient. As the Fermi energy E_{F} is inversely proportional to the effective mass of the electron m, it results in following relation

$$\gamma \sim m\,. \tag{3.5}$$

Above mentioned formalism can be used to approximate the low-temperature heat capacity of a non-magnetic metal by the simple equation

$$C_{\mathrm{p}}(T) = \gamma T + \beta T^3 \,. \tag{3.6}$$

The heat capacity of a magnetically ordered metal exhibits additional contribution from the magnons. As the dispersion relation of the magnons (quasiparticles representing the collective excitation of the magnetic moments) $\omega \sim k^m$ is quadratic ($m = 2$) for an isotropic ferro- and ferrimagnet and linear ($m = 1$) for the antiferromagnet[29], we can derive the general expression

$$C_{\mathrm{mag}}(T) \sim T^{\frac{3}{m}} \,. \tag{3.7}$$

Additional strong anisotropy can open an energy gap Δ and modify the dispersion relation. This gives an additional exponential term to the magnetic part of the heat capacity and results in

$$C_{\mathrm{mag}}(T) \sim \exp\left(-\frac{\Delta}{T}\right) T^{\frac{3}{m}} \,. \tag{3.8}$$

The last note should be devoted to the heat capacity of heavy-fermion (HF) compounds. In these systems the high density of states at the Fermi energy E_{F} leads to an electronic mass m^* which is enhanced by two or three orders and thus to an increased value of the Sommerfeld coefficient γ via Equation (3.5). In this sense, an increased γ is mostly taken as one of the most important experimental quantities to determine whether the compound is a HF system[30].

3.2 Thermal expansion and magnetostriction - magnetoelastic effects

The thermal expansion of a material can be expressed in the form of a relative length change (linear thermal expansion) of the sample $\frac{\Delta l_{sample}}{l}(T)$. Another way to express the resulting length change is the linear thermal expansion coefficient (thermal expansivity) α_i, where i marks the defined (crystallographic) direction along which is being measured. This value is related to the slope of the relative-length-change curve and accordingly is defined as its temperature logarithmic derivative

$$\alpha_i(T) = \frac{1}{l}\frac{\mathrm{d}l(T)}{\mathrm{d}T} \,. \tag{3.9}$$

The volume thermal expansion $\frac{\Delta V}{V}(T)$ or the volume thermal expansion coefficient $\alpha_v(T)$ can be (under some assumptions) calculated from the measured set of three orthogonal linear thermal expansions, or three linear thermal expansion coefficients, labeled as a, b and c. These directions are usually chosen as the main crystallographic directions of the unit cell. The important assumption is that all the length changes are small for the applied small temperature changes. The general expressions are thus valid for an orthorhombic system and can be written as follows

$$\frac{\Delta V}{V}(T) \approx \left\{\frac{\Delta l}{l}\right\}_a (T) + \left\{\frac{\Delta l}{l}\right\}_b (T) + \left\{\frac{\Delta l}{l}\right\}_c (T) \,, \tag{3.10}$$

$$\alpha_v(T) \approx \alpha_a(T) + \alpha_b(T) + \alpha_c(T) \,, \tag{3.11}$$

and can be simplified for the cubic system to

$$\frac{\Delta V}{V}(T) \approx 3\left\{\frac{\Delta l}{l}\right\}_a(T) \,, \tag{3.12}$$

$$\alpha_v(T) \approx 3\alpha_a(T) \,, \tag{3.13}$$

and for the tetragonal system to

$$\frac{\Delta V}{V}(T) \approx 2\left\{\frac{\Delta l}{l}\right\}_a(T) + \left\{\frac{\Delta l}{l}\right\}_c(T) \,, \tag{3.14}$$

$$\alpha_v(T) \approx 2\alpha_a(T) + \alpha_c(T) \,. \tag{3.15}$$

In a similar way as for the heat capacity, the volume thermal expansion coefficient $\alpha_v(T)$ can be expressed at low temperatures as a sum of an electronic and a lattice contribution [31]

$$\alpha_v(T) = aT + bT^3 \,. \tag{3.16}$$

Volume changes can be also induced by applying an external magnetic field. For itinerant systems this effect - magnetostriction - can be expressed by the simple formula [32]

$$\frac{\Delta V}{V} = \kappa C_{ME} M^2 \,, \tag{3.17}$$

where C_{ME} is the magnetoelastic-coupling constant, M magnetization and κ compressibility.

Ehrenfest and Clausius-Clapeyron relation

There exist thermodynamic relations describing the slope of the phase-transition boundaries in the pressure-temperature phase diagram of a system. They are known as the Ehrenfest relation for the second-order phase transition and the Clausius-Clapeyron relation for the first-order phase transition.

As was shown above, there is a discontinuity (step) in the entropy ΔS and the volume change ΔV at the transition temperature T_c of a first-order phase transition. The uniaxial pressure p_i dependence for the direction i of the transition at T_c should follow the equation

$$\frac{\mathrm{d}T_c}{\mathrm{d}p_i} = V_m \frac{\left\{\frac{\Delta l}{l}\right\}_i}{\Delta S} \,, \tag{3.18}$$

where V_m is the molar volume, $\left\{\frac{\Delta l}{l}\right\}_i$ the relative length change along the direction i and ΔS the change of the entropy connected with the transition.

As there are no discontinuities for neither the entropy nor the length change at the second-order phase transition, their temperature derivatives are used in the Ehrenfest relations. It is namely the step in the reduced heat capacity $\Delta C_p/T$ and in the

linear thermal expansion coefficient $\Delta\alpha_i$ that helps to estimate the uniaxial pressure dependence of the second-order phase transition temperature by the equation

$$\frac{\mathrm{d}T_\mathrm{c}}{\mathrm{d}p_i} = V_m \frac{\Delta\alpha_i}{\Delta\left(C_\mathrm{p}/T\right)} \,. \tag{3.19}$$

The hydrostatic pressure dependence of the transition temperatures can be obtained as the sum of the three orthogonal uniaxial pressure contributions estimated by Equation (3.18) and Equation (3.19) or by using the relative volume change (volume thermal expansion coefficient) in Equation (3.10) instead of the single relative length change (linear thermal expansion coefficient).

3.3 Electrical resistivity and magnetoresistance - conduction-electron scattering

The resistivity of a material is influenced by various types of scattering processes of the conduction electrons. If the mechanisms that describe these scattering events are independent, then the total resistivity can be written as sum of the corresponding individual resistivity contributions. This principle is known as Matthiessen's rule [29] and is expressed by the following equation

$$\rho(T)_\mathrm{total} = \rho_0 + \rho_\mathrm{ph}(T) + \rho_\mathrm{mag}(T) \,, \tag{3.20}$$

where ρ_0 is the temperature independent residual resistivity that corresponds to the scattering of the conduction electrons on lattice imperfections (defects, impurities, etc.). As the remaining terms in the simplified Matthiessen rule scale with temperature, the resistivity of a metal in the $0\,\mathrm{K}$ limit should be equal to ρ_0. In that sense it, can be used as a rough index of the overall quality of the sample. In practice also the dimensionless residual resistivity ratio (RRR) is widely used. It is defined as

$$\mathrm{RRR} = \frac{\rho_{300\,\mathrm{K}}}{\rho_\mathrm{LT}} \,, \tag{3.21}$$

where $\rho_{300\,\mathrm{K}}$ is the resistivity of the material at $300\,\mathrm{K}$ (room temperature) and $\rho_\mathrm{LT} \sim \rho_0$ the resistivity at the lowest measured temperature (typically about $2\,\mathrm{K}$, or in mK range for more precise experiments).

The next term in Equation (3.20), ρ_ph, describes the scattering processes between the conduction electrons and phonons. It can be described using the Debye model in a similar way as for the phonon contribution to the heat capacity in Equation (3.2). In the high-temperature limit (i.e., $T \gg \Theta_\mathrm{D}$, where Θ_D is the Debye temperature defined in the Section 3.1) it scales as

$$\rho_\mathrm{ph}(T) \sim C_{EP} T \,, \tag{3.22}$$

where C_{EP} is the electron-phonon-coupling constant. It can be derived that, in the low-temperature limit ($T \ll \Theta_\mathrm{D}$), the phonon scattering term varies as

$$\rho_\mathrm{ph}(T) \sim C T^5 \tag{3.23}$$

known as Bloch's T^5 law[29].

The magnetic contribution ρ_{mag} to the total resistivity in Equation (3.20) is temperature independent in the high-temperature paramagnetic limit and is called the spin-disorder resistivity. It is proportional to the de Gennes factor [33,34] via the relation

$$\rho_{\mathrm{mag}} \sim (g-1)^2 J(J+1)\,, \tag{3.24}$$

where g is the Landé factor and J is the total angular momentum[2].

The temperature dependence of the magnetic contribution to the total resistivity in the ordered state is no longer constant and describes the scattering of the conduction electrons on the magnons. The different character and dispersion relation of magnons (see Section 3.1) in ferromagnets and antiferromagnets leads to a different temperature dependence of ρ_{mag} below the Curie temperature (T_{C}) or the Néel temperature (T_{N}), respectively. If there is no gap in the dispersion relation of the magnons, then electrical resistivity of a ferromagnet varies as $\rho_{\mathrm{mag}}(T) \sim T^2$ and for an antiferromagnet holds $\rho_{\mathrm{mag}}(T) \sim T^4$. In the case of gapped dispersion, more general expression was deduced by Andersen and Smith [35]

$$\rho_{\mathrm{mag}}(T) = aT^2 + bT\left(1+\frac{2T}{\Delta}\right)\exp\left(-\frac{\Delta}{T}\right)\,, \tag{3.25}$$

where a and b are scaling parameters and the gap Δ corresponds to the one in the magnetic contribution to the heat capacity in Equation (3.8).

The electrical resistivity of the uranium intermetallic compounds is not dominated by electron-phonon scattering as in the analogous rare-earth intermetallics. An important role in uranium-based systems is played by the strong coupling of electrons to spin fluctuations and consequently their strong scattering, which is incoherent at high temperatures. It is manifested by a relatively high resistivity at room temperature (even larger than $200\,\mu\Omega\mathrm{cm}$)[36]. Once the system enters the coherent regime (below the characteristic temperature T_{coh}) the resistivity usually decreases significantly.

Most uranium-based intermetallics exhibit Fermi-liquid behavior in the low-temperature limit. It is manifested by a $\rho\,(T) - \rho_0 = aT^2$ dependence. The parameter a is enhanced compared to simple metals and scales with the square of Sommerfeld gamma coefficient γ^2 (Equation (3.5)) . This results in the universal Kadowaki-Woods ratio $\frac{a}{\gamma^2} \approx 1 \cdot 10^{-5}\,\mu\Omega \cdot \mathrm{cm} \cdot \mathrm{K}^2 \cdot \mathrm{mol}^2 \cdot \mathrm{mJ}^{-2}$[37] for heavy-fermion compounds.

Complex scattering mechanisms in uranium-based intermetallics often lead to non-additivity of the individual temperature-dependent terms. In this case, the simplified picture of Matthiessen's rule is not valid (Equation (3.20)). Field-induced metamagnetic transitions in uranium-based compounds are typically connected with large anomalies in the magnetoresistance dependencies as the antiferromagnetic correlations are suppressed and the different periodicity of the lattice alters the scattering of the electrons in the material.

Part III
Experimental techniques in use

4 Crystal growth and characterization, sample preparation

The investigation of the anisotropic properties of materials can be performed on good-quality single crystals. Single crystals typically bring more advantages than only availability to study anisotropic properties. Their periodic long-range arrangement usually goes hand in hand with phase purity, uniformity of composition, lack of grain boundaries, etc. There is a long list of various crystal-growth methods which are used both in the condensed-matter physics and industry. The following two methods were used for the preparation of the single crystals within this study. Precise verification of the correct composition and determination of the crystal structure of the sample is an essential step in condensed-matter research. The structure and proper composition of the measured samples was characterized by the methods mentioned in this chapter.

4.1 Czochralski method - growth of $U_4Ru_7Ge_6$ and UIrGe single crystals

The Czochralski method is based on pulling a rod with a seed, which was initially immersed in the melt, upwards from the melt and rotating it at the same time. Usually, a sizable single-crystalline cylindrical ingot is extracted from the melt when properly controlling temperature, the rate of pulling and the speed of rotation. By rule, single crystals of congruently melting materials can be grown by Czochralski method. A tri-arc furnace[1] that was prior to the growth evacuated to the vacuum of about 10^{-6} mbar and consequently filled with inert Ar gas was used for the growth.

The $U_4Ru_7Ge_6$ single crystal was grown from the constituent elements (purity of Ru 99.95% and Ge 99.9999%). The uranium metal was purified using the *Solid State Electrotransport* technique (*SSE*)[2] [38]. The pulling speed during the growth was $3 - 5\,\mathrm{mm \cdot h^{-1}}$ and the resulting ingot with proper scale can be seen in Figure 4.1.

Half of the crystal was wrapped in Ta foil (purity 99.99%), sealed in a quartz tube under a vacuum of about 10^{-6} mbar and annealed at 1000 °C for 7 days.

The single crystal of UIrGe was also grown by the Czochralski method in a tri-arc furnace from the constituent elements (purity of Ir 99.99% and Ge 99.9999%). The uranium metal was purified in the same way as for the previous material using the *SSE* method [38]. The pulling speed during the growth varied in the interval of $5 - 10\,\mathrm{mm \cdot h^{-1}}$ and the resulting ingot with proper scale can be seen in Figure 4.1.

[1] https://mgml.eu/instruments-technology/mgcl#3-arc-furnace-for-modified-czochralski-method

[2] https://mgml.eu/instruments-technology/mgcl#solid-state-electrotransport-sse

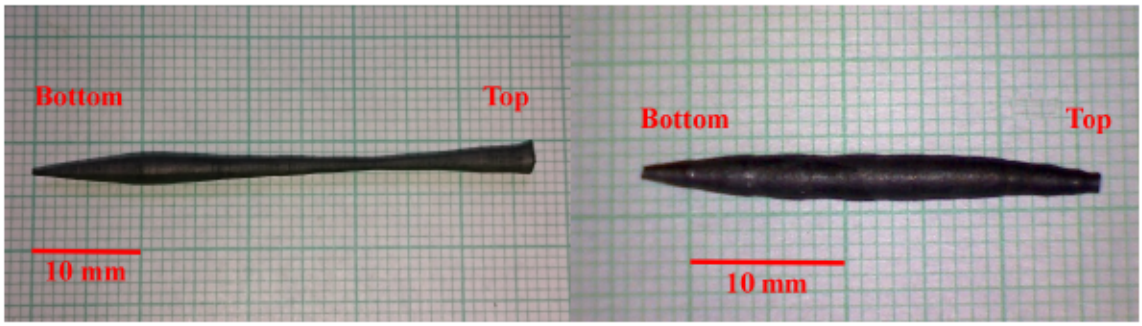

Figure 4.1: Photo of the as-grown singles crystal of $U_4Ru_7Ge_6$ (left) and UIrGe (right) in the tri-arc furnace.

The crystal was wrapped in Ta foil (purity 99.99%), sealed in a quartz tube under a vacuum of about 10^{-6} mbar, and annealed at 1000 °C for 10 days.

4.2 Floating-zone method - growth of UAu_2Si_2 single crystals

The arrangement of the floating-zone method in an optical furnace is as follows. A feed rod of the starting polycrystalline material hangs from the top and the seed rod of the same material is placed below - properly aligned along one common vertical axis. The light from the halogen lamps is properly focused to one point on this vertical axis (initially in between the feed and the seed rod) by four ellipsoidal mirrors. Both rods are moved towards the hot zone and are melted as light of the sufficient intensity is absorbed by the material. Consequent pulling down of the both rods leads to gradual melting of the feed rod and formation of the grown ingot below the hot zone. The whole growth is performed under protective Ar atmosphere.

The UAu_2Si_2 single crystal used in this study was prepared using the floating-zone method in an optical furnace (FZ-T-4000-VI-VPM-PC, Crystal Systems corp.[3]) in a similar way as in Ref. [39]. Nevertheless, to obtain higher-quality and larger single crystals, the entire growth process was optimized. The initial polycrystalline rod with diameter of 6 mm and length of about 100 mm was prepared from the starting elements of U (initially 99.9% and purified by the Solid State Electrotransport method under ultra high vacuum[38]), Au (99.99%) and Si (99.999%). The rod was annealed at 1000°C for three days, cut into two parts and placed in the optical furnace, where the shorter bottom part served as polycrystalline seed and the main larger rod hung from the top as feed material for the growth. The chamber of the optical furnace was evacuated to about 10^{-6} mbar and the growth itself was done under protective Ar atmosphere with a flow of $1.5\,\mathrm{l}\cdot\mathrm{min}^{-1}$ at an overpressure of about 0.2 MPa. The power of the lamps in the furnace was adjusted to keep the temperature of the hot zone slightly above the melting point. Both, the seed and feed rod, were slowly pulled through the hot zone with a speed of $1\,\mathrm{mm}\cdot\mathrm{h}^{-1}$ and without rotation. A photo of the growth process is in Figure 4.2.

[3] https://mgml.eu/instruments-technology/mgcl#optical-floating-zone-furnace-crystal-systems-corp-japan

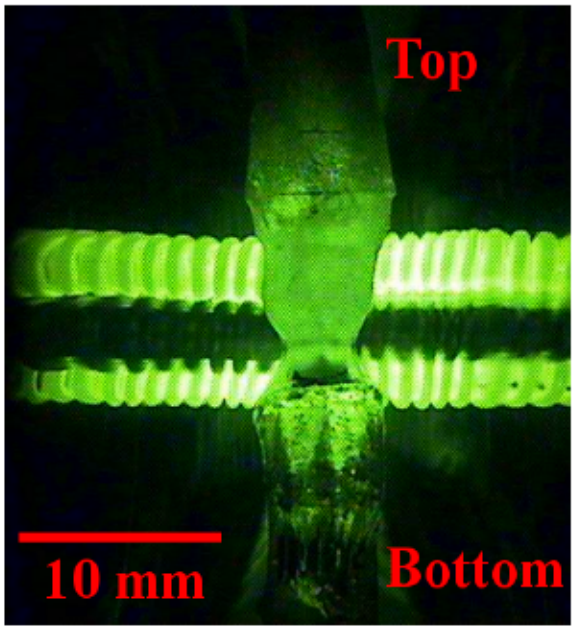

Figure 4.2: Photo of the growth of a single crystal of UAu_2Si_2 in the optical furnace.

4.3 Crystal-structure analysis by X-ray diffraction

The quality of the grown crystals was verified by Laue diffraction using a Photonic Science x-ray Laue system with a CCD camera and single crystal X-ray diffraction on a Rigaku R-Axis Rapid II diffractometer with a Mo anode.

Parts of all single crystals were pulverized and characterized by X-ray powder diffraction (XRPD) at room temperature on a Bruker AXS D8 Advance diffractometer with Cu anode. The XRPD data were evaluated by the Rietveld technique [40] using FULLPROF/WINPLOTR software [41,42].

$U_4Ru_7Ge_6$

The orientation of the $U_4Ru_7Ge_6$ single crystal was determined by the Laue method. Representative Laue pictures for the [100] and [111] direction are presented in Figure 4.3.

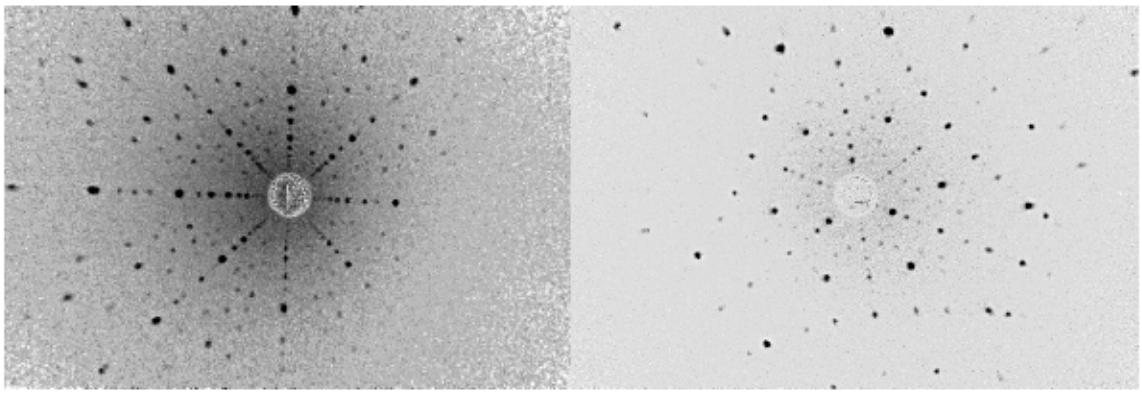

Figure 4.3: Laue pictures of the $U_4Ru_7Ge_6$ single crystal with orientation perpendicular to the [100] (left) and [111] direction (right).

Rietveld refinement of the XRPD data collected on both the pulverized as-cast and annealed single crystal confirmed previous reports[43–45] that $U_4Ru_7Ge_6$ possesses at room temperature a cubic crystal structure of the $Im\bar{3}m$ space group (see Figure 4.4). The room-temperature powder pattern is shown in Figure 4.5. The corresponding lattice parameters (see Table 4.1) determined for both the as-cast and the annealed crystal are nearly identical. The coordination of the U atoms in the $U_4Ru_7Ge_6$ structure is a slightly distorted cuboctahedron[46] and the $U - Ru_1$ distance (2.932 Å) is shorter than the closest $U - U$ distance (4.147 Å).

Table 4.1: Results of structure analysis of $U_4Ru_7Ge_6$ at room temperature.

Space group $Im\bar{3}m$	as-cast	annealed
a	8.2934(2) Å	8.2933(3) Å
U(x, y, z), 8c	(0.25, 0.25, 0.25)	(0.25, 0.25, 0.25)
$Ru_1(x, y, z)$, 12d	(0.25, 0, 0.5)	(0.25, 0, 0.5)
$Ru_2(x, y, z)$, 2a	(0, 0, 0)	(0, 0, 0)
Ge(x, y, z), 12e	(0.31375(13), 0, 0)	(0.31360(11), 0, 0)

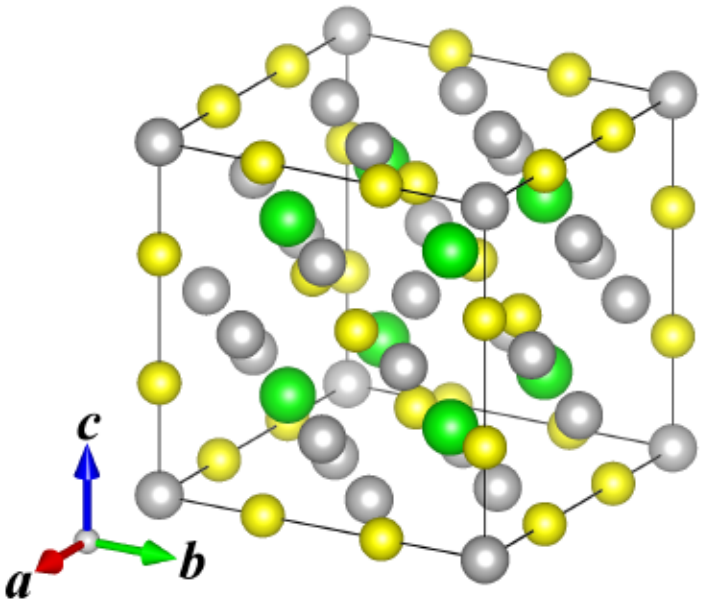

Figure 4.4: Structure of $U_4Ru_7Ge_6$ with the $Im\bar{3}m$ space group U ions are green, Ru gray and Ge yellow.

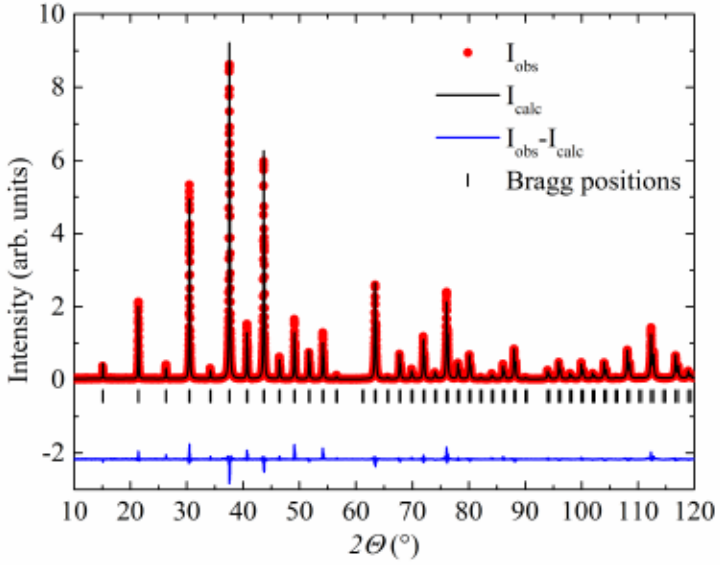

Figure 4.5: X-ray powder-diffraction pattern of an as-cast pulverized $U_4Ru_7Ge_6$ single crystal measured at room temperature.

UAu_2Si_2

The proper orientation of the UAu_2Si_2 sample was determined by the Laue method. Representative Laue pictures for the [100] and [001] direction can be seen in Figure 4.6.

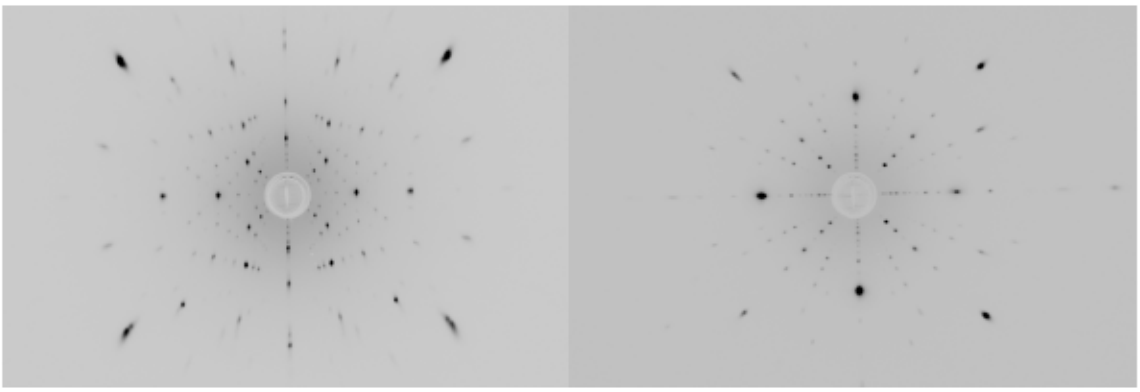

Figure 4.6: Laue pictures of the UAu_2Si_2 single crystal with orientation perpendicular to the [100] (left) and [001] direction (right).

The Rietveld refinement of the XRPD data at room temperature of the pulverized part of the UAu_2Si_2 single crystal show expected $I4/mmm$ space group (see Figure 4.7) in agreement with the previous reports [39,47–52] and no additional phases were observed.

Table 4.2: Results of structure analysis of UAu_2Si_2 at room temperature.

Space group $I4/mmm$	
a	4.2220(1) Å
c	10.2779(3) Å
U(x, y, z), $2a$	(0, 0, 0)
Au(x, y, z), $4d$	(0.5, 0, 0.25)
Si(x, y, z), $4e$	(0.3916(8), 0, 0)

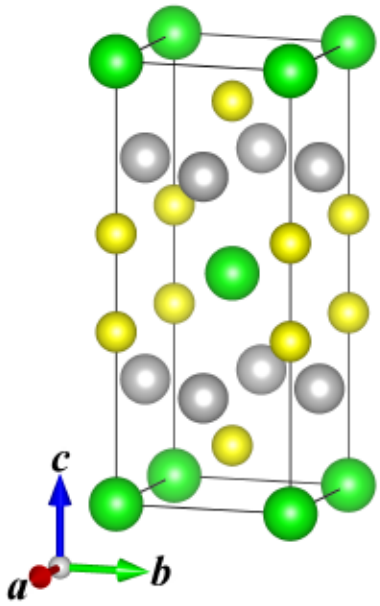

Figure 4.7: Structure of UAu_2Si_2 with the $I4/mmm$ space group U ions green, Au gray and Si are yellow.

The pattern is plotted in Figure 4.8. The obtained structural parameters are summarized in Table 4.2.

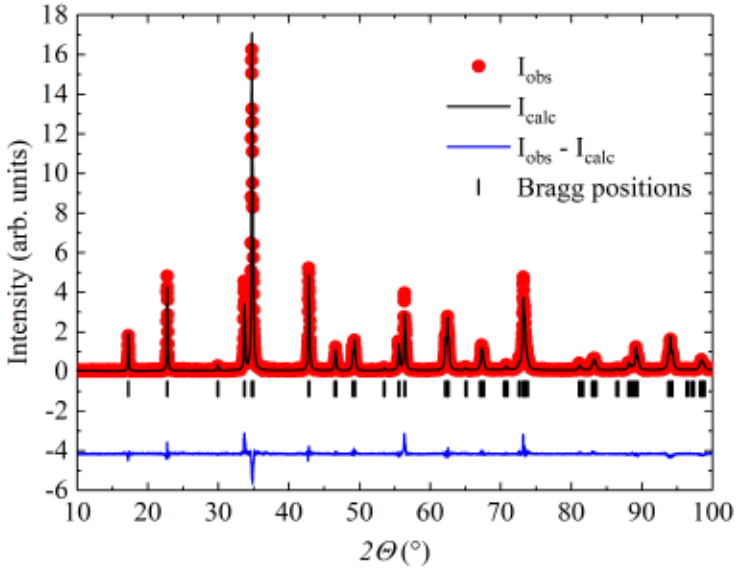

Figure 4.8: X-ray powder-diffraction pattern of a pulverized UAu_2Si_2 single crystal measured at room temperature.

UIrGe

The proper orientation of the single-crystalline sample was determined by Laue method. Representative Laue pictures for the [010] and [001] direction are presented in Figure 4.9.

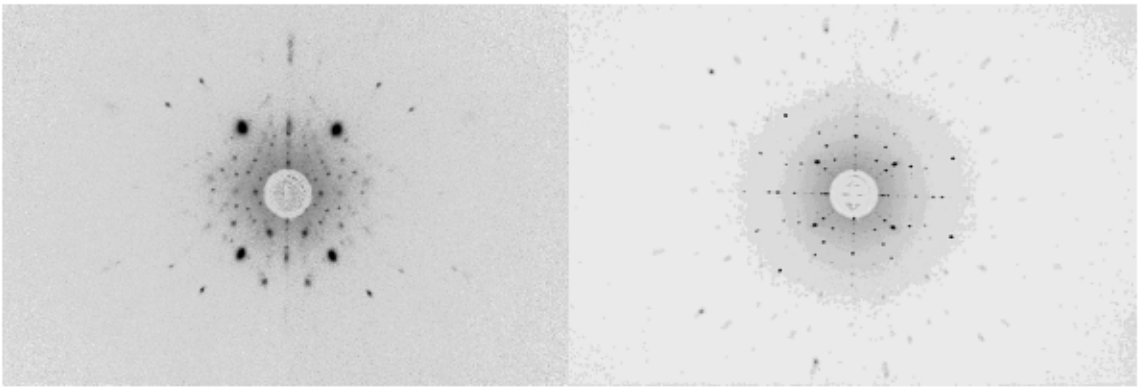

Figure 4.9: Laue pictures of the **UIrGe** single crystal with orientation perpendicular to the [010] (left) and [001] direction (right).

The refined XRPD data obtained at room temperature show the expected structure of **UIrGe** with space group *Pnma* (see Figure 4.10) as reported in Ref.[53]. No additional phases were observed in the measured patterns.

Table 4.3: Results of structure analysis of UAu_2Si_2 at room temperature.

Space group *Pnma*	
a	6.8694(2) Å
b	4.3025(1) Å
c	7.5762(2) Å
U(x, y, z), 4c	(0.0067(4), 0.25, 0.7030(2))
Ir(x, y, z), 4c	(0.2802(3), 0.25, 0.4142(4))
Ge(x, y, z), 4c	(0.1861(6), 0.25, 0.0889(8))

The measured pattern together with refined profile is plotted in Figure 4.11. The Resulting structural parameters are summarized in Table 4.3.

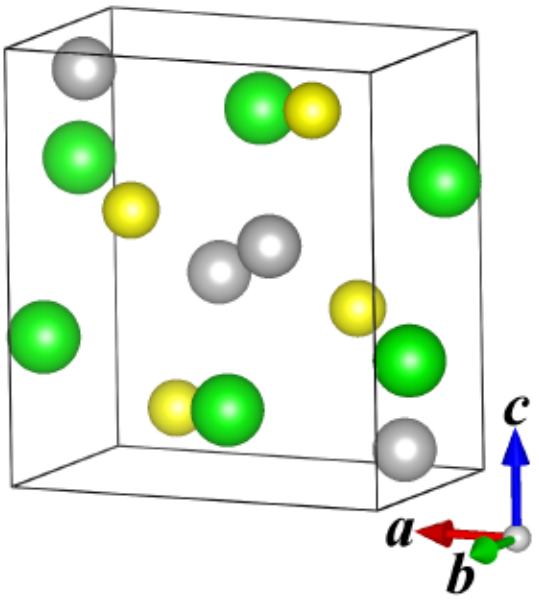

Figure 4.10: Structure of UIrGe with the *Pnma* space group with U ions green, Ir gray and Ge yellow

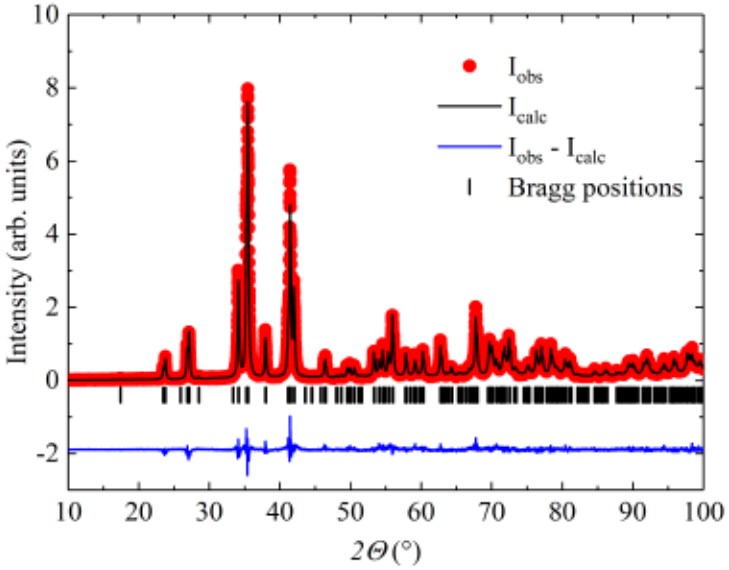

Figure 4.11: X-ray powder-diffraction pattern of a pulverized UAu_2Si_2 single crystal measured at room temperature.

4.4 Energy dispersive x-ray analysis of sample composition

The chemical composition of each single crystal was verified in a scanning electron microscope (SEM) Tescan Mira I LMH equipped with an *Energy Dispersive X-ray* (EDX) detector Bruker AXS inspecting the signal both of the secondary and back-scattered electrons.

$U_4Ru_7Ge_6$

Elemental mapping by EDX confirms the homogeneity of all studied samples of $U_4Ru_7Ge_6$ (see Figure 4.12). The average of multiple point scans from different parts of the sample gave the resulting stoichiometry 4.4(4):6.9(2):5.7(1), pointing to a slight Ge deficiency.

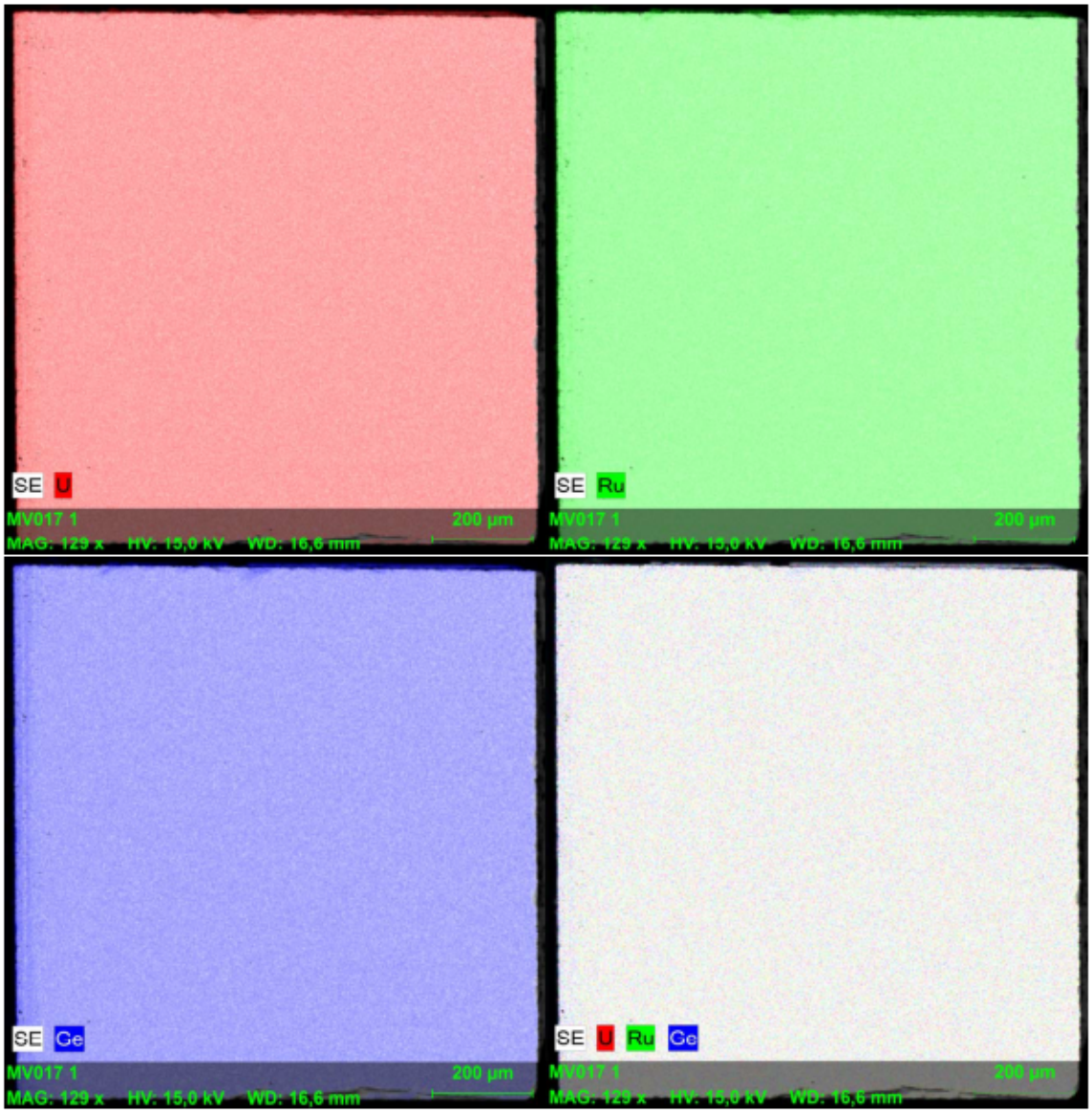

Figure 4.12: Surface of the $U_4Ru_7Ge_6$ single crystal studied by EDX analysis with individual elemental mappings (U - red, Ru - green and Ge - blue). The scale bar (200 μm) is in the bottom right corner of each image.

UAu_2Si_2

EDX reveals homogeneity of the sample shaped from the UAu_2Si_2 single crystals. The individual elemental mapping is shown in Figure 4.13. The average stoichiometry was 1.1(1):1.9(1):2.0(2).

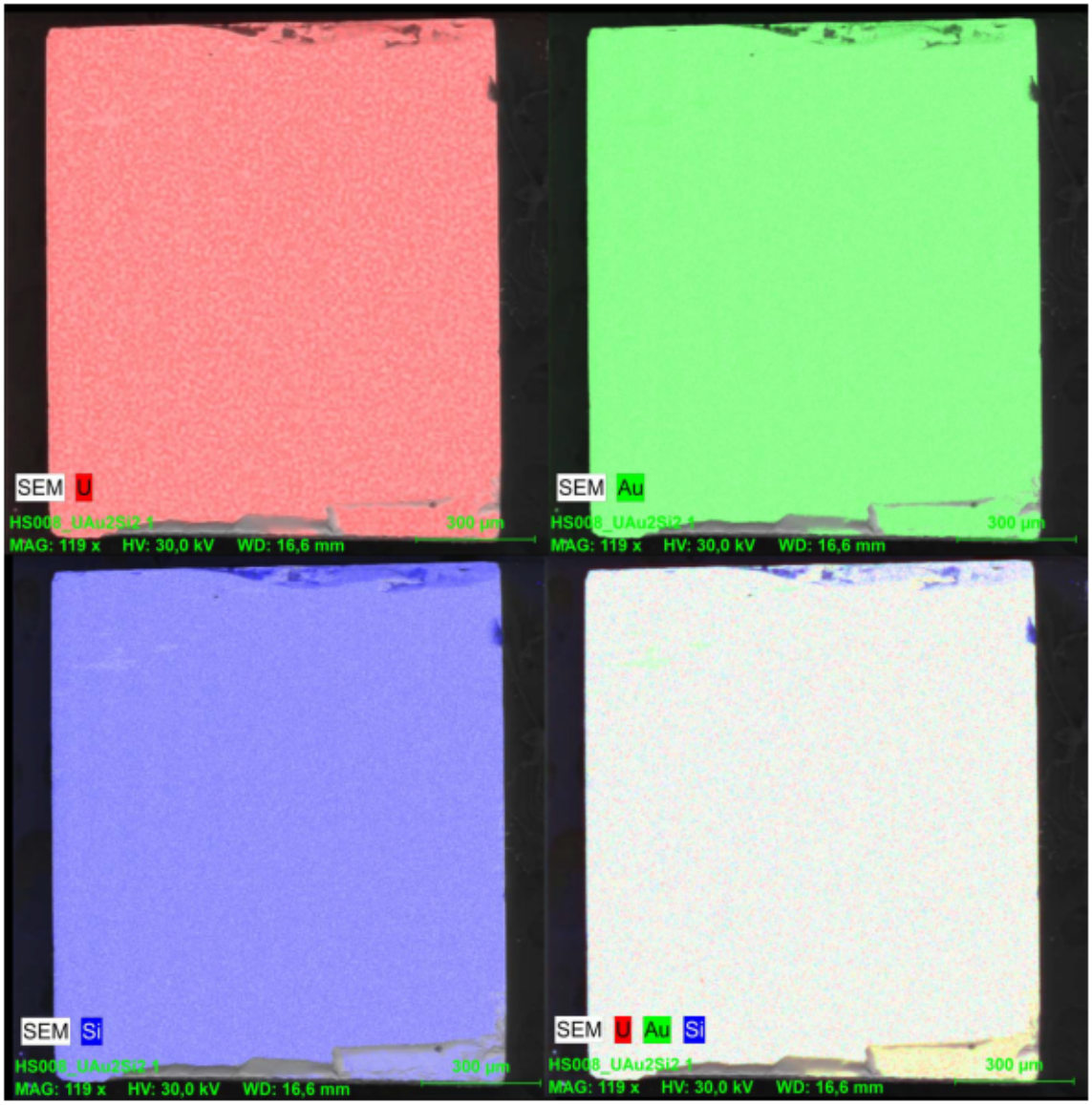

Figure 4.13: UAu_2Si_2 single crystal studied by EDX analysis with individual elemental mappings (U - red, Au - green and Si - blue). The scale bar ($300\,\mu$m) is in the bottom right corner of each image.

UIrGe

The homogeneity of the samples was checked by EDX. The elemental mapping is shown in Figure 4.14 with average stoichiometry of 1.1(1):1.0(1):0.9(1).

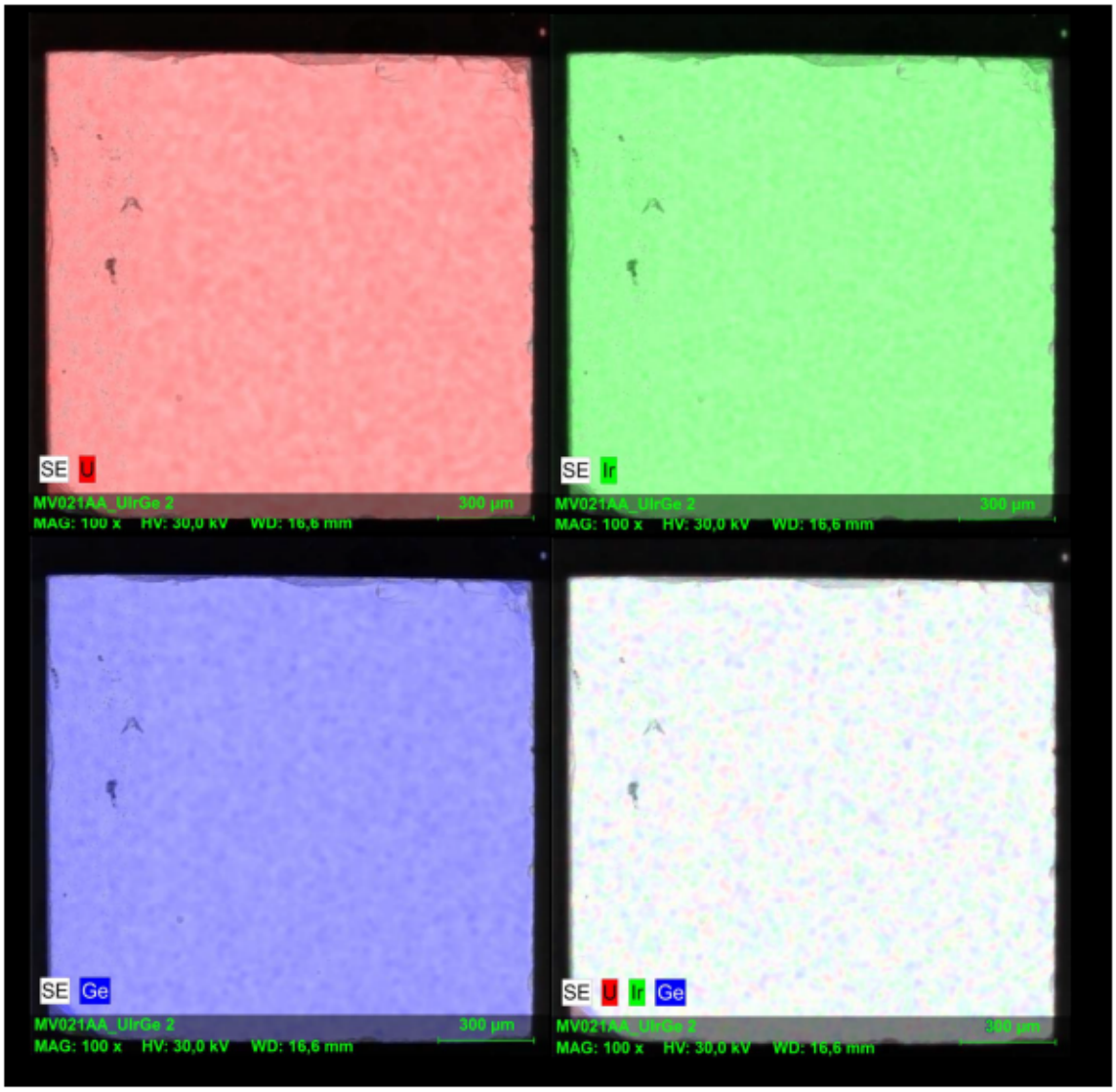

Figure 4.14: UIrGe single crystal studied by EDX analysis with individual elemental mappings (U - red, Ir - green and Ge - blue). The scale bar (300 μm) is in the bottom right corner of each image.

4.5 Preparation of samples for experiments

Samples for individual experiments were cut from the single crystals with a fine wire saw to prevent induction of additional stresses and lattice defects. The surface of the samples was precisely polished by lapping films with the final grain size of 0.1 μm which is needed for the EDX study and ensures better thermal contact during the specific-heat measurements.

5 Measurement of macroscopic properties

5.1 Magnetization, susceptibility

The magnetization measurements were performed in the *Material Growth and Measurement Laboratory*[4] (*MGML*) using the *Physical Property Measurement System* (*PPMS*) apparatus (Quantum Design, Inc.) and *Magnetic Property Measurement System* (*MPMS*) apparatus (Quantum Design, Inc.) with different methods/options. The *Vibrating sample magnetometer* option (*VSM*) of the *PPMS* device was used for the measurement of magnetization and susceptibility up to 14 T in the temperature range of 1.8 K to 300 K. More sensitive measurement method of magnetization using *Superconducting quantum interference device* (*SQUID*) in the *MPMS* apparatus and AC susceptibility measurements were performed in the same temperature range as in the previous method and with applied magnetic field up to 7 T.

The magnetization in pulsed magnetic fields up to about 58 T down to 1.8 K was measured at the *Dresden High Magnetic Field Laboratory* using a coaxial pick-up coil system. The high-field magnetometer is described in Ref. [54]. The absolute values of the magnetization were calibrated using static-field measurements.

Magnetization measurements under hydrostatic pressure were performed in the *MPMS* device using a CuBe pressure cell[55] with a liquid pressure medium and a piece of lead as manometer.

All measurements were performed on single-crystalline samples in the form of cuboids with the planes properly aligned with the main crystallographic directions. This allowed precise orientation and fastening of the samples (typically using GE varnish) to the appropriate holders.

Both the zero-field-cooled (ZFC) and field-cooled (FC) modes of measurement were conducted and compared during the data treatment.

5.2 Heat capacity

The heat-capacity measurements were performed in the *MGML* using *PPMS* apparatus (Quantum Design, Inc.) by relaxation method[56] in the temperature range $1.8 - 300\,\mathrm{K}$ up to magnetic fields of 14 T. The real measured quantity in this case is the heat capacity at constant pressure

$$C_\mathrm{p}(T) = \left(\frac{\mathrm{d}Q}{\mathrm{d}T}\right)_\mathrm{p}. \tag{5.1}$$

This can be recalculated to the heat capacity at constant volume via the following relation

$$C_\mathrm{V}(T) = C_\mathrm{p}(T) - \frac{TV}{\kappa}\beta^2, \tag{5.2}$$

[4] https://mgml.eu

where V is the volume of the substance, κ isothermal compressibility and β the volume-thermal-expansion coefficient defined in Section 3.2. Such correction is usually neglected for solids, as it is typically very small (less than a percent at low temperatures[29]). Therefore, the assumption $C_{\mathrm{p}}(T) \approx C_{\mathrm{V}}(T)$ is used through out the work and for simplicity the notation $C_{\mathrm{p}}(T) = C(T)$ is used.

All samples for the heat-capacity measurements were single crystals in the form of thin plates (thickness less than $500\,\mu\mathrm{m}$) with a mass of a few milligrams. Thermal contact of the sample with the measurement platform was provided by Apiezon N grease.

The heat capacity under hydrostatic pressure was measured by the means of steady-state calorimetry.[57] Double-layered CuBe/NiCrAl piston-cylinder pressure cell was used to generate pressures up to $\sim 3\,\mathrm{GPa}$, with a Daphne 7373 pressure medium and a manganin manometer. A micro strain-gauge was used for periodic heating of the sample and an Au/AuFe thermocouple was used to measure it's temperature oscillations. The amplitude of oscillations is inversely proportional to the sample heat capacity. Technical details of the method[57,58] and actual experimental setup used in our experiments[59] are beyond the scope of this thesis and can be found elsewhere.

5.3 Thermal expansion, magnetostriction

The thermal-expansion measurements performed in this work were carried out using a miniature capacitance dilatometer of the Vienna-type[60]. This measurement device works on the principle of the tilted-plate capacitor[61,62], where the sample itself is placed in between the capacitor plates. This method allows to measure even less regular samples, as there is no need for an ideal parallel alignment of the capacitor plates. The limitation for the sample size is the cross section fitting in a circle of $3\,\mathrm{mm}$ diameter and the length of $1-5\,\mathrm{mm}$. The advantage of the used configuration is the compact size of the device, which allows its usage in a broad variety of environments (low temperatures, high magnetic fields etc.). The body of the cell is made of silver (see Figure 5.1) and the sample is isolated from the capacitor plates by a sapphire disk.

The expansion or contraction of the sample leads to a change of the capacitance $\tilde{C}(T)$ of the cell, which is precisely measured by Andeen-Hagerling AH2500A capacitance bridge in the typical range of $3-10\,\mathrm{pF}$. The change of the measured capacitance $\tilde{C}(T)$ can be recalculated to the length change of the sample as described in Ref.[60].

The dilatometric cell was used in the standard *PPMS* apparatus (Quantum Design, Inc.) of the *MGML* in the temperature range of $1.8-300\,\mathrm{K}$ and under magnetic field up to $14\,\mathrm{T}$ applied either parallel or perpendicular to the measured length change. The same set of properly modified relations from Ref. [60] can be used for the magnetostriction measurement using the same dilatometric cell.

The single-crystalline samples for the measurement were in the form of well shaped and polished cuboids with typical dimensions of $\sim 2\times 2\times 2\,\mathrm{mm}^3$.

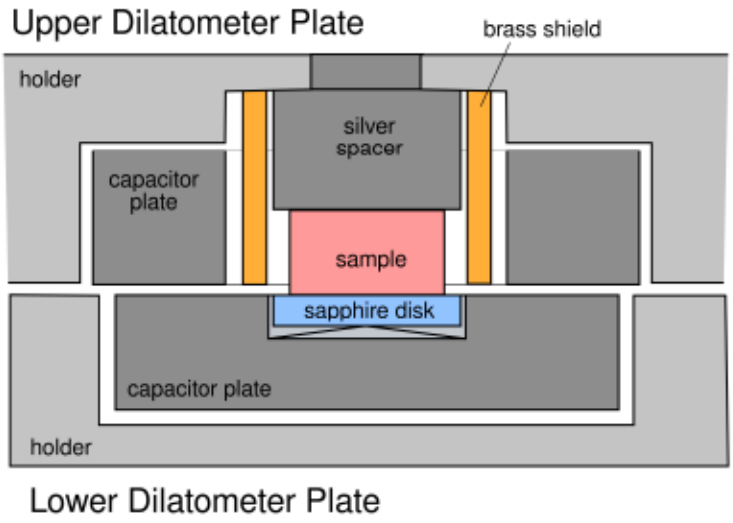

Figure 5.1: Scheme of the capacitance dilatometer. The sample (red) is isolated from the lower capacitor plate (gray) by a sapphire disk (blue) and shielded by brass shielding (orange). After Ref. [63].

5.4 Electrical resistivity, magnetoresistance

The resistivity measurements were performed using the standard four-probe method with the applied alternating current with the fixed amplitude as a part of the commercial *AC Transport* option of the *PPMS* apparatus (Quantum Design, Inc.) in the *MGML* in the temperature range $1.8 - 300\,\mathrm{K}$ and at magnetic field up to $14\,\mathrm{T}$. The measurement itself was done by passing a known current through the sample, using two contacts at the opposite sides, and measuring the voltage drop across the sample, using the other two contacts in between. Gold wires with a diameter of $25\,\mu\mathrm{m}$ were used for the current and voltage leads and they were spot-welded to the surface of the samples. The typical excitation current was set to $0.3\,\mathrm{mA}$ (or lower) to prevent Joule heating of the sample at low temperatures.

The magnetoresistance measurements at magnetic fields up to $14\,\mathrm{T}$ were carried out with the sample mounted on the horizontal rotator. This setup allows free rotation of the sample along one axis from $0° - 360°$ with respect to the direction of the applied magnetic field.

The measured resistance R was recalculated to the resistivity ρ using the measured cross section A of the sample and the length l separating the voltage contacts using the following relation

$$\rho = R\frac{A}{l}. \tag{5.3}$$

The measured single-crystalline samples were shaped in the form of cuboids with typical dimensions of about $0.5\times0.5\times5\,\mathrm{mm}^3$ with the longest edge along the direction of the applied current.

6 Neutron diffraction

The detailed study of the structural and magnetic properties of the intermetallic compounds usually requires microscopic studies that are complementary to bulk methods. One of these methods is the neutron scattering.

6.1 Nuclear and magnetic scattering

In a general neutron-scattering experiment, an incident neutron beam with the wavevector $\boldsymbol{k_i}$ hits the sample and scatters into a state with a final wavevector $\boldsymbol{k_f}$. The difference between these two vectors defines the scattering vector $\boldsymbol{Q}$ and also the momentum transfer $\hbar\boldsymbol{Q}$ to the sample as

$$\boldsymbol{Q} = \boldsymbol{k_i} - \boldsymbol{k_f}\,. \tag{6.1}$$

The neutron can also lose or gain energy during the inelastic scattering on the sample. In that case, the corresponding energy transfer E_{trans} can be written as

$$E_{trans} = E_i - E_f = \frac{\hbar^2}{2m_\mathrm{n}}\left(\boldsymbol{k}_i^2 - \boldsymbol{k}_f^2\right)\,, \tag{6.2}$$

where E_i is the initial and E_f the final energy of the neutron with mass m_n. The resulting scattering process can be described in the form of a double or partial differential cross-section. It is the number of neutrons that are scattered per second into the solid angle $\mathrm{d}\Omega$ within the energy range of $\mathrm{d}E$ around the final energy E_f. In the Born approximation, which assumes that the incoming and scattered beam can be treated as plane waves, the differential cross-section can be described using Fermi's Golden Rule as

$$\frac{\mathrm{d}^2\sigma}{\mathrm{d}\Omega\mathrm{dE}}\left(\boldsymbol{Q}\right) = \frac{|\boldsymbol{k}_f|}{|\boldsymbol{k}_i|}\left(\frac{m_\mathrm{n}}{2\pi\hbar^2}\right)^2 \sum_{\lambda,\sigma} \left|\langle \boldsymbol{k}_f\sigma_f\lambda_f \left|V\left(\boldsymbol{Q}\right)\right| \boldsymbol{k}_i\sigma_i\lambda_i\rangle\right|^2 \delta\left(E_f - E_i - E_{trans}\right)\,, \tag{6.3}$$

where the sum is over all possible initial λ_i and final λ_f states of the system and over all possible initial σ_i and final σ_f spin-states of the neutron. The delta function ensures energy conservation during the scattering process with the possible energy transfer E_{trans}. The Fourier transform $V\left(\boldsymbol{Q}\right)$ of the interaction potential $V\left(\boldsymbol{r}\right)$ describes both the nuclear and magnetic contribution to the interaction between the neutron and the sample and can be written as

$$V\left(\boldsymbol{Q}\right) = \int V\left(\boldsymbol{r}\right)\exp\left(i\boldsymbol{Q}\cdot\boldsymbol{r}\right)\mathrm{d}^3\boldsymbol{r}\,. \tag{6.4}$$

Different types of this interaction potential are discussed in the following paragraphs.

6.1.1 The nuclear interaction

The strongest contribution to the total scattering of the neutron comes from the nuclear elastic scattering. Neutrons interact with nuclei via strong nuclear force and the appropriate interaction potential can be approximated by a delta function as follows

$$V_{\mathrm{N}}(\boldsymbol{r}) = \frac{2\pi\hbar^2}{m_{\mathrm{n}}} \sum_i b_i \delta(\boldsymbol{r} - \boldsymbol{r}_i) \ , \tag{6.5}$$

where the sum is over the whole unit cell and b_i is the scattering length of the involved atom. This potential can be used in Equation (6.3) and for the unpolarized beam it is possible to decompose the partial differential cross-section into two terms: coherent and incoherent. The incoherent scattering results in an isotropic background and will not be taken into account in the following equations. As this term is negligible for aluminum, this material is widely used for sample holders, parts of the sample environment, etc. in neutron-scattering experiments.

The coherent scattering term is resulting from the interference effects and in the elastic experiment it corresponds to the observation of the Bragg peaks. For inelastic scattering it can be observed as a phonon scattering.

For elastic scattering ($E_i = E_f$) on a crystalline sample, we can observe interference of neutrons scattered from the periodic planes. It gives rise to Bragg peaks in the intensity for the case where the scattering vector $\boldsymbol{Q}$ is perpendicular to the crystal planes defined by Miller indices h, k and l and equal to the reciprocal lattice vector $\boldsymbol{q}$. The cross-section for elastic coherent scattering can thus be written as

$$\left(\frac{\mathrm{d}^2\sigma}{\mathrm{d}\Omega \mathrm{dE}}(\boldsymbol{Q})\right)_{\mathrm{coh,elast}} = \frac{(2\pi)^3}{V_0} \sum_{\boldsymbol{q}} |F_{\mathrm{N}}(\boldsymbol{Q})|^2 \delta(\boldsymbol{Q} - \boldsymbol{q}) \delta(E) \ , \tag{6.6}$$

where V_0 is the unit-cell volume and the sum is over all reciprocal vectors $\boldsymbol{q}$. The whole structure information of the unit cell (and thus of the whole crystal) is contained in the nuclear structure factor

$$F_{\mathrm{N}}(\boldsymbol{Q}) = \sum_j b_j \exp(i\boldsymbol{Q} \cdot \boldsymbol{r}_j) \ , \tag{6.7}$$

where the sum is over all nuclei at positions $\boldsymbol{r}_j$ in one unit cell. As the cross-section in Equation (6.6) is proportional to the measured intensity $I(\boldsymbol{Q})$, we can write the simplified relation

$$I(\boldsymbol{Q}) \sim |F_{\mathrm{N}}(\boldsymbol{Q})|^2 \ . \tag{6.8}$$

6.1.2 The magnetic interaction

A neutron has its magnetic dipole moment $\boldsymbol{\mu}_{\mathrm{n}}$ and thus interacts with electromagnetic field $\boldsymbol{B}(\boldsymbol{r})$ created by the spin and orbital momentum of unpaired electrons of the magnetic ions of the sample. The potential of this interaction can be written as

$$V_{\mathrm{M}}(\boldsymbol{r}) = -\boldsymbol{\mu}_{\mathrm{n}} \cdot \boldsymbol{B}(\boldsymbol{r}) \ . \tag{6.9}$$

The Fourier transform of the interaction potential in Equation (6.9) can be written as

$$V_{\mathrm{M}}(\boldsymbol{Q}) = -\boldsymbol{\mu}_{\mathrm{n}} \cdot \boldsymbol{B}(\boldsymbol{Q}) = -\mu_0 \boldsymbol{\mu}_{\mathrm{n}} \boldsymbol{M}_{\perp}(\boldsymbol{Q}) \,, \tag{6.10}$$

where $\boldsymbol{M}_{\perp}(\boldsymbol{Q})$ is the component of the Fourier transformation of the sample magnetization perpendicular to the scattering vector $\boldsymbol{Q}$. Finally, we can write the expression for the cross-section of the magnetic scattering which is similar to the Equation (6.6) as follows

$$\left(\frac{\mathrm{d}^2\sigma}{\mathrm{d}\Omega \mathrm{dE}}(\boldsymbol{Q})\right)_{\mathrm{mag,elast}} = \frac{(2\pi)^3}{V_{0\mathrm{m}}} \left(\frac{\gamma r_0}{2}\right)^2 \sum_{\boldsymbol{q}_{\mathrm{M}}} |F_{\mathrm{M}}(\boldsymbol{Q})|^2 \, \delta(\boldsymbol{Q} - \boldsymbol{q}_{\mathrm{M}}) \, \delta(E) \,, \tag{6.11}$$

where $V_{0\mathrm{m}}$ is the volume of the magnetic unit cell, the sum is over all magnetic reciprocal vectors $\boldsymbol{q}_{\mathrm{M}}$ and $F_{\mathrm{M}}(\boldsymbol{Q})$ is the magnetic structure factor. The magnetic scattering cross-section is also proportional to the measured intensity and we can define simplified relation

$$I_{\mathrm{M}}(\boldsymbol{Q}) \sim |F_{\mathrm{M}}(\boldsymbol{Q})|^2 \,. \tag{6.12}$$

6.2 Polarized-neutron diffraction

The following paragraphs are devoted to the description of only one possible utilization of this method that was used within this study.

Using a polarized beam can be very useful when one is dealing with a ferromagnet with rather small magnetic moments as the magnetic contribution to the measured scattering intensity is much smaller than the nuclear contribution. In that case, the polarized beam can enormously increase the sensitivity to the magnetic signal and allows calculation of the magnetic structure factor $F_{\mathrm{M}}(\boldsymbol{Q})$ from the measured intensity $I(\boldsymbol{Q})$.

In this type of measurement, the incident beam is polarized parallel or antiparallel to the induced moment of the sample. In simplified form the measured intensity can bewritten as[64,65]

$$I(\boldsymbol{Q}) = F_{\mathrm{N}}(\boldsymbol{Q}) F_{\mathrm{N}}^*(\boldsymbol{Q}) + F_{\mathrm{M}}(\boldsymbol{Q}) F_{\mathrm{M}}^*(\boldsymbol{Q}) + \mathbf{P_i} \left(F_{\mathrm{M}}(\boldsymbol{Q}) F_{\mathrm{N}}^*(\boldsymbol{Q}) + F_{\mathrm{M}}^*(\boldsymbol{Q}) F_{\mathrm{N}}(\boldsymbol{Q})\right) \,, \tag{6.13}$$

$$\begin{aligned} I(\boldsymbol{Q}) = {} & F_{\mathrm{N}}(\boldsymbol{Q}) F_{\mathrm{N}}^*(\boldsymbol{Q}) + F_{\mathrm{M}}(\boldsymbol{Q}) F_{\mathrm{M}}^*(\boldsymbol{Q}) \\ & + \mathbf{P_i} \left(F_{\mathrm{M}}(\boldsymbol{Q}) F_{\mathrm{N}}^*(\boldsymbol{Q}) + F_{\mathrm{M}}^*(\boldsymbol{Q}) F_{\mathrm{N}}(\boldsymbol{Q})\right) \end{aligned} \,, \tag{6.14}$$

where $\mathbf{P_i}$ is the polarization vector of the incident beam. The intensity of the ideally unpolarized beam ($\mathbf{P_i} = 0$) depends only on the sum of the squares of the structural factor and magnetic structural factor. For the polarized case ($\mathbf{P_i} \neq 0$), there are two additional non-zero terms that contribute to the measured value of intensity $I(\boldsymbol{Q})$. The ideal case of full polarization of the incident beam $|\mathbf{P_i}| = 1$ leads to an intensity in the following form for the parallel and antiparallel configuration

$$I(\boldsymbol{Q})^{\pm} = |F_{\mathrm{N}}(\boldsymbol{Q}) \pm F_{\mathrm{M}}(\boldsymbol{Q})|^2 \tag{6.15}$$

If we assume a hypothetical experiment with a ratio of the magnetic structure factor and structure factor of $F_{\mathrm{M}}(\boldsymbol{Q}) = 0.1F_{\mathrm{N}}(\boldsymbol{Q})$, then the measured intensity in the unpolarized case would be

$$I_{unp}(\boldsymbol{Q}) = F_{\mathrm{N}}^2(\boldsymbol{Q}) + \frac{2}{3}F_{\mathrm{M}}^2(\boldsymbol{Q}) \approx 1.01F_{\mathrm{N}}^2(\boldsymbol{Q}) \ , \tag{6.16}$$

where $\frac{2}{3}$ is due to the spherical averaging[65].

A polarized experiment on the same compound would give the following result for one polarization $I^+ = F_{\mathrm{N}}^2(\boldsymbol{Q}) + 2 \cdot F_{\mathrm{N}}(\boldsymbol{Q}) \cdot F_{\mathrm{M}}(\boldsymbol{Q}) + F_{\mathrm{M}}^2(\boldsymbol{Q}) = F_{\mathrm{N}}^2(\boldsymbol{Q}) + 0.2F_{\mathrm{N}}^2(\boldsymbol{Q}) + 0.01F_{\mathrm{N}}^2(\boldsymbol{Q}) = 1.21F_{\mathrm{N}}^2(\boldsymbol{Q})$ and for the opposite polarization gives the intensity of $I^- = 0.81F_{\mathrm{N}}^2(\boldsymbol{Q})$. The measured quantity of such experiment is called *flipping ratio* and is given as

$$R = \frac{I^+}{I^-} = \frac{\left(F_{\mathrm{N}}(\boldsymbol{Q}) + F_{\mathrm{M}}(\boldsymbol{Q})\right)^2}{\left(F_{\mathrm{N}}(\boldsymbol{Q}) - F_{\mathrm{M}}(\boldsymbol{Q})\right)^2} \tag{6.17}$$

The flipping ratio for the previous example would reach $R = 1.49$ affording a much higher contrast between the structure factor and the magnetic structure factor than in the unpolarized case.

Data refinement

The measured flipping ratios (Equation (6.17)) and the structure factor $F_{\mathrm{N}}(\boldsymbol{Q})$ from some previous experiment allow us to calculate the corresponding magnetic structure factor $F_{\mathrm{M}}(\boldsymbol{Q})$. As the unpaired electrons that create the magnetic moment are largely extended in real space (specially for itinerant systems) the magnetic structure factor $F_{\mathrm{M}}(\boldsymbol{Q})$ rapidly falls to zero at higher $\boldsymbol{Q}$.

The real space distribution of the magnetic moment $m(\boldsymbol{r})$ is the inverse Fourier transform of the magnetic form factor $F_{\mathrm{M}}(\boldsymbol{Q})$ and in principle can be calculated with the following relation

$$m(\boldsymbol{r}) = \frac{1}{V_{0\mathrm{m}}} \sum_{\boldsymbol{Q}} F_{\mathrm{M}}(\boldsymbol{Q}) \exp\left(-i\boldsymbol{Q} \cdot \boldsymbol{r}\right) \ . \tag{6.18}$$

Nevertheless, the limited coverage of the reciprocal space $\boldsymbol{Q}$ leads to incomplete summing, leading to termination effects that can lead to unphysical results to the calculated real space distribution of the magnetic moment $m(\boldsymbol{r})$. To overcome this problem, there exist computational methods and models for refinement of the calculated magnetic-structure factor in order to obtain a realistic map of the magnetic moment.

One of the computational methods uses the principle of maximalization of the information entropy and Bayesian statistics. It is called the maximum-entropy method (MAXENT)[66,67]. For further calculations, the unit cell is divided in to the given number N of voxels (parallelepipeds) labeled k with position $\boldsymbol{r}_k$ in the real space.

The calculated normalized densities $\rho(\boldsymbol{r_k})$ of the magnetic moment are then regarded to be equal within one voxel. The computed information entropy S for a certain distribution of the magnetic moment is thus calculated as follows

$$S = -\sum_{k=1}^{N} \rho(\boldsymbol{r_k}) \ln\left(\frac{\rho(\boldsymbol{r_k})}{\tau(\boldsymbol{r_k})}\right) , \tag{6.19}$$

where $\tau(\boldsymbol{r_k})$ is the normalized density at $\boldsymbol{r_k}$ from the prior information. This entropy S is consequently maximized under constraints K by the method of undetermined Lagrange multipliers. It is calculated by maximizing the quantity Q

$$Q = S - \lambda K - \mu\left(\sum_{k=1}^{N} \rho(\boldsymbol{r_k}) - 1\right) \tag{6.20}$$

with respect to $\rho(\boldsymbol{r_k})$, where λ and μ are two Lagrange multipliers. The calculations within this study were done using Dysnomia software [68] using a variant of the Cambridge algorithm [69] and the limited-memory Broyden-Fletcher-Goldfarb-Shanno (L-BFGS) algorithm [70] for maximizing Q (Equation (6.20)).

Indirect methods of the data refinement need some theoretical model which is adjusted to the measured data. Such approach can give more detailed information than MAXENT, however it requires good knowledge of the studied system and inherently bring simplifications. One of the widely used indirect methods is the multipolar expansion technique. The appropriate magnetic density is calculated from the spherical harmonics centered on the atoms which are tabulated for each ion [71]. This method allows to separately distinguish the size and sign of the spin and orbital component of the magnetic moment on each atom. It was originally developed for the description of electron densities for X-ray studies [72]. The magnetic form factor for each ion can be written using the spherical harmonics $\langle j_i(\boldsymbol{r})\rangle$ and the parameters W_i in the form

$$f(\boldsymbol{r}) = W_0\langle j_0(\boldsymbol{r})\rangle + W_2\langle j_2(\boldsymbol{r})\rangle = \mu_{\mathrm{T}}\left(\langle j_0(\boldsymbol{r})\rangle + C_2\langle j_2(\boldsymbol{r})\rangle\right) , \tag{6.21}$$

where μ_{T} is the total magnetic moment. The orbital contribution to the magnetic moment is $\mu_{\mathrm{L}} = \mu_{\mathrm{T}}C_2 = W_2$ and the spin contribution is $\mu_{\mathrm{S}} = \mu_{\mathrm{T}} - \mu_{\mathrm{L}} = W_0 - W_2$.

Part IV
Results and discussion

7 Almost isotropic itinerant $5f$-electron ferromagnetism in $U_4Ru_7Ge_6$

7.1 Introduction

Magnetocrystalline anisotropy (MA) is manifested by locking the magnetic moments in a specific orientation (usually the easy magnetization direction) with respect to the crystal axes. A quantitative measure of MA, the anisotropy field H_a, is the magnetic field needed to be applied in the hard magnetization direction in order to reach the easy-axis magnetization value. The key prerequisites of MA are the orbital moment of a magnetic ion, the spin-orbit interaction (SOI) coupling the orbital and spin moment, and interactions with neighboring ions [73,74]. The SOI is a relativistic effect, and becomes stronger in heavier atoms. Consequently MA dominates magnetism in materials with lanthanide and actinide series ions bearing magnetic moments of the $4f$- and $5f$-electrons, respectively.

The widely accepted scenario of the origin of magnetocrystalline anisotropy involves the crystal field (CF) interaction, the single-ion mechanism born in the electrostatic interaction of the anisotropic crystal field (the potential created at the magnetic ion site by the electric charge distribution in rest of the crystal) with the aspherical charge cloud of the magnetic electrons. The electron orbital adopts the direction that minimizes the CF interaction energy. The single-ion anisotropy is most often encountered in compounds with lanthanide series ions having well-localized $4f$-electrons [75,76].

Contrary to the $4f$-orbitals deeply buried in the core electron density of lanthanide series ions, the spatially extended uranium $5f$-electron wave functions interact with the overlapping $5f$-orbitals of the nearest neighbor U ions ($5f$-$5f$ overlap) as well as with the valence electron orbitals of ligands ($5f$-ligand hybridization [17]). Consequently the $5f$-electron wave functions loose the atomic character. This fact have a fatal impact on the formation of the U magnetic moments which are then often found dramatically reduced with respect to the U^{3+} and U^{4+} free-ion moment values. Unlike the $3d$ transition metals, which generally exhibit only a spin magnetic moment due to "freezing" of the orbital component in the crystal field, the relativistic effects, namely the strong SOI, in the heavy atoms like U induce a large orbital polarization [19,77] which is boosting the formation of a considerable orbital moment even in the case of itinerant $5f$ electrons. The relativistic energy band calculations performed for U compounds by rule provide an orbital component larger than the antiparallel spin component of a U magnetic moment [19,77–82]. These findings are in agreement with the results of polarized neutron diffraction (PND) studies of U-compounds. The pioneering PND studies were focused on US[83], UO_2[84,85] and USb[86], considered to be localized $5f$-electron systems. A strong evidence of the

important role of the $5f$-ligand hybridization was first experimentally revealed by PND on URh_3[87] with the observation of the enhanced elemental susceptibility of the Rh ion, twice the value of metal Rh. The $5f$-ligand hybridization mechanism was theoretically explained for UT_3 and UX_3 (T = transition metal and X = p-element, respectively) compounds by Koelling *et al.*[17] and corroborated by band structure calculations performed by Eriksson *et al.*[88].

The strong SOI induces a predominant orbital magnetic moment antiparallel to the spin moment in the spin-polarized $5f$-electron energy bands. This effect was first demonstrated for the itinerant $5f$-electron magnetism in UN[19]. In some cases very small, or even zero, total magnetic moment of a U ion is observed as a result of mutual compensation of the antiparallel spin and the orbital component. The itinerant $5f$-electron ferromagnet UNi_2[89], with the U magnetic moment of few hundredths of μ_B, serves as an excellent example as documented by results of polarized neutron measurements[90] and first principles electronic structure calculations[80]. Despite the itinerant character of the magnetism, UNi_2 exhibits a very strong magnetocrystalline anisotropy, with $\mu_0 H_a \gg 35\,\mathrm{T}$ at $4.2\,\mathrm{K}$[91]. Another prominent example of almost complete compensation of the spin (μ_S) and orbital (μ_L) $5f$ moments is UFe_2 with $\mu_L = 0.23\,\mu_B$ and $\mu_S = 0.22\,\mu_B$, resulting in a net moment at the U site of only $0.01\,\mu_B$. This specific situation together with the considerably different spatial distributions of the orbital and spin magnetizations result in an unusual magnetic form factor exhibiting a maximum at a finite q[92,93]. The experimental observations fulfilled the theoretical prediction of Brooks *et al.*[94] based on the finding that the $5f$-ligand hybridization reduces disproportionately the orbital moment, which usually dominates the total uranium moment in compounds, and consequently the orbital moment was predicted to become comparable to the spin moment in UFe_2.

The very strong MA seems to be inherent to the uranium magnetism. The typical values of the MA field of most uranium intermetallic compounds are of the order of hundreds Tesla[22]. The strong anisotropy is also reported for the cubic U pnictides and chalcogenides[95,96].

The strong interaction of the spatially extended U $5f$ orbitals with surrounding ligands in the crystal and participation of $5f$ electrons in bonding[12,97] imply an essentially different mechanism of MA based on a two ion (U-U) interaction, compared to the $4f$ case mentioned above. The anisotropy of the bonding and $5f$-ligand hybridization assisted by the strong SOI are the key ingredients of the two-ion anisotropy in $5f$-electron magnets.

The systematic occurrence of particular types of anisotropy related to the layout of the U ions in a crystal lattice suggests, in materials in which the U-U co-ordination is clearly defined in the crystal structure, the easy-magnetization direction is in the plane perpendicular to the nearest U-U links[21,22]. This scenario, however, does not hold for crystal structures in which the direct U-U link is shielded by the presence of non-U ligands between nearest U neighbors. Cooper and co-workers[98,99] have formulated a relatively simple model of the two-ion interaction. This model, leading to qualitatively realistic results, is based on Coqblin-Schrieffer approach to the mixing of ionic f-states and conduction-electron states, in which the mixing term of the Hamiltonian of Anderson type is treated as a perturbation, and the hybridization

interaction is replaced by an effective f-electron-band electron resonant exchange scattering. The theory has been further extended so each partially delocalized f-electron ion is coupled by the hybridization to the band electron sea, leading to a hybridization-mediated anisotropic two-ion interaction giving an anisotropic magnetic ordering.

This part of the thesis is focused on magnetism of the $U_4Ru_7Ge_6$ compound. $U_4Ru_7Ge_6$ was first prepared as a result of an attempt to obtain Ge analog to already known heavy-fermion compound URu_2Si_2 in the polycrystalline form [100]. Doping of Ge on the Si site increases volume of the unit cell and maintains the tetragonal structure up to the composition $URu_2(Si_{0.7}Ge_{0.3})_2$. For higher concentration it starts to form the cubic 4:7:6 phase of the $U_4Ru_7Ge_6$ compound [101,102]. Later work on polycrystalline samples revealed ferromagnetic behavior with ordering temperature estimated from the drop of electrical resistivity in region $10-13\,\mathrm{K}$ [44]. Ferromagnetic state of $U_4Ru_7Ge_6$ can be suppressed by substitution of Ge by Os as has been shown in Ref. [103]. $U_4Os_7Ge_6$ is Pauli paramagnet and alloying with ferromagnetic $U_4Ru_7Ge_6$ leads to the monotonous suppression of the ordering temperature towards the critical concentration $U_4(Ru_{0.7}Os_{0.3})_7Ge_6$ where the ferromagnetic order vanishes. Such behavior is believed to be a competition between RKKY interaction responsible for magnetic ordering and Kondo interaction that finally dominates and causes non-magnetic ground state of the system. Critical region might exhibit signs of quantum critical behavior [103]. More convincing evidence for quantum critical behavior in $U_4Ru_7Ge_6$ was brought by Hidaka *et al.* [104]. They tuned the ferromagnetic state to the quantum critical point by applying external pressure. Critical pressure of $\sim 2.6\,\mathrm{GPa}$ leads to lowering of ordering temperature to zero and to signs of non-Fermi liquid behavior observed on the temperature dependence of electrical resistivity. Although the first $U_4Ru_7Ge_6$ single crystals were grown already in the late 1980's, only a vague report on ferromagnetism ($T_C \sim 7\,\mathrm{K}$, $0.2\,\mu_B$/U ion in $5\,\mathrm{T}$ at $4.3\,\mathrm{K}$) [43,45] and no information on anisotropy can be found in literature.

Therefore a high quality single crystal of this compound was grown and its magnetization, AC susceptibility, thermal expansion, specific heat and electrical resistivity was measured with respect to temperature and magnetic field. A weakly anisotropic ferromagnetism has been observed below $T_C = 10.7\,\mathrm{K}$. The ferromagnetic ground state is characterized by the easy-magnetization axis along the [111] crystallographic direction. A magnetic phase transition at which the easy magnetization axis changes from [111] to [001] is observed at $T_r = 5.9\,\mathrm{K}$. The [111] ([001]) phase is associated with a tiny rhombohedral (tetragonal) distortion of the paramagnetic cubic crystal structure hardly observable in X-ray diffraction measurements. However it can be indicated by thermal-expansion data. To shed more light on the microscopic mechanisms responsible for the unusual $U_4Ru_7Ge_6$ magnetism the first-principles electronic structure calculations were also done as a part of the published papers resulting from this thesis [105,106]. These calculations were not performed by the author of this thesis. Nevertheless, as they are essential for the whole case of the $U_4Ru_7Ge_6$, they are summarized in Section 7.2.3 with the permission of its author Martin Diviš. Consequent detailed PND study at low temperature on a single crystal provides microscopic experimental evidence of the aforementioned predictions. All the ferromagnetic ura-

nium compounds studied so far by PND are characterized by a single U site in the crystallographic unit cell, both in the paramagnetic and the ferromagnetic states. The situation is different for $U_4Ru_7Ge_6$, as it is shown in the following chapter.

7.2 Results

7.2.1 Isotropic paramagnetic susceptibility

The nearly identical temperature dependencies of paramagnetic susceptibility measured along the [111] and [001] direction, are consistent with an isotropic paramagnetic state of $U_4Ru_7Ge_6$ (see the $1/\chi$ vs. T plot in Figure 7.1). The susceptibility values at temperatures above 30 K can be well fitted with a modified Curie-Weiss law[107] (Equation (1.16)). Parameters of the fit are shown in Table 7.1.

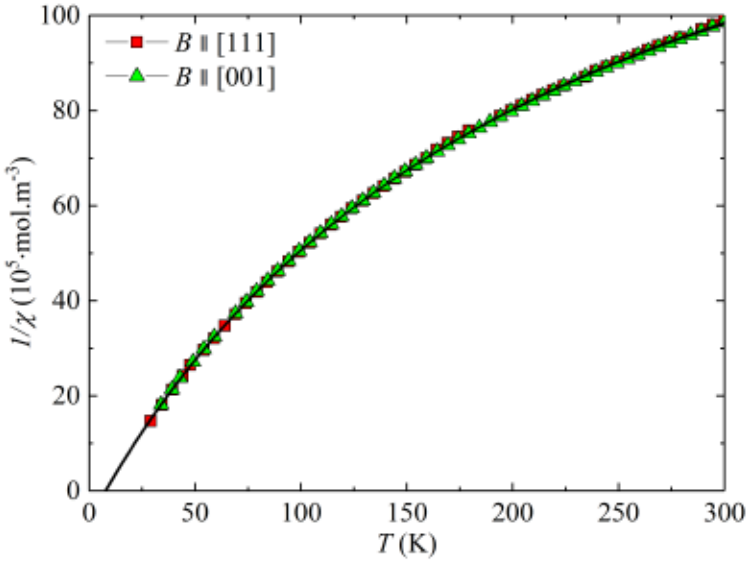

Figure 7.1: Temperature dependence of the inverse susceptibility of $U_4Ru_7Ge_6$ in a magnetic field of 1 T applied along the [111] and [001] direction. The solid curves represent the fits with a modified Curie-Weiss law.

Table 7.1: Results of the modified Curie-Weiss fit for $U_4Ru_7Ge_6$ using the Equation (1.16) in the temperature interval $30 - 300$ K.

$B \parallel$	μ_{eff} (μ_B/U)	θ_P (K)	$\chi_0 \times 10^{-8}$ (m^3 mol^{-1})
[001]	1.43	7.5	5.8
[111]	1.43	8.1	5.7

The effective moments are calculated from the parameter C (Curie constant) of Equation (1.16) via relation (Equation (1.6))[2,22]. The values for both directions

are far from the effective moments of the free ions U^{3+} ($3.62\,\mu_B$) or U^{4+} ($3.58\,\mu_B$), respectively. This points on the itinerant character of the magnetism of $U_4Ru_7Ge_6$.

7.2.2 Low temperature magnetization - weak ground-state anisotropy

The magnetization curves $M(\mu_0 H)$ measured in a magnetic field, applied along either the [111], [110] or [001] direction document that $U_4Ru_7Ge_6$ is at 1.9 K ferromagnetic with the easy magnetization direction along the [111] axis (see Figure 7.2). The spontaneous magnetization is $M_{S[111]} = 0.88\,(1)\ \mu_B$ (obtained as an extrapolation of the $M_{[111]}(\mu_0 H)$ dependence to $\mu_0 H = 0\,T$). The spontaneous magnetization for other two directions is lower. It is namely $M_{S[110]} = 0.71\,(1)\ \mu_B$ for the [110] direction and $M_{S[001]} = 0.51\,(1)\ \mu_B$ for the [001] direction being the hard magnetization direction. All these values of the spontaneous magnetization are in very good agreement with the so called Néel's phase law [108] for a cubic system. It proposes that $M_{S[001]}$ and $M_{S[110]}$ can be obtained from the $M_{S[111]}$ value multiplied by the appropriate direction cosines – i.e. $M_{S[001]} = \sqrt{\frac{1}{3}} M_{S[111]} = 0.51\,(1)\ \mu_B$ and $M_{S[110]} = \sqrt{\frac{2}{3}} M_{S[111]} = 0.72\,(1)\ \mu_B$ that is in very good agreement with the measured values. For fields higher than 0.3 T the $M_{[111]}(\mu_0 H)$, $M_{[110]}(\mu_0 H)$ and $M_{[001]}(\mu_0 H)$ curves merge. In that sense the magnetocrystalline anisotropy field can be estimated as $\mu_0 H_a \approx 0.3\,T$. However, the magnetization does not saturate in a field up to the 14 T, where the magnetization reaches the value of $1.4\,\mu_B$/f.u.. The poor saturation of the magnetization in high magnetic fields is typical for itinerant electron ferromagnets. The increasing magnetic moment with increasing magnetic field is then reflecting the magnetic-field induced change of the electronic structure (additional splitting of the majority and minority subbands).

This very weak magnetization anisotropy makes $U_4Ru_7Ge_6$ an unique exception among the U ferromagnets, which are normally strongly anisotropic with anisotropy fields of several hundred Tesla [22]. In the next section this issue is approached by the first-principles electronic structure calculations focused on the microscopic origin of U magnetic moments and MA.

7.2.3 First-principles calculations

To obtain microscopic information about magnetism in $U_4Ru_7Ge_6$ the first-principles methods based on density functional theory (DFT) including spin-orbit interaction (SOI) were applied. The Kohn-Sham-Dirac 4-components equations have been solved by using the latest version of the full-potential-local-orbitals (FPLO) computer code[109]. Both the Local Spin Density Approximation (LSDA) [110] and the General Gradient Approximation (GGA) [111] were used. The $5f$-states were treated as an itinerant Bloch states. Several k-meshes in the Brillouin zone were involved to ensure the convergence of charge densities, total energy and magnetic moments. For the sake of simplicity a collinear ferromagnetic structure was assumed.

In $U_4Ru_7Ge_6$ the total ground-state magnetic moment was found to point along the [111] direction. Due to the SOI, the symmetry is reduced from 48 to 12 sym-

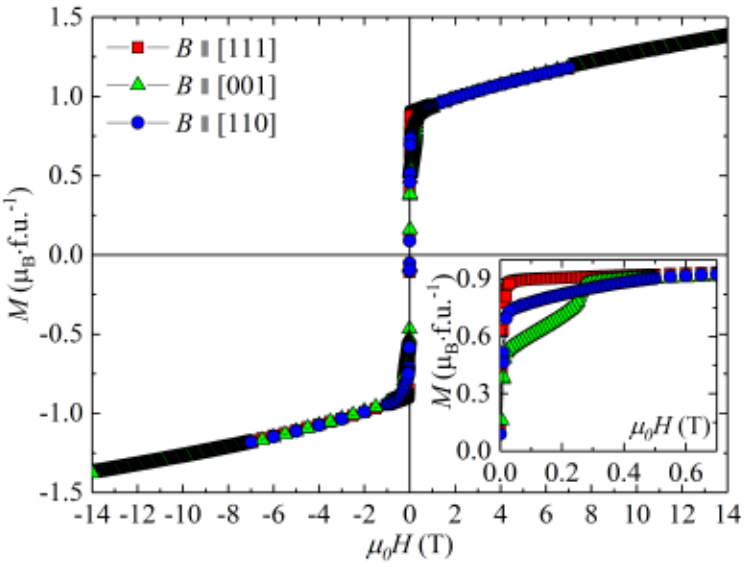

Figure 7.2: Field dependence of magnetization isotherms of $U_4Ru_7Ge_6$ at 1.9 K for the applied magnetic field along the [111], [110] and [001] directions. Inset shows a low field detail.

metry operations. Instead of four symmetrically equivalent U ion sites in the scalar relativistic treatment with a spin-only magnetic moment, the spin and orbital angular momenta are coupled by the relativistic SOI which divides the U ions in two subgroups consistent with the expected rhombohedral distortion induced by magnetoelastic interaction in case of the [111] easy magnetization direction. The U ions in the first subgroup at the U_1 positions (0.25, 0.25, 0.25) and (0.75, 0.75, 0.75), have a very small total magnetic moment of $-0.01\,\mu_B$ due to cancellation of the almost equal-size antiparallel spin and orbital moment (see Figure 7.3), using LSDA. In GGA, the cancellation is not so pronounced leading to the moment of $-0.103\,\mu_B$. The second subgroup includes the U ions at the remaining six U_2 positions bearing the spin magnetic moment of $-0.56\,\mu_B$ and the orbital magnetic moment of $0.79\,\mu_B$, using LSDA. GGA provides a slightly enhanced spin ($-0.82\,\mu_B$) and orbital ($1.021\,\mu_B$) magnetic moment. There are also some hybridization-induced Ru magnetic moments, which summed to give $0.29\,\mu_B$ and $0.653\,\mu_B$ for LSDA and GGA, respectively. The calculated Ge magnetic moment is negligible for both methods. The summation over the seventeen ions (one formula unit) in the primitive crystallographic cell gives the total magnetic moment of $1.01\,\mu_B$ and $1.231\,\mu_B$ for LSDA and GGA, respectively. It is somewhat larger than the spontaneous magnetic moment determined by experiment.

The relativistic calculations were performed also with the moment along [001]. In this case the cubic symmetry is reduced to tetragonal, and all U moments have the same value of spin ($-0.529\,\mu_B$ and $-0.794\,\mu_B$) and orbital ($0.706\,\mu_B$ and $0.939\,\mu_B$) component for LSDA and GGA, respectively. The coordination polyhedra of U atom contains of seven Ru atoms with partially occupied delocalized Ru $4d$-states (see Figure 7.3). These $4d$-states hybridized strongly with U $5f$-states. There-

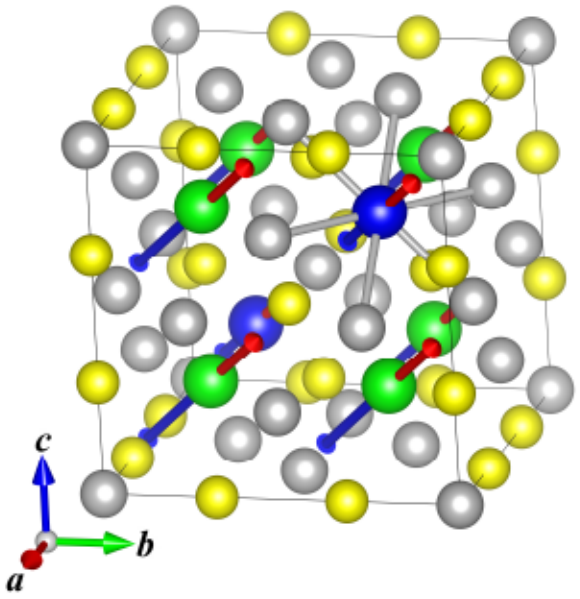

Figure 7.3: Structure of $U_4Ru_7Ge_6$ together with magnetic moments from theoretical calculations (see Section 7.2.3). Arrows for magnetic moments are in proper relative scale but in arbitrary units. U_1 ions are blue, U_2 are green, Ru_1 and Ru_2 are gray and Ge are yellow. The shortest distances $U_{(1,2)} - Ru_1$ are marked by gray cylinders.

fore the correlations inside LSDA and GGA are sufficient for a good description of magnetic moments in the presence of spin-orbit interaction. It is not necessary to introduce some other method which would describe strong correlations between the $5f$-electrons like LSDA+U. This is, for instance, the main difference of the $U_4Ru_7Ge_6$ case from the heavy-fermion compound UBe_{13}[112], in which the uranium ion is buried in the Be-ligand cage, but the Be has an occupied $2s$-subshell and hybridization with U $5f$-states is much weaker. Therefore the correlations inside the $5f$-subshell are much more pronounced than in $U_4Ru_7Ge_6$.

When calculating the magnetocrystalline anisotropy energy between the configurations of magnetic moments aligned along the [111] and [001] axis, the values of the total energy were used. In agreement with experiment, it was found that the ground state with the total moment points to the [111] direction using both LSDA and GGA. The excited state with the moment pointing to the [001] direction is $0.9\,\mathrm{meV}$ above the ground state. This value is in agreement within the order of magnitude with the energy corresponding to $T_r = 5.9\,\mathrm{K} \approx 0.5\,\mathrm{meV}$, the temperature of the [111] to [001] spin reorientation transition that is described in the following section.

To test the performance of LSDA and GGA the equilibrium volume were calculated and compared with experimental value V_0. The LSDA overbinds the minimal volume by $4.8\,\%$ ($V/V_0 = 95.2$). In contrast to this value the GGA improves the agreement with experiment remarkably ($V/V_0 = 1.01$). Therefore the GGA description of $U_4Ru_7Ge_6$ seems to be more precise than LSDA. Calculated components of magnetic moment using GGA for all the atoms in the unit cell are listed in the Table 7.4.

7.2.4 Phenomena near magnetic phase transitions

The Curie temperature, T_C, of a ferromagnet is frequently estimated as the temperature of the inflection point of the $M(T)$ curve measured in a low magnetic field and/or of the temperature dependence of the AC-susceptibility. In Figure 7.4 (a) one can see from $M(T)$ measured in the external magnetic field of $10\,\mathrm{mT}$ applied along the [111], [110] and [001] direction, an inflection point at the same temperature of $10.6 \pm 0.1\,\mathrm{K}$ ($\sim T_C$) and a crossing at $T_r = 5.9 \pm 0.1\,\mathrm{K}$. Two sharp anomalies at corresponding temperatures can be seen in the $\chi_{AC}(T)$ dependence shown in Figure 7.4 (b). These results clearly document that $U_4Ru_7Ge_6$ orders ferromagnetically at T_C with the easy magnetization axis [001] (which is demonstrated by the $9\,\mathrm{K}$ magnetization isotherms in the inset of Figure 7.4 (a)). At T_r the crystal undergoes a spin reorientation transition to a ground state characterized by the easy magnetization axis along [111] as was also visible in the $M(H)$ magnetization curve at $1.9\,\mathrm{K}$ in Figure (7.2). Through the whole temperature range the [110] direction stays as an intermediate axis.

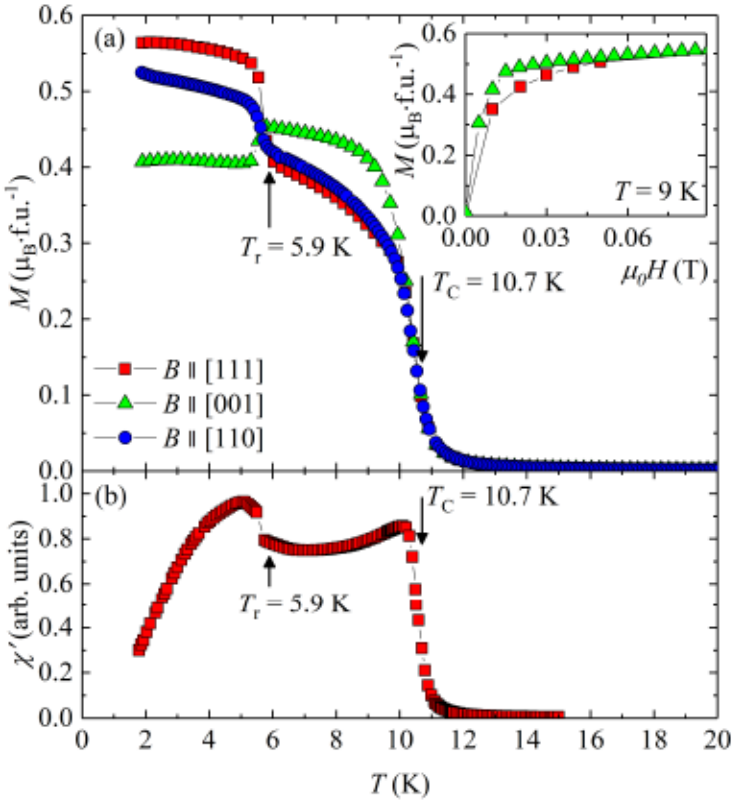

Figure 7.4: Temperature dependence of the magnetization of $U_4Ru_7Ge_6$ measured in a magnetic field of $10\,\mathrm{mT}$ (in the ZFC regime) applied along the [111], [110] and [001] direction (a) and temperature dependence of the AC susceptibility in the AC field applied along the [111] (b). Inset in the upper panel shows field dependence of magnetization at $9\,\mathrm{K}$.

More rigorous method of determining Curie temperature of a ferromagnet from magnetization data is based on the analysis of so called Arrott plots, i.e $M^2(\mu_0 H/M)$ isotherms in the vicinity of the ordering temperature [113]. Linear Arrott plots are in fact a graphical representation of the Ginsburg-Landau mean field theory of magnetism in the vicinity of the ferromagnetic to paramagnetic second order phase transition. In Figure 7.5 one can see that the Arrott plots for $U_4Ru_7Ge_6$ in a magnetic field applied along the easy magnetization direction [001] are almost linear with varying slope for magnetic fields between 1 and 7 T, whereas for lower fields they became slightly convex. The linear extrapolations of high-field data to the vertical axis mark the values of M^2, which are considered as estimates of the square spontaneous magnetization M_S^2. The spontaneous magnetization as the order parameter of a ferromagnetic phase vanishes at T_C. Note the use of the linear extrapolations from high fields in the case of the convex curvature of $U_4Ru_7Ge_6$ Arrott plots in low fields leads to a certain overestimation of M_S values, and consequently to a higher estimated $T_C^* \approx 12$ K. This is not in agreement with the estimation of T_C from the temperature dependence of magnetization and AC susceptibility.

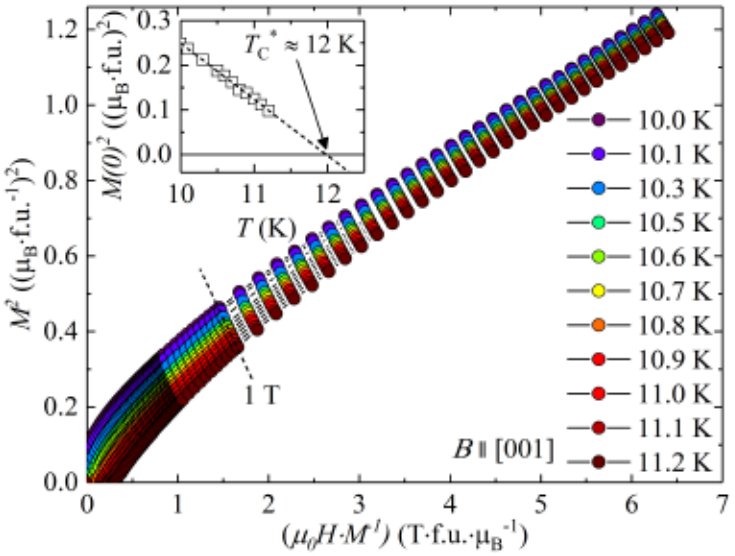

Figure 7.5: Arrott plots for $U_4Ru_7Ge_6$ in a magnetic field applied along the [001] direction. The solid lines are only guides to the eye. The inset shows the linear extrapolation (dashed line) of the square of spontaneous magnetization to zero as an estimation of the ordering temperature T_C^*.

A more precise T_C value may be expected from the generalized approach using the Arrott-Noakes equation of state

$$(\mu_0 H/M)^{1/\gamma} = (T - T_C)/T_1 + (M/M_1)^{1/\beta} , \tag{7.1}$$

where M_1 and T_1 are material constants [114]. The magnetization data were reanalyzed by plotting them as $M^{1/\beta}$ vs. $(\mu_0 H/M)^{1/\gamma}$ with critical exponents β and γ chosen to get the best possible linearity of these plots while keeping them parallel with constant

slope. The values $\beta = 0.31 \pm 0.03$ and $\gamma = 0.81 \pm 0.04$ lead to a linear dependence in the broad field range, except the very low fields. This construction is plotted in Figure 7.6 for all measured isotherms. This approach leads to $T_C = 10.7 \pm 0.1$ K (see inset of Figure 7.6), in much better agreement with the estimated value from the low field magnetization data.

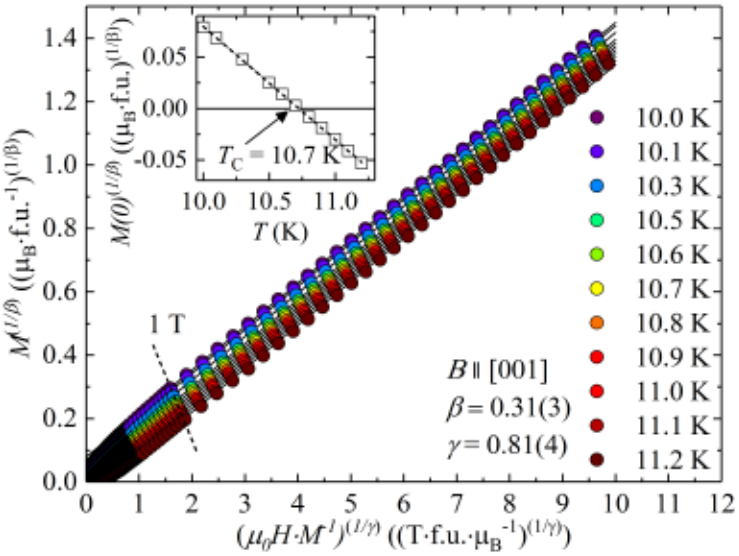

Figure 7.6: Arrott-Noakes plots reflecting the equation of states (with $\beta = 0.31 \pm 0.03$ and $\gamma = 0.81 \pm 0.04$) for $U_4Ru_7Ge_6$ in the magnetic field applied along the [001] direction. The solid lines are linear fits. The inset shows the linear extrapolation (dashed line) of the square of spontaneous magnetization to zero as an estimation of the ordering temperature T_C.

The critical magnetization isotherm should obey relation $M \sim (\mu_0 H)^{1/\delta}$ (Equation (2.8)) that sets the next critical exponent δ. The magnetization curves for the magnetic field applied along the [001] direction are plotted in the logarithmic scale in Figure 7.7.

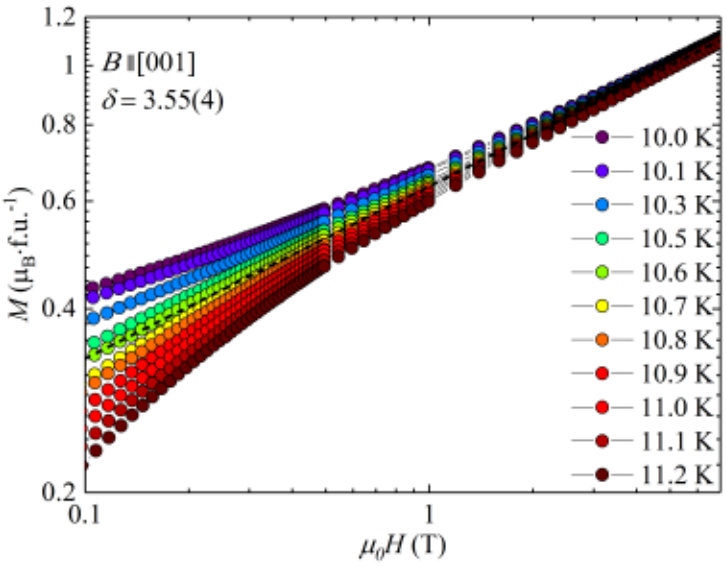

Figure 7.7: Log-Log plot of the field dependence of magnetization for $U_4Ru_7Ge_6$ in the magnetic field applied along the [001] direction. The critical isotherm at $T_C = 10.7\,K$ is fitted by linear function (dashed line) in the field interval of $1 - 7\,T$ to obtain the critical exponent $\delta = 3.55 \pm 0.04$.

The fitted value of the critical exponent is $\delta = 3.55 \pm 0.04$ and the linear dependence starts to deviate from the critical isotherm for lower magnetic fields. The critical exponent δ in the ideal case might satisfy the Widom scaling relation $\delta = 1+\gamma/\beta$ (Equation (2.9)) which for β and γ, provided by the Arrott-Noakes analysis, gives $\delta = 3.61 \pm 0.04$. This is in excellent agreement with the value obtained from the direct fitting of the critical isotherm. Note that the critical exponents for the mean field approximation are $\beta = 0.5$, $\gamma = 1$ and $\delta = 3$ (see Table 2.1), however Yamada[115] has shown that spin fluctuations in weak itinerant ferromagnets lead to Arrott plots linear in strong magnetic fields and bent downwards at the region of small magnetizations.

Heat capacity data measured at zero magnetic field show a clear anomaly at $10.7\,K$ as displayed in Figure 7.8. This temperature is consistent with the T_C value determined from the magnetization data by Arrott-Noakes plot analysis. The estimated magnetic entropy at T_C (i.e. integrated from $0.3\,K$ to T_C) of $0.2\,R\ln 2$ is much lower than $R\ln 2$ yielding additional evidence of itinerant electron magnetism in $U_4Ru_7Ge_6$. For the itinerant limit case, in which local moments disappear at T_C, the magnetic entropy is equal to zero, because the entropy above T_C (no moments) is equal to the low-T limit (moments ordered, no fluctuations) [22]. The archetypal example of itinerant ferromagnet is $ZrZn_2$, with entropy of $\approx 0.005\,R\ln 2$[116,117]. The magnetic moment reorientation transition at T_r is reflected in a tiny, but clear, peak at this temperature.

The gamma coefficient of the electronic specific heat determined from a standard C/T vs. T^2 plot (see Inset in Figure 7.8) by the fit with Equation (3.6) of the data below $4\,K$ is $\gamma = 362\,mJ \cdot mol^{-1} \cdot K^{-2}$. The value related to one U ion

is $\gamma = 90.5\,\mathrm{mJ \cdot mol^{-1} \cdot K^{-2}}$ and reflects the presence of the U $5f$-electron states at the Fermi energy E_F similar to numerous other U intermetallics with itinerant $5f$-electrons which usually exhibit elevated values somewhere between 30 and $100\,\mathrm{mJ \cdot mol^{-1} \cdot K^{-2}}$ per U ion [22].

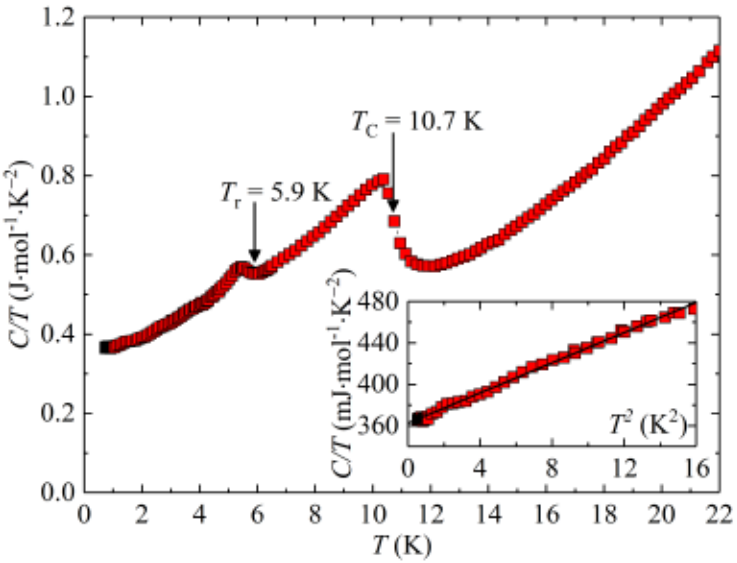

Figure 7.8: Temperature dependence of the heat capacity (C/T vs. T plot) of $\mathrm{U_4Ru_7Ge_6}$. Inset shows the the C/T vs. T^2 plot with fit to the Equation (3.6).

The linear thermal expansion $\Delta l/l$ was measured along the [001], [111] and [110] direction in zero magnetic field (seen in Figure 7.9). It shows two distinct anomalies which can be attributed to the magnetic phase transitions revealed by magnetization measurements (T_C and T_r). When cooling from higher temperatures, a downturn (upturn) in the vicinity of T_C is followed by a steep increase (decrease) of the corresponding $\Delta l/l$ below $\sim 6\,\mathrm{K}$ ($\sim T_\mathrm{r}$) that is seen for the [001] ([111]) direction, respectively. The linear thermal expansion of the [110] direction shows only mild changes (small upturn) at T_C and (small step) below T_r.

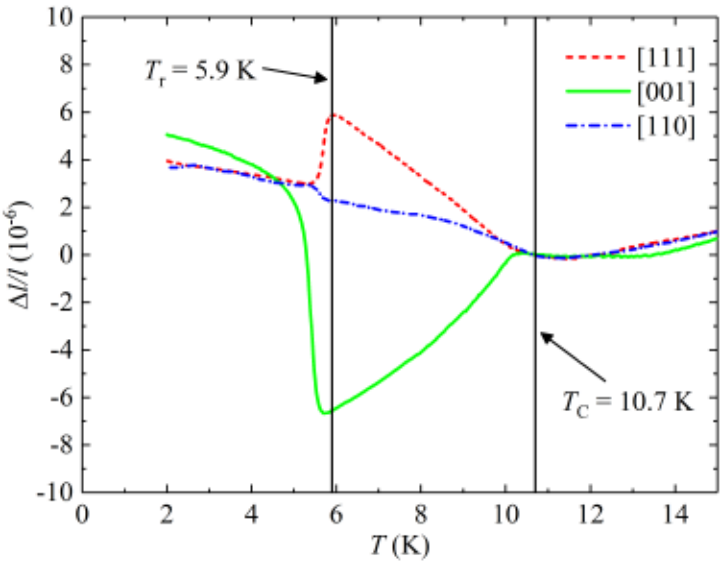

Figure 7.9: Linear thermal expansion of $U_4Ru_7Ge_6$ along the [001], [110] and [111] directions. The vertical lines mark the position of the T_r and T_C.

Most thermal expansion studies of ferromagnets revealing the spontaneous magnetostriction at temperatures $T < T_C$ were done using X-ray or neutron diffraction [118]. The structure of the single crystal of $U_4Ru_7Ge_6$ was also studied by X-ray powder diffraction at low temperatures, down to 3 K [105]. No change of diffraction within the experimental error has been observed below 11 K.

From Figure 7.9 it is however evident that the thermal expansion data obtained by dilatometer on the $U_4Ru_7Ge_6$ single crystal clearly demonstrate the existence of lattice distortions in the ferromagnetic state. They might be possible tetragonal in the $T_r < T < T_C$ range an rhombohedral below T_r. The distortions here are, however, very small ($< 10^{-5}$).

The dilatometer can be used to determine the crystal distortions along the three perpendicular crystal axes [100], [010] and [001]. To study the corresponding linear spontaneous magnetostriction of a ferromagnet with a dilatometer one should perform measurements on a single crystal sample containing only one ferromagnetic domain. The magnetization data suggest, that in the temperature interval $T_r < T < T_C$ the magnetization easy axis is [001]. Therefore, it is possible to estimate the volume change of this phase. For that purpose the crystal was at first cooled down to 6.2 K (the temperature just above the onset of the spin reorientation transition) in a field of 1 T parallel to the [001] direction to obtain single domain sample. At this temperature the magnetic field was decreased down to 30 mT, and then the thermal expansion was measured in the longitudinal $(\Delta l/l)_{[001]}$ and transversal $(\Delta l/l)_{[100]}$ geometry with increasing temperature up to T_C. In this experiment, in fact, the thermal expansion along the c and a axis of the ferromagnetic tetragonally distorted structure was measured. A field of 30 mT applied along [001] is the minimum field maintaining the single-domain sample with the magnetic moment oriented along the c axis. These $(\Delta l/l)_{[001]}$ and $(\Delta l/l)_{[100]}$ thermal expansion data can be taken as a

reasonable approximation of spontaneous linear magnetostriction (denoted as $\lambda_{S[001]}$ and $\lambda_{S[100]}$, respectively).

One can see that the value of the spontaneous tetragonal distortion is negative (the c axis shrinks) and very small ($\lambda_{S[001]} \sim -9 \times 10^{-6}$ at 6.2 K). Simultaneously the a axis expands ($\lambda_{S[100]} = \lambda_{S[010]} \sim 9 \times 10^{-6}$ at 6.2 K). Figure 7.10 shows also the corresponding spontaneous thermal volume expansion usually denoted as $\omega_S \left(= 2 \cdot \lambda_{S[100]} + \lambda_{S[001]}\right)$. As expected for an itinerant electron ferromagnet, the volume of the $U_4Ru_7Ge_6$ lattice expands below T_C. Reasonable data can be collected only down to 6.2 K. Below this temperature the magnetic-moment-reorientation transition from the [001] to the [111] direction commences and the direction of magnetic moment becomes uncertain despite a magnetic field of 30 mT applied along [001].

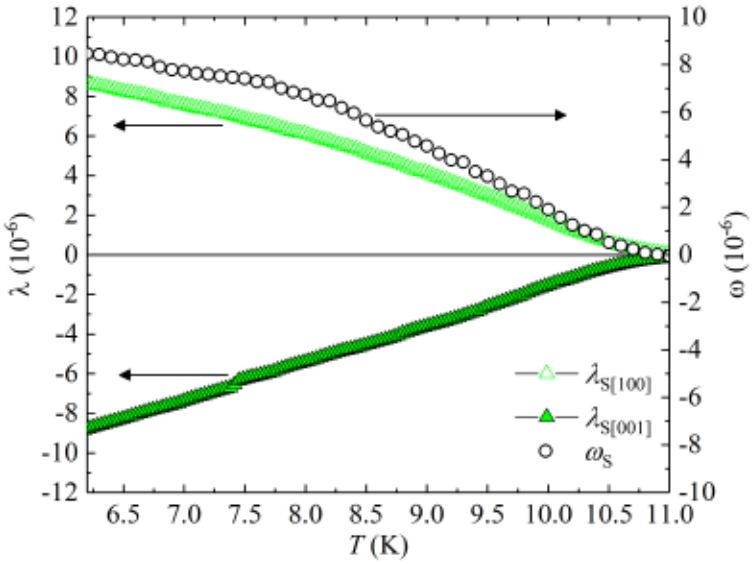

Figure 7.10: Linear thermal expansion along the [001] and [100] (denoted as $\lambda_{S[001]}$ and $\lambda_{S[100]}$ on the left axis) direction in a magnetic field of 30 mT applied along [001], and the corresponding thermal volume expansion (denoted as ω_S on the right axis). Temperatures are from 6.2 K up to T_C. The data are considered as the best estimation of corresponding spontaneous magnetostriction (see text).

The longitudinal magnetostriction measurement for three different directions [001], [110] and [111] is plotted in Figure 7.11. The curves were measured at 2 K and 9 K, i.e. below T_r where the easy axis is [111] and in the interval $T_r < T < T_C$ where the easy axis is [001].

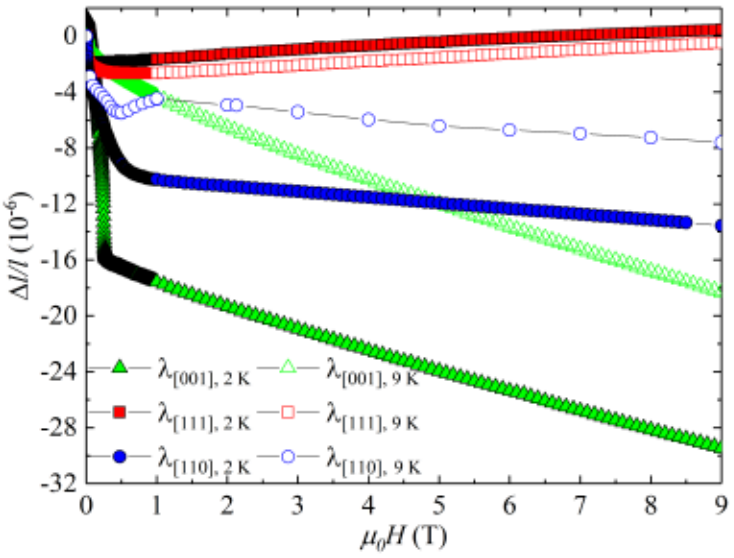

Figure 7.11: Longitudinal magnetostriction for the [100], [110] and [111] direction at 2 K and 9 K.

The magnetostriction for the direction [001] shows initial fast drop followed by steady monotonous decrease. The slope of the high field dependence is almost independent on the temperature. Very similar behavior is observed for the [110] direction except the minimum around 0.5 T at the 9 K data. Initial drop is also present for the [111] direction but increasing of the applied field leads to the prolongation of the unit cell along [111]. Opposite trend of the magnetostriction for [111] and [001] direction is another evidence for the distortion of the formerly cubic lattice, that can be obviously also induced by the applied magnetic field.

Large effect of the applied external field can be observed on the transversal magnetostriction. In that configuration magnetic field was applied along the [100] axis and the length change was measured in the perpendicular direction [001]. Resulting curves are plotted in Figure 7.12 and are very similar for the 2 K and 9 K data. They both exhibit large and positive length change that is opposite to the contraction observed for the longitudinal measurement of the [001] direction in Figure 7.11.

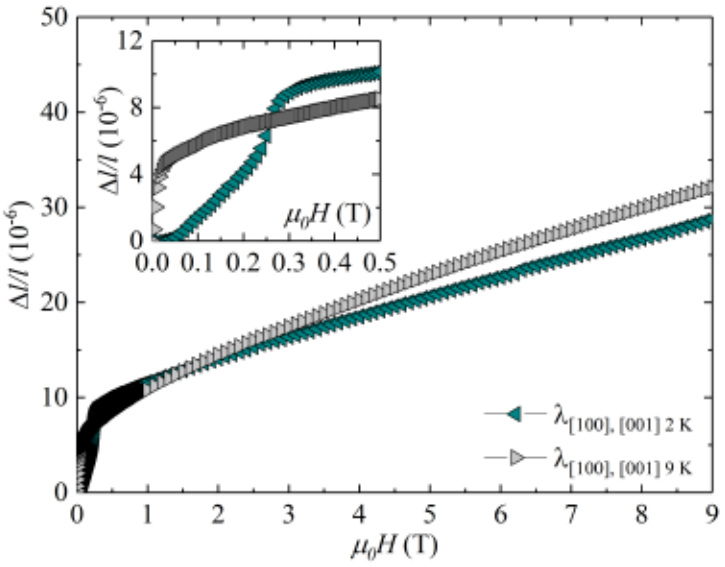

Figure 7.12: Transversal magnetostriction for the field applied along the [100] direction and the length change measured along the [001] at 2 K and 9 K. The inset shows the low field region.

The length change is slightly higher for the 9 K data as it lies in the $T_r < T < T_C$ temperature interval where the inherent tetragonal distortion is expected. It thus have the main axes well aligned with respect to the transversal measurement. As the structure at 2 K is proposed to be rhombohedral the transversal geometry of the measurement does not have to necessarily correspond to the symmetric directions in the unit cell.

The magnetostriction curves $\lambda(\mu_0 H)$ strongly resembles the magnetization $M(\mu_0 H)$ data and while plotted as $\lambda(M^2)$ (see Figure 7.13) for the field interval $0.5 - 7$ T they show clear linear trend. As expected from the longitudinal magnetostriction, slopes of these linear trends are opposite for the [001] and [111] direction and almost independent on the temperature. This linear dependence is in agreement with the itinerant character of magnetism of $U_4Ru_7Ge_6$ where $\lambda \sim M^2$ (see Equation (3.17)).

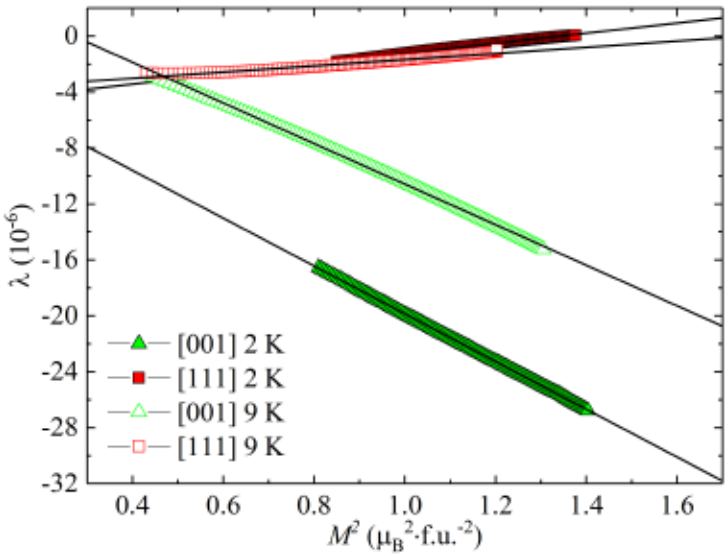

Figure 7.13: Combined plot of the magnetostriction as a function of the square of magnetization $\lambda\,(M^2)$ in the field interval of $0.5-7\,\mathrm{T}$ at $2\,\mathrm{K}$ and $9\,\mathrm{K}$. The solid lines are linear fits.

The almost identically corresponding values of the electrical resistivity measured for current along [111] and [001] direction over the entire temperature range $2-300\,\mathrm{K}$ indicates a quite isotropic electron transport in $\mathbf{U_4Ru_7Ge_6}$ (see Figure 7.14). The convex $\rho\,(T)$ curve in the paramagnetic state rather resembles the behavior of transition metal compounds. This trend changes at T_C to the low-temperature concave curve with a T^2 scaling (fit of the T^2 dependence is marked as a dashed line in the inset of Figure 7.14). When inspecting the second derivative, there is a deep minimum of $\partial^2\rho/\partial^2 T$ at T_C and a local minimum at T_r.

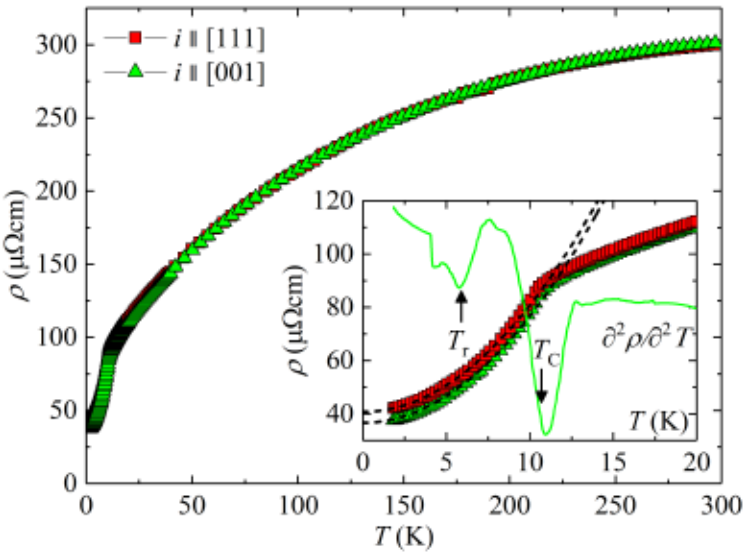

Figure 7.14: Temperature dependence of electrical resistivity of the $U_4Ru_7Ge_6$ measured for current along [111] and [001] direction. The inset shows the low temperature region together with the second derivative (solid line) of the [001] curve where the two arrows show the position of T_r and T_C. The dashed lines are fits to the T^2 dependence.

7.2.5 Suppression of magnetism under hydrostatic pressure

Previous studies on polycrystals of $U_4Ru_7Ge_6$ revealed possibility to suppress the ferromagnetism towards the quantum critical point by applying hydrostatic pressure[104]. However, the T_r transition was not tracked within that work as it is probably less pronounced on the polycrystalline samples.

The electrical resistivity measurements of the single crystals under hydrostatic pressure up to 3 GPa were performed within this work. Strong pressure dependence with similar slope was observed for both transitions T_r and T_C (see Figure 7.15).

The critical pressure for T_r is extrapolated towards $p_{cr,Tr} \approx 1.4$ GPa where this reorientation temperature is suppressed to 0 K. Higher pressure is needed for Curie temperature where the extrapolated value is $p_{cr,TC} \approx 2.8$ GPa and the ferromagnetic order disappears in the possible quantum critical point QCP.

7.2.6 Crystal structure study

The room-temperature space group $Im\bar{3}m$ has the group $R\bar{3}m$ as the only rhombohedral maximal subgroup[119]. In the frame of the $R\bar{3}m$ space group former single U site in a Wyckoff position 8*c* is split into two different sites U1 and U2 with Wyckoff position 3*b* and 9*d*, respectively. As it is in agreement with the prediction of two different U sites with the same multiplicity by DFT (Section 7.2.3 and Ref.[105]), it is assumed that $R\bar{3}m$ is a possible subgroup describing the ground state structure of $U_4Ru_7Ge_6$. All the following data will be comparably refined using both the room

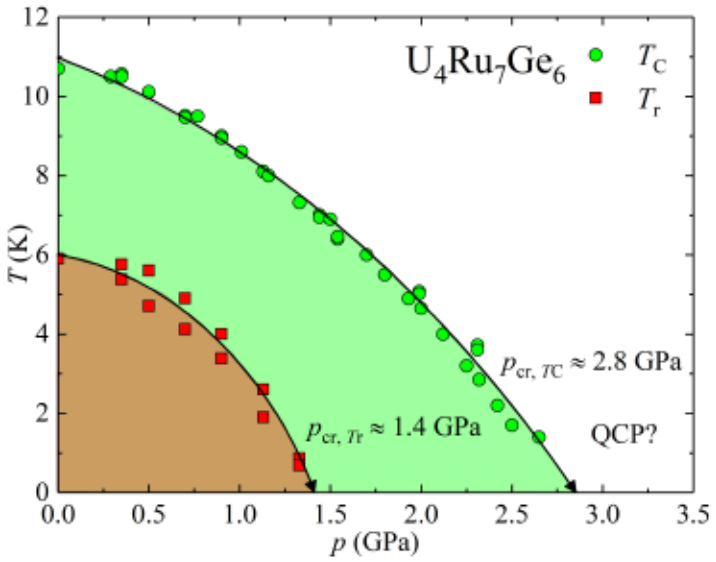

Figure 7.15: Pressure phase diagram of $U_4Ru_7Ge_6$ revealing the suppression of T_r and T_C towards the extrapolated critical pressures $p_{cr,Tr}$ and $p_{cr,TC}$. Possible presence of QCP is marked at the critical pressure $p_{cr,TC}$. All data points are deduced from the electrical resistivity measurements.

temperature cubic space group $Im\bar{3}m$ and proposed distorted rhombohedral $R\bar{3}m$ space group, to rigorously study the ground state structure. The transformations of the unit cell parameters, lattice vectors, atomic site fractional coordinates and h, k, l indices between the $Im\bar{3}m$ and $R\bar{3}m$ space group are summarized in Table 7.2, where the hexagonal description of $R\bar{3}m$ is used.

As can be seen from the lattice vector transformation in Table 7.2 the rhombohedral $R\bar{3}m$ unit cell is rotated with respect to the cubic $Im\bar{3}m$ in the way that former $[111]_{cub}$ direction is parallel with the new $[001]_{hex}$ and $[-110]_{cub}$ points along transformed $[100]_{hex}$ (see Figure 7.16).

The six $Ru2_{cubic}$ $12d$ ions are forming a hexagonal arrangement around the U ions in the cubic structure that is perpendicular to the body diagonals. This local coordination is crucial for the structure of $U_4Ru_7Ge_6$, as the shortest inter-uranium distance $d_{U-U} = \frac{a_{cub}}{2} \approx 4.14665\,\text{Å}$ is rather large while the distance between U ion and the nearest Ru ions $d_{U-Ru2_{cubic}} \approx 2.93212\,\text{Å}$ highlights the importance of hybridization between U $5f$ and Ru $4d$ wavefunctions. The proposed symmetry change is most pronounced in the change of the fractional coordinate x of the $Ru2_{cubic}$ $12d$ ($Ru2_{hex}$ $18g$) site, that is no longer fixed by symmetry. Formerly the U $8c$ position has $.-3m$ point symmetry (it has no symmetry along the cubic primary directions in the $\{100\}_{cub}$ family, three-fold rotoinversion axis along the secondary direction family $\{111\}_{cub}$ and mirror plane perpendicular to the $\{110\}_{cub}$ family). As the fractional coordinate x of the $Ru2_{hex}$ position starts to deviate from the 0.25 value, this strict hexagonal arrangement is conserved only for the U1 sites in the distorted rhombohedral structure. It can be seen from the preserved site symmetry of the U1 site,

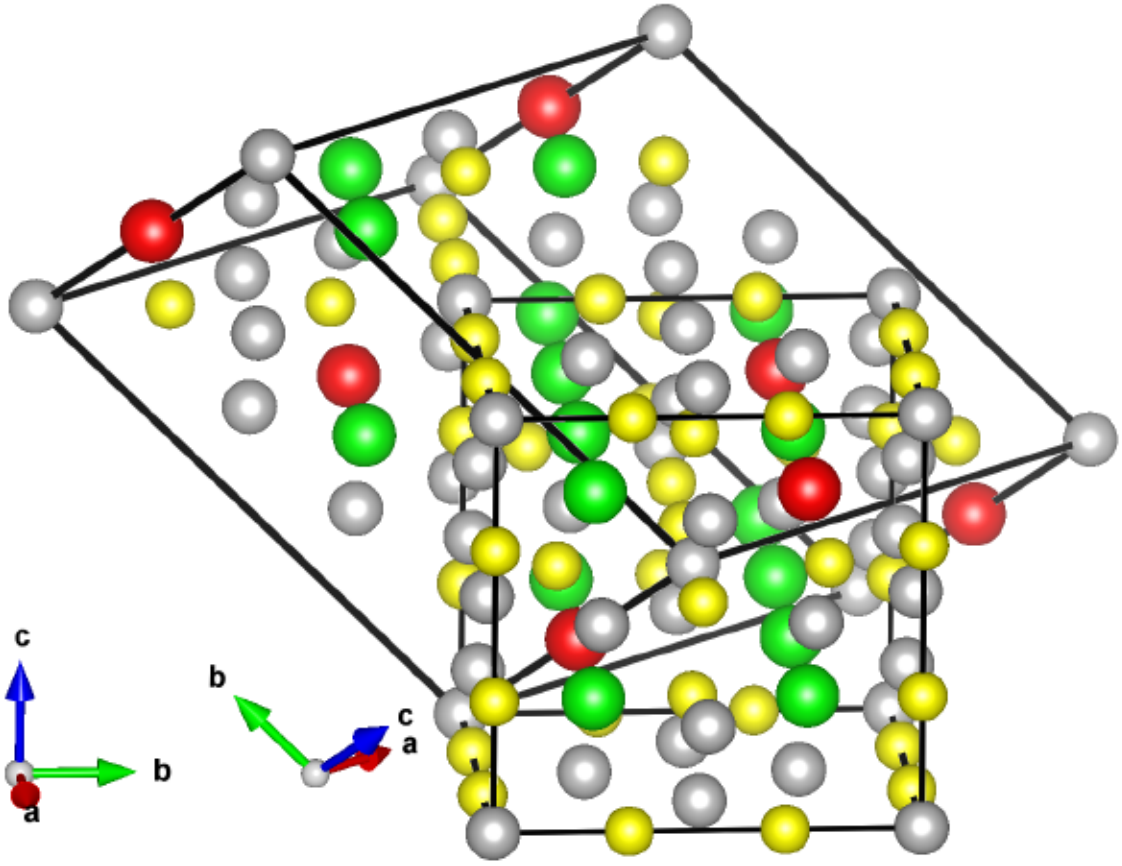

Figure 7.16: Mutual orientation of the cubic $Im\bar{3}m$ unit cell and the rhombohedral $R\bar{3}m$ in the hexagonal axes. U1 sites are marked red, U2 green, Ru1 and Ru2 gray, and Ge are yellow.

Table 7.2: Summary of the structural transformation between $Im\bar{3}m$ and $R\bar{3}m$ spacegroup. Underlined coordinates in the $R\bar{3}m$ spacegroup are free parameters and are thus connected with the distortion.

$Im\bar{3}m$		$R\bar{3}m$, hexagonal axes	
U $8c$	(0.25, 0.25, 0.25)	U1 $3b$	(0, 0, 0.5)
		U2 $9d$	(0.5, 0, 0.5)
Ru1 $2a$	(0,0,0)	Ru1 $3a$	(0, 0, 0)
Ru2 $12d$	(0.25, 0, 0.5)	Ru2 $18g$	$(\underline{x_{\mathrm{Ru2}}}, 0, 0.5)$, $\underline{x_{\mathrm{Ru2}}} \sim 0.25$
Ge $12e$	$(x_{\mathrm{Ge}}, 0, 0)$, $x_{\mathrm{Ge}} \sim 0.31$	Ge $18h$	$(\underline{\frac{x_{\mathrm{Ge}}}{3}}, \underline{\frac{-x_{\mathrm{Ge}}}{3}}, \underline{\frac{-2x_{\mathrm{Ge}}}{3}})$
$a_{\mathrm{cub}}, V_{\mathrm{cub}}$		$\vec{a}_{\mathrm{hex}} = \vec{b}_{\mathrm{cub}} - \vec{a}_{\mathrm{cub}}$, $a_{\mathrm{hex}} = \sqrt{2}a_{\mathrm{cub}}$ $\vec{a}_{\mathrm{hex}} = \frac{1}{2}\left(\vec{a}_{\mathrm{cub}} + \vec{b}_{\mathrm{cub}} + \vec{c}_{\mathrm{cub}}\right)$, $c_{\mathrm{hex}} = \frac{\sqrt{3}}{2}a_{\mathrm{cub}}$ $V_{\mathrm{hex}} = \frac{3}{2}V_{\mathrm{cub}}$	
$(h,k,l)_{\mathrm{hex}} = (h,k,l)_{\mathrm{cub}} \begin{pmatrix} -1 & 0 & \frac{1}{2} \\ 1 & -1 & \frac{1}{2} \\ 0 & 1 & \frac{1}{2} \end{pmatrix}$			

which is $-3\mathrm{m}$ (primary direction of the rhombohedral lattice in the hexagonal axes is $\{001\}_{\mathrm{hex}}$ that is in our case parallel with the $\{111\}_{\mathrm{cub}}$ and secondary direction is $\{100\}_{\mathrm{hex}}$, parallel with the $\{110\}_{\mathrm{cub}}$) while the U2 site has only $.2/\mathrm{m}$ and the hexagonal arrangement of the Ru ions is distorted. This distortion leads to the emergence of two different distances between U2 and $\mathrm{Ru2_{hex}}$ sites. The first one depends only on the lattice parameter a_{hex} as $\mathrm{d(U2 - Ru2_{hex,1}) = a_{hex} \cdot (0.5 - x_{Ru2})}$, while the second one varies as $\mathrm{d(U2 - Ru2_{hex,2})} = \sqrt{\frac{1}{48}\mathrm{a_{hex}^2} + \frac{1}{9}\mathrm{c_{hex}^2}}$. The unique distance between U1 and $\mathrm{Ru2_{hex}}$ is described in a similar way as $\mathrm{d(U1 - Ru2_{hex}) = a_{hex} \cdot x_{Ru2}}$. It has an effect on the local coordination of the U1 and U2 sites. Example of the number of atoms around the U1 and U2 sites as a function of the radial distance is presented in the form of histograms in Figure 7.17. The histograms show the number of atoms in the given radial distance from the U1 and U2 site, respectively, for the chosen lattice parameters $\mathrm{a_{hex}} = 11.6476\,\text{Å}$ and $\mathrm{c_{hex}} = 7.2054\,\text{Å}$. The difference between the corresponding cubic lattice parameters $\mathrm{a_{cub}}$ calculated separately from the $\mathrm{a_{hex}}$ and $\mathrm{c_{hex}}$ is 1%. This exaggerated value is used for illustrative representation of the distortion. The histograms show, that the U2 site has less regular local structure leading to reduced degeneracy of the mutual distances with other types of atoms.

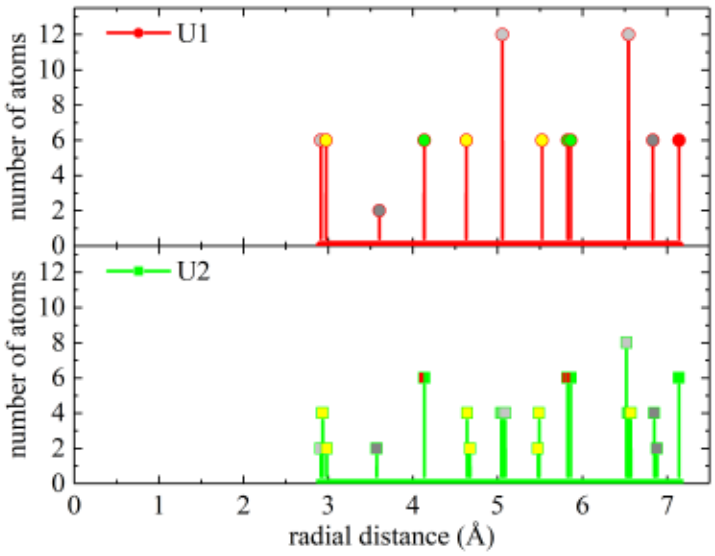

Figure 7.17: Histograms of the number of atoms at the given distance from the U1 and U2 site, respectively. Colors of the point represent appropriate element/positions as in Figure 7.16 a) (i.e. Ge – yellow, Ru1 – dark gray, Ru2- light gray, U1 – red, U2 – green)

One should notice that the proposed small distortion does not cause the appearance of any additional Bragg reflections within the experimental sensitivity of the diffraction experiments. It only introduces different rules for merging of the equivalent reflections. This was confirmed using the neutron Laue diffractometer CYCLOPS at ILL, Grenoble, where no additional reflections down to 2 K were observed. Figure 7.18 shows the Laue patterns measured at the paramagnetic state at 15 K (top) and at the ordered state at 2 K (bottom).

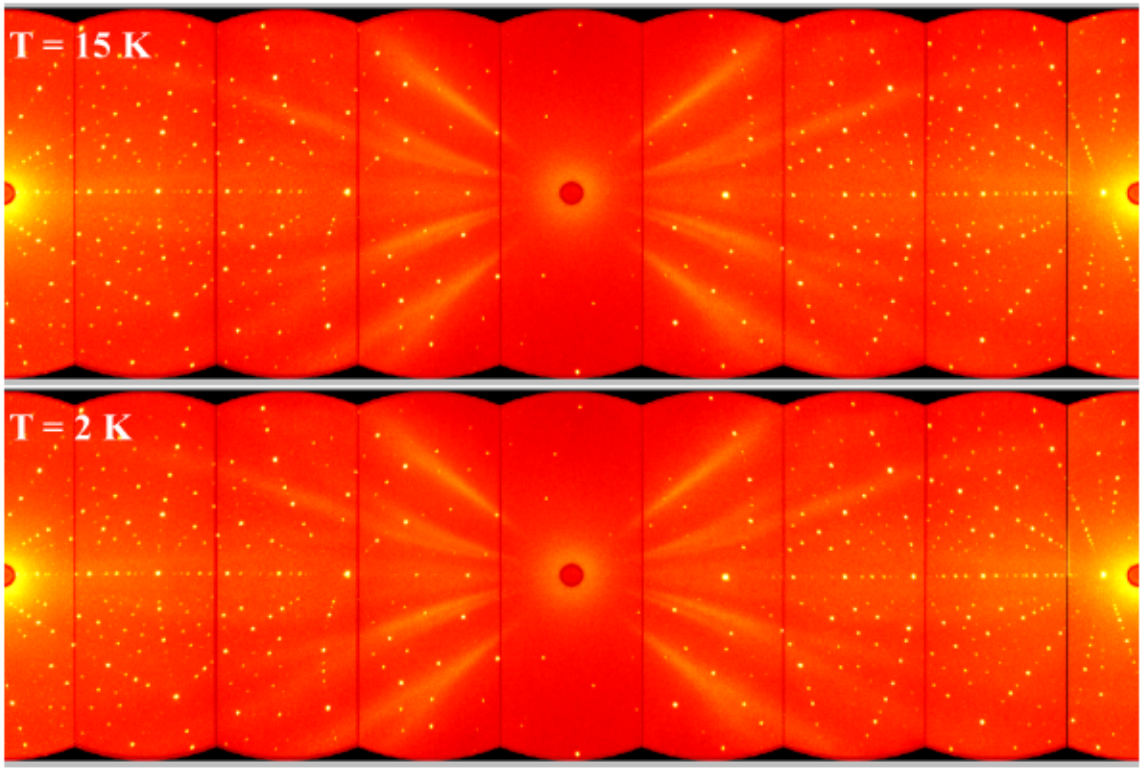

Figure 7.18: Laue patterns recorded at 15 K in the paramagnetic state (top) and at 2 K in the ordered state (bottom).

The unpolarized neutron diffraction experiment was performed on D9 diffractometer at ILL, Grenoble with the wavelength of $\lambda = 0.841$ Å. The absorption and extinction correction were applied on the all measured data. Total number of 371(216) inequivalent reflections assuming a $R\bar{3}m$ ($Im\bar{3}m$) space group was obtained. The internal agreement factor of the equivalent reflections was 4.74% (6.43%) at 1.9 K and 3.50% (4.40%) at 20 K for $R\bar{3}m$ ($Im\bar{3}m$) space group. It was thus always slightly better using the distorted $R\bar{3}m$ space group, even in the paramagnetic phase.

As the intensities at 1.9 K (ordered state) should be affected both by nuclear and magnetic contribution, the temperature dependence of four different strong reflections from 15 K down to 1.9 K was measured. Their intensity did not show any significant change. Such observation is acceptable since the spontaneous magnetic moment of $U_4Ru_7Ge_6$ is only $0.85\,\mu_B$/f.u.. The reflections were also treated with a large enough scattering vector, *i.e.* $\frac{\sin\theta}{\lambda} > 0.6\,\text{Å}^{-1}$, separately. These should be much less affected by the magnetic contribution as was later confirmed by polarized neutron experiment where reflections above this value showed flipping ratios close to 1 (see Section 7.2.7). The comparison of the resulting calculated intensities versus the measured ones is plotted in Figure 7.19.

The breaking of symmetry can lead to the existence of the twins (4 types of the domains in this case). This possibility was checked and the data data were refined including these four twin components. However, based on the twin domain fractions obtained for each twin domain [97(2) : 0(2) : 0(1) : 3 %] it can be concluded that after

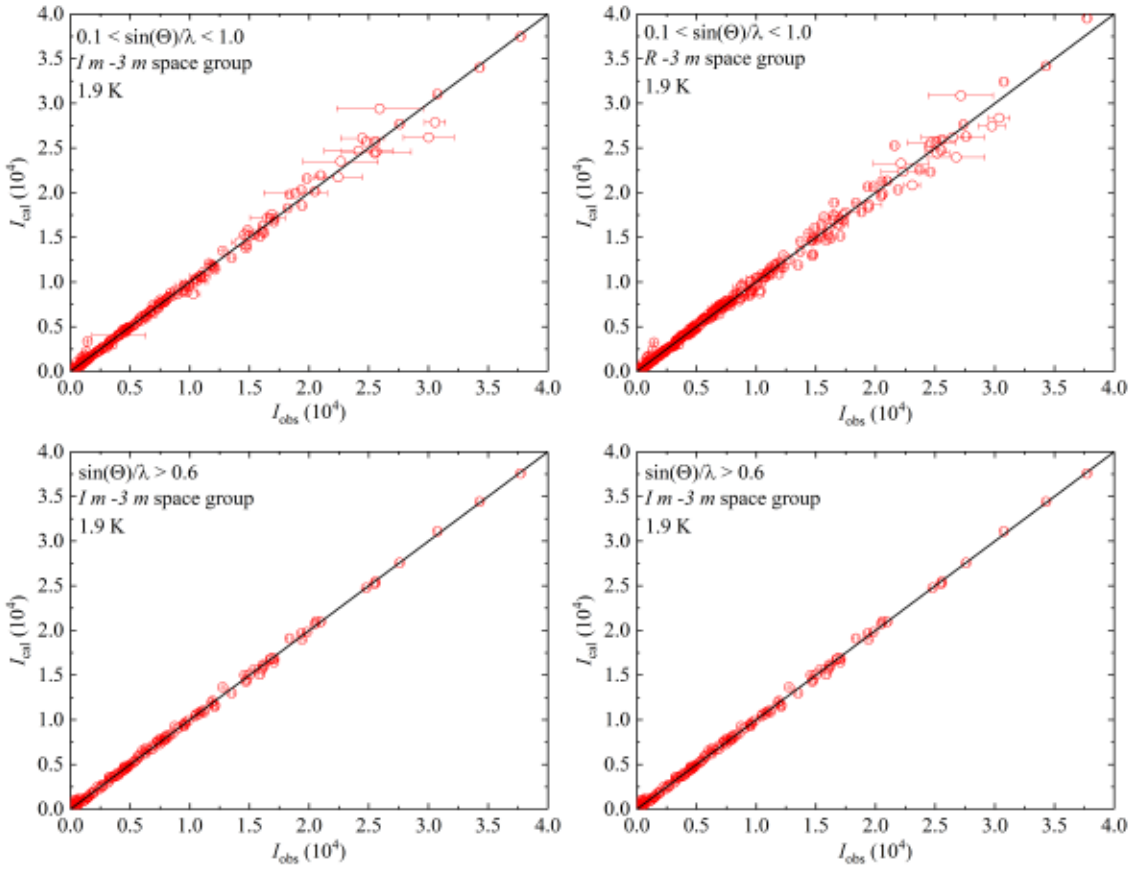

Figure 7.19: Comparison of the calculated intensities I_{cal} with the measured ones I_{obs} for the data measurement at 1.9 K. Top row shows the treatment of the whole data set with the cubic $Im\bar{3}m$ space group (left) and rhombohedral $R\bar{3}m$ space group (right). The bottom row are the data with the reduced data set with $q > 0.6\,\text{Å}^{-1}$.

Table 7.3: Structural parameters and isotropic temperature factors B_{iso} obtained from the refinement of the neutron diffraction data, together with the corresponding agreement factors R_F. The rows labeled as 20 K and 1.9 K show results for refinement using the whole set of reflections, while the one labeled as 1.9 K† shows results only for the reflections with $q > 0.6\,\text{Å}^{-1}$.

$Im\bar{3}m$							
	B_{iso} [Å^2]				x_{Ge}		R_F
	U		Ru1	Ru2	Ge		
20 K	0.075(12)		0.120(12)	0.130(27)	0.120(12)	0.3114(1)		3.72
1.9 K	0.066(12)		0.117(12)	0.127(28)	0.115(12)	0.3115(1)		3.66
1.9 K†	-0.049(10)		0.006(7)	0.020(13)	0.001(7)	0.3115(1)		3.05
$R\bar{3}m$							
	B_{iso} [Å^2]					x_{Ge}	x_{Ru2}	R_F
	U1	U2	Ru1	Ru2	Ge			
20 K	0.060(23)	0.106(26)	0.090(10)	0.094(10)	0.039(12)	0.3117(2)	0.2500(1)	4.05
1.9 K	0.057(23)	0.031(12)	0.088(25)	0.096(10)	0.093(10)	0.3114(2)	0.2500(1)	3.98
1.9 K†	0.006(17)	0.016(11)	0.067(18)	0.045(10)	0.055(10)	0.3112(1)	0.2498(1)	3.32

the phase transition the sample remains mainly as a single domain.

The structure was refined from the measured integrated intensities, corrected for absorption, using the FullProf software package [41,42], including extinction corrections and isotropic temperature factors B_{iso}. The B_{iso} parameter is proportional to the root mean square displacement of the atom from its average position. The results are summarized in Table 7.3, with different agreement factors R_F for the cubic ($Im\bar{3}m$) and rhombohedral ($R\bar{3}m$) space groups. The crystallographic R_F factor is defined as a sum of the absolute values of differences between observed and calculated structure factors divided by the sum of the absolute values of the observed structure factors and multiplied by 100. The negative isotropic temperature factor B_{iso} for U ion at 1.9 K, when only reflections with $\frac{\sin\theta}{\lambda} > 0.6\,\text{Å}^{-1}$ are assumed, is consistent with the model of loss of the cubic symmetry in the ground state. Nevertheless, it can not be taken as a clear evidence for the structure change. A possible site mixing was also checked with no significant effect on the agreement factors. The crucial importance of the performed neutron diffraction study was the structure determination as precise as possible, including the extinction and absorption correction, on the same crystal and at the same temperature as in the following polarized neutron experiment.

7.2.7 Magnetic moments studied by polarized neutrons

The flipping ratio method using a polarized neutron beam is a powerful tool to study small magnetic moments. Its principle is described in Section 6.2. It is based on the measurement of the flipping ratio $R = \frac{I^+}{I^-}$ of scattered intensities I^+ and I^-, with primary beam polarized parallel (+) or antiparallel (-) to the applied vertical field direction. It was performed on the D3 diffractometer at ILL, Grenoble using the wavelength of $\lambda = 0.85\,\text{Å}$. The absorption and extinction correction were applied on the all measured data. The magnetic easy axis of $U_4Ru_7Ge_6$ at the ground state is $[111]_{cub}$ (i.e. $[001]_{hex}$). The sample was thus aligned to have the external vertical magnetic field parallel to that direction. A set of flipping ratios was collected at the same temperatures (1.9 K and 20 K) as in the unpolarized experiment. The applied magnetic field was 1 T and 9 T for both measured temperatures.

The obtained results were treated both with respect to cubic $Im\bar{3}m$ and rhombohedral $R\bar{3}m$ space group. While merging the equivalent flipping ratios obtained in 9 T and 1.9 K within rhombohedral $R\bar{3}m$ space group leads to the 78 independent values with internal agreement factor of 1 %, the same approach for cubic $Im\bar{3}m$ space group gives 52 independent values with a degraded 3.5 % internal agreement factor. The inadequacy of the cubic description can be further illustrated by the example of the two reflections with dramatically different flipping ratios. These are namely $(030)_{hex}$ reflection with $R = 1.28(2)$ and $(211)_{hex}$ with $R = 0.79(2)$ as two inequivalent ones in the $R\bar{3}m$ space group. But according to the $Im\bar{3}m$ space group, they should be equivalent within the $\{2-11\}_{cub}$ family. It clearly shows, that cubic space group $Im\bar{3}m$ cannot be used to describe the ground state of $U_4Ru_7Ge_6$. Same result was observed for the data obtained at 1.9 K in 1 T and at 20 K and 9 T. We will thus focus only on the description using rhombohedral $R\bar{3}m$ space group in following treatment of polarized neutron data, both using maximum entropy calculations or direct flipping ratios refinement.

Maximum entropy method (MAXENT)

The maximum entropy approach is not affected by any prior assumption of the distribution of magnetic density. Its only inputs are the symmetry and dimensions of the unit cell and the magnetic structure factors obtained from the measured flipping ratios. Its principle is described in Section 6.2. In this case the whole unit cell was divided in to 235 x 235 x 145 separated voxels. The initial state was a flat magnetic density distribution over the unit cell. The results are plotted using the VESTA software[120]. The resulting three-dimensional spin density map agrees with the experimental magnetic structure factors and has maximal entropy. Figure 7.20 shows the spin density map obtained at 9 T and 1.9 K in a slice perpendicular to the $[001]_{hex}$ axis at the fractional coordinate $z = \frac{5}{6}$. This slice truncates both the U1 and U2 ions and evidences a density almost three times higher on the U2 sites than on the U1 site: $\sim 0.24\,\mu_B\,\text{Å}^{-3}$ and $\sim 0.078\,\mu_B\,\text{Å}^{-3}$ respectively, at the center.

Integration in the spherical region around the given atomic position can serve as a rough estimation of the magnetic moments associated to each site. Such integration

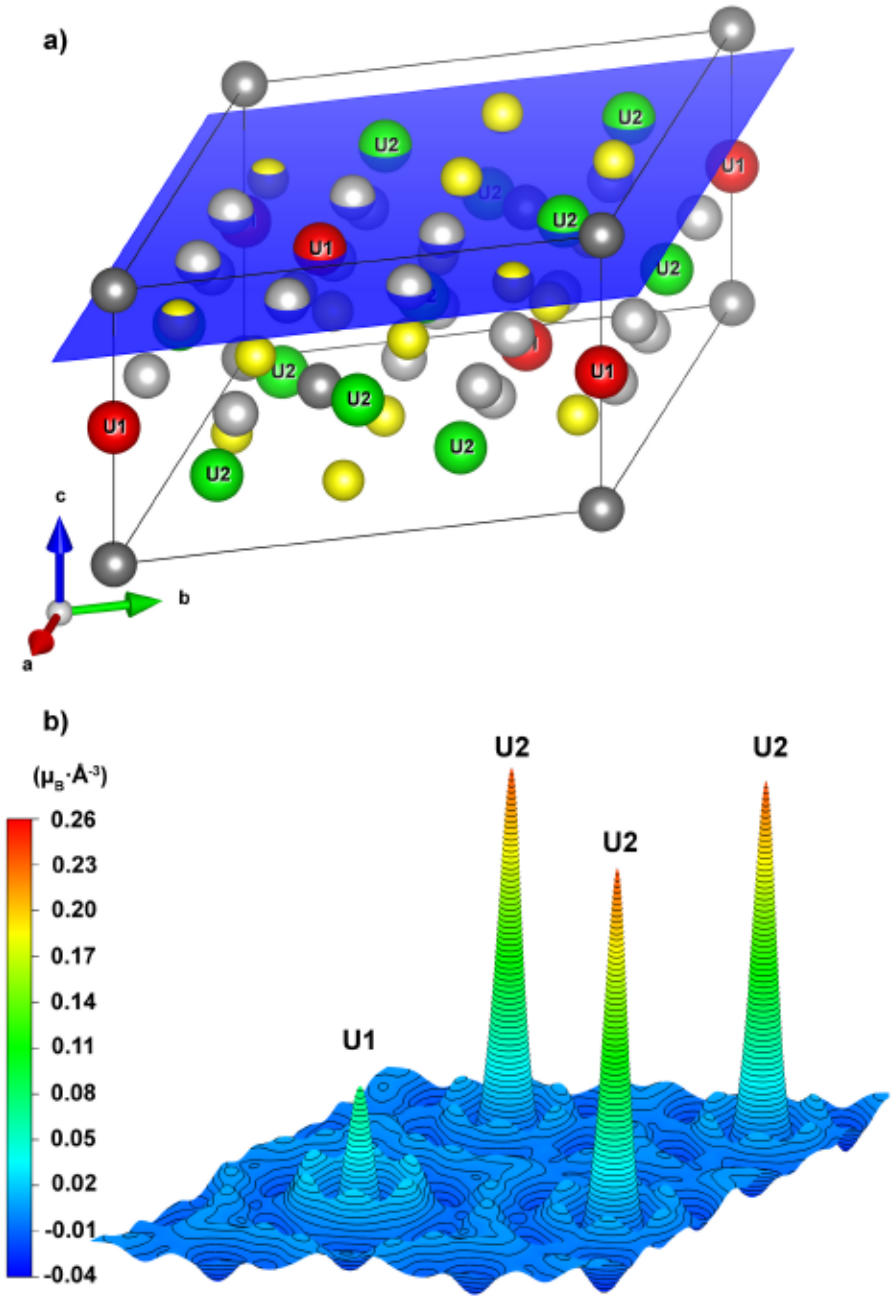

Figure 7.20: a) Indicated section in the $R\bar{3}m$ space group representation, that is perpendicular to the $[001]_{\text{hex}}$ axis. b) Corresponding MAXENT magnetization density map measured in 9 T and 1.9 K. Contour lines are at $0.004\,\mu_{\text{B}}\,\text{Å}^{-3}$.

was performed in the sphere with gradually increasing radius. The obtained magnetic moment μ showed saturation around ~ 1.8 Å for the U1 position and ~ 0.8 Å U2 position being constant up to ~ 1.8 Å. This value was chosen as the limit for integration r_{max} and is close to the experimental atomic radius of 1.75 Å of uranium[121]. The integrated magnetic moments as a function of the radius are plotted in Figure 7.21.

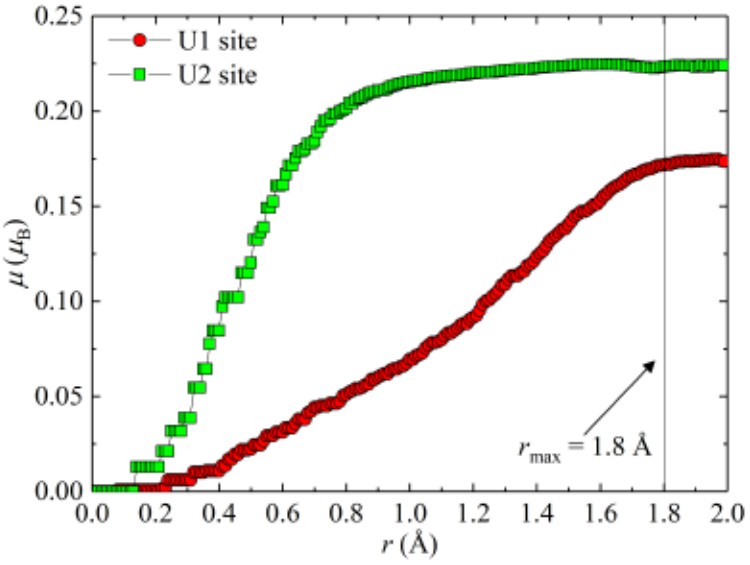

Figure 7.21: Integrated magnetic moment μ from the MAXENT spin density map for the U1 and U2 site as a function of the sphere radius r up to the limit r_{max}.

Integrated values are $0.17(1)\,\mu_B$ and $0.22(1)\,\mu_B$ for the U1 and U2 site at 9 T and 1.9 K, respectively. Qualitatively comparable results were obtained for the measurement at 1.9 K and 1 T and at 20 K, and 9 T. All obtained spin density maps are compared with the same scale in Figure 7.22. All values are summarized in Table 7.4.

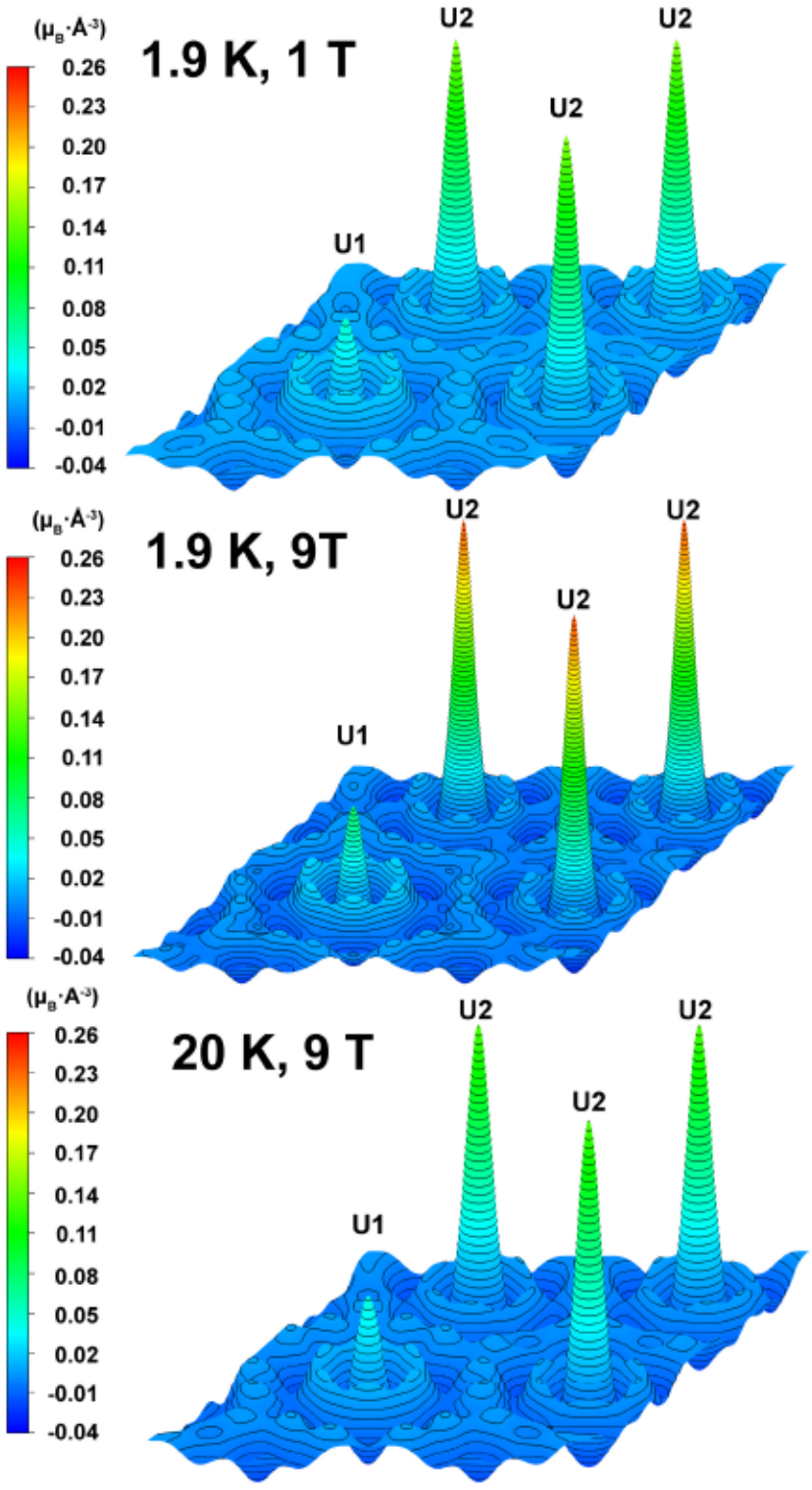

Figure 7.22: MAXENT magnetization density maps measured in 1 T and 1.9 K, 9 T and 1.9 K and 9 T and 20 K. All maps have the same scale and contour lines are at $0.004\,\mu_B\,\text{Å}^{-3}$.

Direct refinement of the flipping ratios

To describe the magnetic structure of $U_4Ru_7Ge_6$ in more detail and distinguish between the spin μ_S and orbital μ_L components of the magnetic moments the measured flipping ratios were compared with a model, in the dipolar approximation as was described in Section 6.2. The least squares refinement was performed using the FullProf/WinPlotr[41,42] software. The magnetic form factor was characterized by Equation (6.21) using the tabulated values of $\langle j_0(\boldsymbol{r})\rangle$ and $\langle j_2(\boldsymbol{r})\rangle$ corresponding to the Ru^{1+} for ruthenium and either the U^{3+} or the U^{4+} values for uranium (although the actual valence of uranium in $U_4Ru_7Ge_6$ may be different)[122]. With this method, the corresponding spin μ_S and orbital μ_L magnetic moments were obtained.

The assumed ground-state space group $R\bar{3}m$ of $U_4Ru_7Ge_6$ has two different U and Ru sites but, according to the symmetry, every reflection has a contribution from all four sites, and one has to include them all at once into the least squares fit. Best fits for the all experimental conditions were obtained assuming a U^{3+} form factor, although the difference between U^{3+} and U^{4+} form factor is very small[123]. The results are summarized in Table 7.4. The measured and calculated flipping ratios are plotted in Figure 7.23 for 1 T and 1.9 K, 9 T and 1.9 K and 9 T and 20 K.

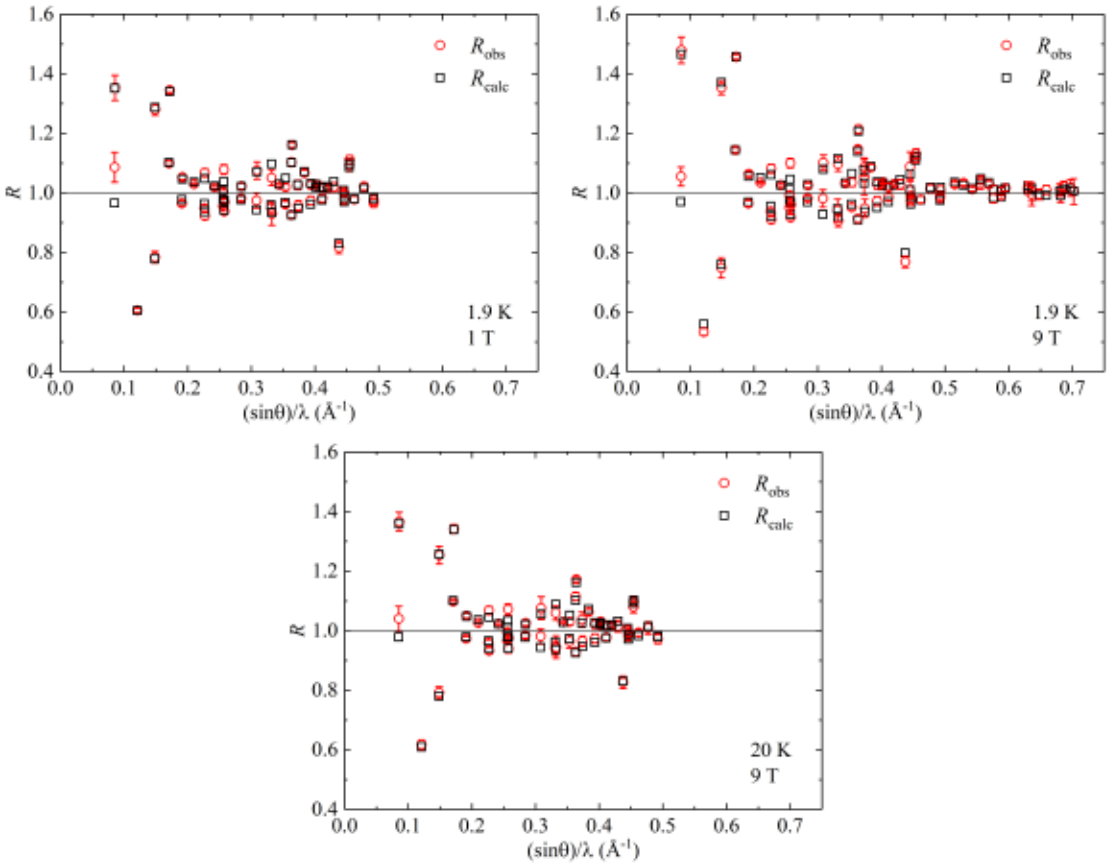

Figure 7.23: Flipping ratios measured at 1.9 K and 1 T, 1.9 K and 9 T and 20 K and 9 T compared with the calculated values using the dipolar approximation.

Table 7.4: Magnetic moments calculated from DFT, obtained by MAXENT and from the direct fitting of the flipping ratios using dipolar approximation in 1 T and 9 T at 1.9 K and 20 K. All values are in the μ_B and signs of the magnetic moments are consistent for all methods.

	DFT	MAXENT			Dipolar approximation		
	GGA	1 T 1.9 K	9 T 1.9 K	9 T 20 K	1 T 1.9 K $\chi^2 = 1.27$	9 T 1.9 K $\chi^2 = 1.49$	9 T 20 K $\chi^2 = 1.02$
Atom mult.	μ_S μ_L μ	μ	μ	μ	μ_S μ_L μ	μ_S μ_L μ	μ_S μ_L μ
U1 1	-0.657				0.17(4)	0.23(5)	0.15(4)
	0.554	0.11(1)	0.17(1)	0.10(1)	-0.04(4)	-0.05(4)	-0.02(4)
	-0.103				0.129(9)	0.18(1)	0.13(1)
U2 3	-0.820				-0.26(2)	-0.28(3)	-0.26(2)
	1.021	0.16(1)	0.22(1)	0.14(1)	0.43(2)	0.51(2)	0.43(2)
	0.201				0.176(6)	0.230(8)	0.172(6)
Ru1 1	-0.110				0.04(4)	0.00(5)	0.00(4)
	-0.005	-	-	-	-0.03(4)	0.00(4)	0.00(4)
	-0.115				0.01(1)	0.00(2)	0.00(1)
Ru2 6	0.119				0.07(2)	0.11(2)	0.09(1)
	0.009	-	-	-	-0.05(2)	-0.08(2)	-0.07(1)
	0.128				0.021(5)	0.030(6)	0.024(4)
Ge 6	0.009				-	-	-
	0.004	-	-	-	-	-	-
	0.013				-	-	-
μ_{sum}	1.231	0.85(2)	1.05(2)	0.84(2)	0.79(4)	1.02(4)	0.79(4)
μ_{bulk}		0.94(1)	1.25(1)	0.98(1)	0.94(1)	1.25(1)	0.98(1)

In the ordered state the spin and orbital moments on the U2 site are antiparallel with a dominant orbital contribution leading to a ratio of $\frac{\mu_L}{\mu_S} = -1.7(2)\,(-1.8(2))$ and parameter C_2 reaches a value of $2.5(1)\,(2.3(1))$ at $1\,\mathrm{T}$ ($9\,\mathrm{T}$).

The orbital component of the magnetic moment on the U1 site is very small: $-0.04(4)\,\mu_B$ and $-0.05(4)\,\mu_B$ at $1\,\mathrm{T}$ and $9\,\mathrm{T}$, respectively. Together with the dominating spin component it gives a very unusual value of the ratio of $\frac{\mu_L}{\mu_S} = -0.2(2)\,(-0.2(2))$ that means very small and negative parameter $C_2 = -0.3(3)\,(-0.3(2))$.

The resulting magnetic moment on the Ru1 position is negligible both in $1\,\mathrm{T}$ and $9\,\mathrm{T}$. On the other hand the Ru2 position shows a clear induced moment ($0.021(5)\,\mu_B$ and $0.030(6)\,\mu_B$ for $1\,\mathrm{T}$ and $9\,\mathrm{T}$, respectively).

The bulk magnetization value μ_{bulk} at $2\,\mathrm{K}$ resulting from the magnetometry measurements increases by a factor 1.3 between $1\,\mathrm{T}$ ($0.94(1)\,\mu_B$) and $9\,\mathrm{T}$ ($1.25(1)\,\mu_B$). This scaling is valid within the experimental error, for all the fitted magnetic moments of the U and Ru ions. The resulting total magnetic moments per formula unit, $\mu_{sum} = \mu_{U1} + 3\mu_{U2} + \mu_{Ru1} + 6\mu_{Ru2}$ are $0.79(4)\,\mu_B$ and $1.02(4)\,\mu_B$ for $1\,\mathrm{T}$ and $9\,\mathrm{T}$, respectively, smaller than the bulk magnetization values. The residual moment $\mu_{res} = \mu_{bulk} - \mu_{sum}$ can be attributed to the polarization of the conduction electrons. Due to the large spatial extent of the conduction electrons their form factor vanishes around $\frac{\sin\theta}{\lambda} = 0.1\,\mathrm{\AA}^{-1}$[124] and cannot be observed in our neutron diffraction experiments. This μ_{res} value is $0.15(4)\,\mu_B$ and $0.23(4)\,\mu_B$ for $1\,\mathrm{T}$ and $9\,\mathrm{T}$, respectively reaching $\sim 17\%$ of the bulk magnetic moment for both cases.

The bulk magnetic moment above the ordering temperature at $20\,\mathrm{K}$, induced by the external magnetic field of $9\,\mathrm{T}$, is $0.98(1)\,\mu_B$. This value is close to the moment in the ordered state at $1.9\,\mathrm{K}$ in the field of $1\,\mathrm{T}$, which reaches the value of $0.94(1)\,\mu_B$. The analysis of the flipping ratios obtained in these conditions, i.e. above T_C, at $20\,\mathrm{K}$ and $9\,\mathrm{T}$, gives comparable results to those obtained at $1.9\,\mathrm{K}$ and $1\,\mathrm{T}$, i.e. the U1 and U2 position shows remarkably different magnetic moments. Results of the fit are summarized in Table 7.4.

7.3 Discussion

The $M(\mu_0 H)$ curve measured for the hard magnetization direction [001] merges with the easy-magnetization direction [111] curve near $0.3\,\mathrm{T}$ as seen in Figure 7.2. This anisotropy field of $U_4Ru_7Ge_6$ is unprecedentedly the lowest value ever observed for a uranium intermetallic compound. Moreover, an entirely isotropic paramagnetic susceptibility and electrical resistivity was also observed, which has not been reported for any uranium $5f$-electron ferromagnet

One may argue that the almost isotropic magnetism in $U_4Ru_7Ge_6$ is a consequence of the itinerant character of U $5f$-electron magnetic moment. The spontaneous magnetic moment of this compound is $\sim 0.85\,\mu_B$/f.u., which provides an average moment of $\sim 0.21\,\mu_B$/U ion when supposing negligible contributions from Ru and Ge ions. This value is 4 times larger than the U-born magnetic moment of the itinerant $5f$ electron ferromagnet UNi_2[80,89–91] which in contrast exhibits a huge magnetocrystalline anisotropy with the anisotropy field $\gg 35\,\mathrm{T}$[91].

Both the magnetization data and ab initio calculations clearly show that easy magnetization direction of $U_4Ru_7Ge_6$ in the ground state is [111]. As a result of magnetoelastic interaction[125], the ferromagnetic ordering at temperatures below T_C is accompanied by the spontaneous magnetostriction causing a distortion of a crystal lattice related to the easy-magnetization direction. These distortions are common in ferromagnetic materials possessing cubic crystal structure in a paramagnetic state (at temperatures $T > T_C$). The spontaneous magnetostriction leads to a distortion lowering the paramagnetic cubic to tetragonal, orthorhombic and rhombohedral symmetry for the [001]-, [110]- and [111]-easy-magnetization direction, respectively. The expected rhombohedral distortion of the cubic $U_4Ru_7Ge_6$ lattice in the ferromagnetic ground state is so tiny that it falls within the experimental error of a standard x-ray diffraction, but is clearly indicated by thermal expansion results at low temperatures. As a consequence of the distortion, the one equivalent crystallographic site common for all U ions in the cubic lattice splits into two inequivalent ones, which is confirmed by ab initio calculations.

Our magnetization results also reveal that the easy-magnetization direction holds onto the [111] axis only at low temperatures up to T_r ($= 5.9\,\mathrm{K}$), whereas at higher temperatures up to T_C the easy-magnetization direction is unambiguously along [001] and the paramagnetic cubic lattice is tetragonally distorted along this direction. This finding is in good agreement with the theoretical calculations, which reveal the excited state with the [001] easy magnetization $0.9\,\mathrm{meV}$ above the ground state. The calculated total energy is the sum of positive kinetic energy and negative potential energy and negative exchange correlation energy. The difference of kinetic energy for the [111] and [001] direction is $59.27\,\mathrm{meV}$, of potential energy is $-53.67\,\mathrm{meV}$, and of exchange correlation energy is $-6.50\,\mathrm{meV}$.

The magnetic moment reorientation transition in $U_4Ru_7Ge_6$ at T_r is manifested in specific features (anomalies) which were observed in the temperature dependencies of magnetization (Figure 7.4 (a)), AC susceptibility (Figure 7.4 (b)), specific heat (Figure 7.8), thermal expansion (Figure 7.9) and electrical resistivity (Figure 7.14). It is in fact an order-to-order magnetic phase transition accompanied by structural distortion due to notable magnetoelastic coupling. These phase transitions are known to be of the first order type (e.g. $HoAl_2$[126]). The thermal expansion anomalies seen in Figure 7.9 at T_C and T_r, respectively, may be viewed as an illustrative examples of the second and first order type phase transitions. However, the first order phase transition is to be accompanied by latent heat, which was not detect by desired detailed specific-heat measurement and the T_r related specific-heat anomaly is considerably broader than expected for a first order phase transition. The lack of observables pointing to the presence of latent heat is attributed to the complex domain structure processes during the spin reorientation in the multidomain sample in the vicinity of T_r. Crystal imperfections acts as nucleation centers leading to random population of equivalent domains within a finite temperature window, effectively smearing out the latent heat contribution over a finite temperature range making it difficult to observe experimentally. The tentative determination has to be confirmed by a designed method allowing indication of coexistence of the [001] and [111] phases in the vicinity of T_r, which would resolve the issue of the phase transition

order. It might be observable in μSR spectra, in which the different signals from the [001] and [111] phase should be visible. Results that can be achieved by a μSR experiment, however, strongly depends on the actual stopping site(s) of the muon in the $U_4Ru_7Ge_6$ lattice.

The anisotropy field values in U ferromagnets are typically hundreds of Tesla, whereas in $U_4Ru_7Ge_6$ it is roughly three orders of magnitude smaller. When inspecting crystal structures it was found that in all cases of the U ferromagnets characterized by high values of anisotropy field the U ions have some U nearest neighbors. Contrary, the individual U ions in $U_4Ru_7Ge_6$ are buried inside the Ru and Ge polyhedra thereby preventing direct connection to any nearest U ion which should have consequences for magnetism [46].

The direct $5f$-$5f$ overlap of U electron orbitals is probably behind the huge magnetic anisotropy of other U compounds. The symmetry of the network of U nearest neighbors determines the type of magnetic anisotropy in these materials [22]. The very weak MA in $U_4Ru_7Ge_6$ is apparently due to the lack of the direct overlap of $5f$ wave-functions of the nearest U neighbors (direct $5f$-$5f$ overlap). The symmetry of the hybridization of U $5f$-electron states with the $4d$-electron states of surrounding Ru ions, which are in a hexagonal arrangement perpendicular to the [111] axis, determines the [111] easy magnetization direction.

Onset of itinerant electron ferromagnetism is usually accompanied by a positive spontaneous magnetovolume effect [127,128]. Also the thermal expansion data show this tendency despite the negative value of $\lambda_{S[001]}$. Unfortunately, the measurements using a dilatometer cannot be extended to temperatures lower than T_r because the body diagonals representing the [111] easy magnetization direction are not perpendicular and therefore an experiment analogous to that for $T_r < T < T_C$ is not accessible.

Strong hydrostatic pressure dependence was observed both for T_r and T_C transition (see Figure 7.15). The expected extrapolated value of critical pressure for T_r transition is $p_{cr,Tr} \approx 1.4\,\mathrm{GPa}$ while T_C is suppressed to $0\,\mathrm{K}$ at $p_{cr,TC} \approx 2.8\,\mathrm{GPa}$. Similar critical pressure for T_C was observed on polycrystalline sample by Hidaka et al. [104] where QCP is expected around $2.6\,\mathrm{GPa}$ while T_r was not traced in their data. More detailed study on single crystals under pressure and at lower temperatures to verify the presence of QCP is currently in progress.

Using unpolarized neutron single crystal diffraction methods is not sufficient to undoubtedly solve the ground-state structure of the system, as the proposed distortion of the cubic structure is very small (in the order of 10^{-6}). Comparison of the agreement factors R_F for the $Im\bar{3}m$ and $R\bar{3}m$ space group actually favors the cubic structure both in the ordered state and above T_C (see Table 7.3). However, this may be biased by the fact that the number of inequivalent reflections is much higher for the rhombohedral structure, and the internal agreement factor for the equivalent reflections was always worse for the cubic structure model. The value of the fractional coordinate $x_{Ru2_{hex}}$, that is not fixed in the distorted structure, is close to the value of 0.25 given by symmetry in the cubic description, for both the measurements at $20\,\mathrm{K}$ and $1.9\,\mathrm{K}$. It thus keeps the $d(U1 - Ru2_{hex})$ and $d(U2 - Ru2_{hex,1})$ distances almost equal and the largest effect of the interatomic distance change can be expected for $d(U2 - Ru2_{hex,2})$ that is controlled only by the change of the lattice parameters a_{hex}

and $\mathbf{c_{hex}}$. This variation of the lattice parameters was revealed as a strong evidence for the distortion observed the precision measurement of the thermal expansion [105]. Further proof is brought by the polarized neutron study, which clearly evidences two uranium sites with drastically different magnetic moments. Further detailed structural study of this compound, like high-resolution x-ray diffraction, is desired.

The first-principle calculations clearly shows the necessity to incorporate the spin-orbit interaction while treating the uranium-based intermetallics. Previous calculations of magnetic moments performed on the $\mathbf{U_4Ru_7Ge_6}$ omitted the relativistic effects[46]. This spin only approach naturally deals with the only one U position as the lack of spin-orbit interaction does not lower the symmetry. It gives a total magnetic moment of $\sim 2.72\,\mu_B$/f.u. that overestimates the experimental bulk value. The results using GGA give a total magnetic moment of $\sim 1.23\,\mu_B$/f.u., much closer to the bulk magnetization value ($\sim 1.25\,\mu_B$/f.u. at 1.9 K and 9 T). The spin-orbit interaction also leads to the appearance of the two distinct U sites (U1 and U2), in agreement with the proposed rhombohedral distortion. The DFT calculations show antiparallel alignment of the spin and orbital magnetic moments both on the U1 and U2 sites (see Table 7.4). This is expected from the third Hund's rule [29] for systems with less than half-filled shells. The spin moments on the U1 and U2 sites are parallel. However, the total magnetic moment of the U1 site is expected to be dominated by its spin component, leading to a mutually antiparallel alignment of the U1 and U2 total moments and resulting in a ferrimagnetic structure in the ground state of $\mathbf{U_4Ru_7Ge_6}$. Such a behavior was observed by neutron powder diffraction in the case of $\mathbf{UCu_5Sn}$ where two different U sites possess antiparallel collinear magnetic moments of dramatically different magnitudes of $2.14(2)\,\mu_B$/f.u. on the 2a and $0.18(4)\,\mu_B$/f.u. on the 2c position [129]. It is believed to be caused by Kondo screening, acting strongly on the 2c position. Availability of only unpolarized neutron data prevented the authors from distinguishing between the spin and orbital components.

The polarized neutron diffraction results are in good qualitative agreement with the DFT calculations and gives independent and clear experimental evidence of the presence of two different U sites, excluding the cubic $Im\bar{3}m$ space group as a proper ground-state structure. However, while both the maximum entropy calculations and a direct fit of the flipping ratios clearly show a different density of magnetic moments on the U1 and U2 sites, they also reveal a positive magnetic moment on both of them, in disagreement with the DFT calculations (see Table 7.4).

The refined model for fitting of flipping ratios gives a rather large $C_2 \sim 2.5$ parameter, irrespective of the applied magnetic field, for the U2 site. It is much higher than the theoretical values calculated within the intermediate coupling scheme for the free U^{3+} (1.64) and U^{4+} (1.43) ions. These correspond to a ratio $\frac{\mu_L}{\mu_S}$ of -2.55 and -3.34 for U^{3+} and U^{4+}, respectively [130]. The U2 site exhibits $\frac{\mu_L}{\mu_S} \sim -1.7$ independent of the applied field. This ratio depends very strongly on the degree of hybridization between the uranium $5f$- and transition-metal d−wavefunctions and its decrease from the free ion values means strengthening of the hybridization [131]. In that sense the $5f$-wavefunction of the U2 ion strongly hybridizes with the surrounding Ru $4d$-wavefunctions as expected from its coordination. Similar values of the C_2 parameter can be found in the case of antiferromagnetic compounds $\mathbf{UNiGa_5}$ [132]

(2.45(7)) and UGa_3[133] (2.52(5)).

The total U1 magnetic moment, obtained from polarized neutrons is opposite to the DFT prediction. It also has an extremely small orbital moment irrespective of the applied magnetic field. This means an almost quenched orbital moment of the U ion on the U1 position, which is quite surprising and unexpected. Similar effects was already observed only in the case of metallic α-Uranium, for which the measured magnetic form factor can be approximated as spin-only and varies significantly from the one usually observed for the uranium-based compounds[134]. A later theoretical study actually describes α-Uranium as a system where the third Hund's rule is not valid and the orbital moment can be parallel to the spin moment[135,136].

The DFT calculations of $U_4Ru_7Ge_6$ also predict non-negligible induced moments on both the Ru sites. They are expected to be antiparallel to each other with dominating spin components. A small magnetic moment is also predicted to be present on the Ge site. In disagreement with the DFT calculations only negligible magnetic moment was found on the Ru1 site. On the other hand, the Ru2 site exhibits a significant induced moment dominated by its spin component. These Ru2 ions form a hexagonal arrangement around the U1 site and a distorted hexagon around the U2 position. The ratio of the magnetic moment on the Ru2 site and the U2 site is ≈ 0.12 both at $1\,\mathrm{T}$ and $9\,\mathrm{T}$ and ≈ 0.16 for the U1 site. This is another direct evidence for the hybridization between U $5f$ and Ru $4d$ wavefunctions. This resembles the case of URuAl, where the ratio of the Ru induced magnetic moment to the U moment is even bigger, 0.45(8)[137]. Parallel alignment of the magnetic moment on the U2 and the Ru2 sites can be understood by analogy with the mechanism proposed by Brooks *et al.*[138]. This was used to describe the parallel orientation of the moment on the U and the Co sites in UCoGe observed by XMCD[139], although polarized neutron diffraction showed an antiparallel arrangement[140]. According to that we would expect our $4d$ spins of Ru to be antiferromagnetically coupled to the $6d$ spins of U. Thanks to a positive intraatomic Hund's rule exchange these U $6d$ spin moments are coupled parallel to the $5f$ spin moments. Antiferromagnetic coupling of spin and orbital component on U then result in a final parallel orientation of the Ru and U moments.

The GGA DFT magnetic moments are only in semiquantitative agreement with the experimental results obtained by the MAXENT method and dipolar approximation including the fitting of form factors. One should take into account that the GGA results were obtained at zero magnetic field whereas the magnetic fields of $1\,\mathrm{T}$ and $9\,\mathrm{T}$ were applied in experiment. Therefore, the GGA calculations can be taken as the first approximation to the complex ferromagnetic ground state of $U_4Ru_7Ge_6$ compound. For instance the difference in the charge state of U1 and U2 atoms is only 0.002 electrons in GGA calculations. The difference in the charge state and the degree of the $5f$(U) and $4d$(Ru) hybridization between the U1 and U2 split states can be only roughly obtained using DFT GGA calculations. This points to future use of more a complex theory like for example Dynamical Mean-Field Theory (see for instance Ref.[141]) which is able to take into account the magnetic fluctuations at the U1 and U2 site.

The residual moment in the unit cell μ_{res} is estimated to represent $\sim 17\%$ of

the bulk moment. A comparably large and positive (12%) value was observed in antiferromagnetic UPd_2Al_3 where it was attributed to the possible contribution of the outer Pd electrons, as there is no observed induced moment on the Pd site itself [124]. This compound has a similar coordination of U ions surrounded by hexagons of $4d$ ions as $U_4Ru_7Ge_6$ but at a larger distance of 3.12 Å. An even larger moment of μ_{res} was found in the uranium-based superconductor UCoGe, where it reaches $54-85\%$ of the bulk magnetic moment [140], depending on the used method.

The fact that the different magnetic moments were observed on U1 and U2 even in the paramagnetic state at 20 K in a 9 T applied field clearly shows that the proposed distortion to the rhombohedral structure with two different U sites can also be induced by an external magnetic field even above the ordering temperature. The $\frac{\mu_L}{\mu_S}$ ratio remains unchanged relative to the ordered state, showing that there is no change in the nature of the $5f$ wavefunctions between the ferromagnetic and paramagnetic state. Similar results were found in the case of ferromagnetic superconductor UGe_2 [142].

It has to be noticed, that only a co-linear (z component) alignment of the magnetic moments was assumed in this study. If the $R\bar{3}m$ space group is taken as the real ground state structure and U1, U2, Ru1 and Ru2 are assumed as the only positions with magnetic moments, then there are four possible maximal magnetic space groups for the propagation vector $(0,0,0)$ (i.e. a ferromagnetic state). Among these $R\bar{3}m'$ is the only one that allows moment on all these four positions [119]. In the most general case it allows magnetic component out of the z-direction on the U2 and Ru2 position.

Only very few uranium based systems with two different U sites have been studied by neutrons. A ferrimagnetic ground-state was confirmed for the above mentioned UCu_5Sn [129]. Burlet *et al.* [143] describes antiferromagnetic order of the $U_4Cu_4P_7$ with two different U sites as a result of their different valence states. It is not possible to make any conclusions regarding the valence of U ions in the case of $U_4Ru_7Ge_6$, since the U^{3+} and U^{4+} form factors are very similar and it is also expected rather itinerant nature of the ferromagnetism. Nevertheless, $U_4Ru_7Ge_6$ is so far the only uranium based ferromagnet that shows a structural distortion in the ordered state, connected with the appearance of two different, formerly symmetry equivalent, U sites.

From the point of view of correct determination of form factors of dramatically reduced $5f$-electron magnetic moments and their orbital and spin components by neutron diffraction $U_4Ru_7Ge_6$ represents an extremely difficult case for several reasons, mainly: i) two inequivalent U sites/magnetic moments, ii) lack of reflections arising from only one of U sites, iii) non-negligible Ru $4d$-electron induced moments. Microscopic site-selective experiments are strongly desired for further progress in understanding the physics of this unique U intermetallic compound. Considering the strongly reduced U magnetic moment. Valuable information may be expected from a complex μSR study including determination of the possible muon stopping site(s).

8 Complex magnetism in UAu_2Si_2 revealed on single crystals

8.1 Introduction

The anharmonic lattice vibrations due to the asymmetric bonding potential lead to increasing equilibrium interatomic distances with rising temperature in solids. The corresponding thermal expansion is a monotonously increasing function of temperature. The anisotropy of bonding within the crystal lattice causes the anisotropy of thermal expansion which is manifested by different temperature dependences of the linear thermal expansion $(\Delta l/l)_i$ along the different crystallographic axes, i. The thermal expansion of metals includes also a conduction-electron contribution. This plays a considerable role at low temperatures where the phonon term almost vanishes.

The magneto-structural coupling, reflecting the interplay between the spin and lattice degrees of freedom, brings additional contributions to the thermal expansion in magnetic compounds. The magnetocrystalline anisotropy leads to anisotropic magnetic contributions to the thermal expansion. Magnetic materials then exhibit unusual thermal-expansion behavior especially in a magnetically ordered state.

The thermal expansion, similar to the specific heat, is thus a useful probe for investigations of thermodynamic phenomena in magnetic materials (without applying magnetic field). The specific heat has only bulk character, whereas the thermal expansion enables us to study also the anisotropy of thermodynamic properties.

The spatially extended uranium $5f$-electron wave functions in solids considerably interact with the overlapping $5f$ orbitals of the nearest-neighbor U ions and the $5f$-electron states hybridize with valence-electron states of non-uranium ligands ($5f$-ligand hybridization [17]) and the $5f$ electrons even participate in bonding [12,97]. The exchange interactions that are coupling the uranium $5f$-electron magnetic moments in U antiferromagnets are strongly anisotropic. The direct exchange interactions are due to the $5f$-$5f$ orbitals overlap. The anisotropy of these, typically ferromagnetic (FM), interactions and as well as the magnetocrystalline anisotropy are determined by the arrangement of the nearest-neighbor U ions in the lattice. The antiferromagnetic (AFM) interactions in U compounds are usually mediated by the anisotropic $5f$-ligand hybridization. The magnetoelastic coupling then produces highly anisotropic magnetic contributions to the thermal expansion and magnetostriction, especially in U antiferromagnets.

The anisotropy of magnetoelastic phenomena is a subject of numerous papers on U-based magnetic compounds. Most frequently they have been dedicated to the intriguing properties of URu_2Si_2, the most thoroughly studied uranium compound in the last three decades. The volume of this compound reduces considerably below the hidden-order transition temperature T_{HO} as manifested by a sharp positive peak in the thermal-expansion coefficient at T_{HO}. The volume reduction of the tetragonal structure is due to the basal-plane shrinkage. The simultaneous lattice expansion along the c axis is too small to compensate the negative basal-plane effect [144–147]. The possibility of a slight orthorhombic distortion of the tetragonal lattice at temperatures below T_{HO} plays an important role in the physics of URu_2Si_2.

The influence of anisotropic exchange interactions on the anisotropy of thermal expansion in U antiferromagnets is manifested by the magnetoelastic behavior of two other UT_2X_2 (T – transition metal, X – p-electron metal) compounds with the tetragonal $ThCr_2Si_2$ structure, UCo_2Si_2[148,149] and UNi_2Si_2[150] and several antiferromagnets from the family of hexagonal UTX compounds crystallizing in the ZrNiAl structure. In both structures the nearest U-U neighbors are located in the basal plane where the U magnetic moments are coupled ferromagnetically. All these compounds exhibit the strong uniaxial anisotropy fixing the U moments to the c axis, which is the easy magnetization direction. The AFM structures in these materials are built of the FM basal-plane layers antiferromagnetically coupled along the c axis. The thermal expansion below the Néel temperature (T_N) in these antiferromagnets (similar to URu_2Si_2 below T_{HO}) is strongly anisotropic as well as the magnetostriction accompanying field-induced metamagnetic transitions from the AFM to paramagnetic state. The corresponding a- and c-axis linear thermal expansions $(\Delta l/l)_a$ and $(\Delta l/l)_c$, respectively have in all cases opposite signs. The volume thermal expansion calculated according to Equation (3.14) for the UT_2X_2 compounds is small as a result of compensation of the opposite-sign linear expansions. The linear magnetostrictions λ_a and λ_c accompanying a metamagnetic transition are also of opposite signs leading to small volume magnetostriction. However, they have opposite polarities with respect to the corresponding-direction of thermal expansions. In fact, the magnetic contributions to thermal expansion of an antiferromagnet below T_N are suppressed by the opposite polarity corresponding to magnetostrictions caused by the metamagnetic transition.

UAu_2Si_2 belongs to the family of UT_2Si_2 compounds which adopt the tetragonal $ThCr_2Si_2$ structure (see Figure 8.1) (UIr_2Si_2 and UPt_2Si_2 crystallize in the $CaBe_2Ge_2$ structure[22]). These compounds exhibit a spectrum of physical properties ranging from Pauli paramagnets (UFe_2Si_2[151], URe_2Si_2 and UOs_2Si_2[47]) to magnetically ordered systems which are mostly complex and either AFM (UCr_2Si_2[152], UCo_2Si_2[153], UNi_2Si_2[154], URh_2Si_2[155], UPd_2Si_2[155,156], UIr_2Si_2[47,157], and UPt_2Si_2[47]), or FM (UMn_2Si_2[151]). UCu_2Si_2[153,158–160] exhibits a FM ground state with an additional AFM phase at higher temperatures. An exceptional case among them is the well-known URu_2Si_2[161] exhibiting the hidden-order transition. The magnetism of UAu_2Si_2 was for many years left unclear mainly due to metallurgical difficulties [22].

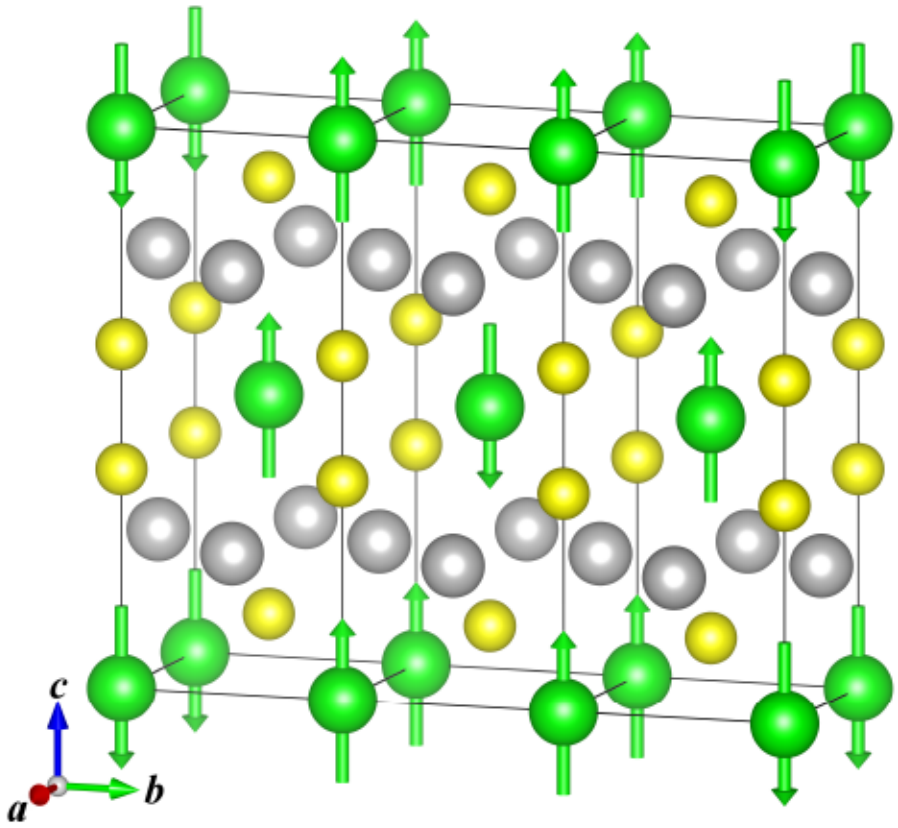

Figure 8.1: Structure of UAu_2Si_2. U ions are green, Au gray and Si are yellow. The arrows show the magnetic structure according to the Ref. [52]

Quite recently a single crystal of UAu_2Si_2 was prepared for the first time and systematic investigations of its intrinsic properties were commenced. The results obtained by measurements of magnetization, specific heat and electrical resistivity [39] followed by neutron diffraction [52] and ^{29}Si-NMR [162] experiments corroborate the conclusion about the ground state of UAu_2Si_2 as an uncompensated antiferromagnet, contrary to previous reports on polycrystals [47–51]. UAu_2Si_2 undergoes a FM-like transition at 50 K (referred to as T_2) followed by another magnetic phase transition (T_m) around 20 K. All the previous measurements show a large magnetocrystalline anisotropy with the direction of magnetic moments along the c axis. The propagation vector is $(2/3, 0, 0)$ and the magnetic structure can be described as a stacking sequence (+ + -) of the FM ac plane sheets along the a axis [52]. The specific-heat measurements point to an enhanced value of the Sommerfeld coefficient $\gamma \sim 180\,\mathrm{mJ \cdot K^{-2} \cdot mol^{-1}}$. Now, the UAu_2Si_2 single crystal is investigated by use of thermal-expansion, magnetostriction and magnetization measurements up to high magnetic fields and under hydrostatic pressure. The results of this chapter, are complementary to the previous neutron-diffraction work, confirming the uncompensated antiferromagnetic (UAFM) ground state of the compound [52], and bring evidence for the intrinsic nature of the FM component below ~ 50 K previously reported as parasitic in the first single-crystal study [39]. Magnetization measurements in pulsed high

magnetic fields helped to complete the phase diagram of UAu_2Si_2 and revealed signs of the presence of a tricritical point (TCP). These were performed by the Tatsuya Yanagisawa and are used in the thesis with his kind permission.

8.2 Results

8.2.1 Non-monotonous field dependence of T_m revealed by heat capacity measurement

Prominent lambda-shaped anomaly in the heat capacity data marks the second-order phase transition at $T_m \approx 20.5\,\mathrm{K}$ (see Figure 8.2 (a)). This value is estimated as the temperature balancing the entropy at the transition. Applied magnetic field along the c axis initially increases the transition temperature up to $T_{m,max} \approx 20.9\,\mathrm{K}$ around $5\,\mathrm{T}$. Further increase of the magnetic field lowers the transition temperature (see the final phase diagram in Figure 8.13). Such non-monotonous trend of T_m is clearly visible in the field dependence of heat capacity measured at $20.8\,\mathrm{K}$ (i.e. slightly above T_m). Entering and leaving the ordered state is connected with the increased heat capacity at this temperature (see left inset in Figure 8.2 (a)). In contrast, no additional field-induced transition was observed on the $2\,\mathrm{K}$ scan up to $9\,\mathrm{T}$. Separated $5f$-electrons contribution was obtained after subtracting the heat capacity of the polycrystalline $ThAu_2Si_2$ (data taken from Ref.[39]) and is plotted in Figure 8.2 (b). The Sommerfeld coefficient $\gamma \approx 193\,\mathrm{mJ \cdot mol \cdot K^{-2}}$ was determined from a standard $C_{p,mag}/T$ vs. T^2 plot and is lowered by applied external magnetic field (see the left inset in Figure 8.2 (b)). It suggests, that the effective mass is reduced with the magnetic field applied along the c axis. Values of the magnetic entropy S_{mag} (obtained as $C_{p,mag}/T$ integrated from $2\,\mathrm{K}$ up to T_m) reaches the value of $\approx 1.09\mathrm{R}\ln 2$ at $0\,\mathrm{T}$.

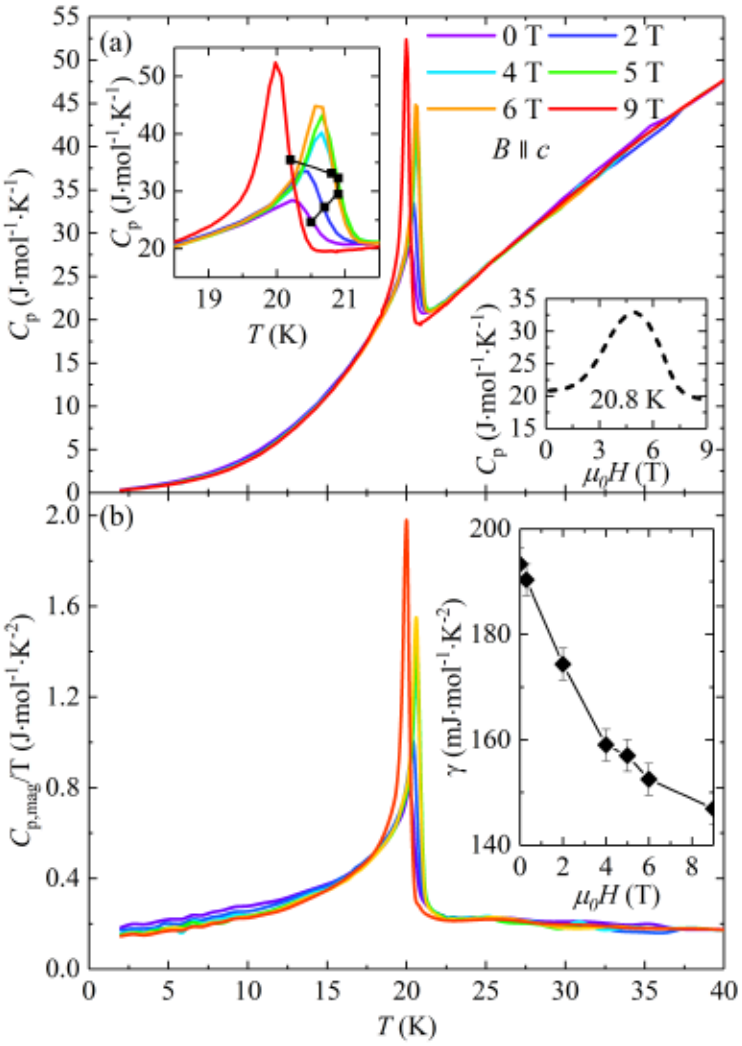

Figure 8.2: (a) Heat capacity of UAu_2Si_2 with the magnetic field applied along the c axis. The left inset shows region around T_m that is marked as black square for each data set. The right inset shows field dependence of heat capacity at 20.8 K. (b) Electronic contribution to the heat capacity divided by temperature. The inset shows field dependence of the Sommerfeld γ coefficient.

8.2.2 Anisotropic magnetic and magnetoelastic phenomena

The a- and c-axis linear thermal expansions together with the volume expansion calculated according to Equation (3.14) are plotted in Figure 8.3. The individual data are vertically shifted to set them equal to 0 at $T_m \approx 20.1$ K (slightly lower than from the heat capacity data). Below this magnetic phase transition a significant change in the temperature dependence of the thermal expansion is observed in line with the previous reports[39,52].

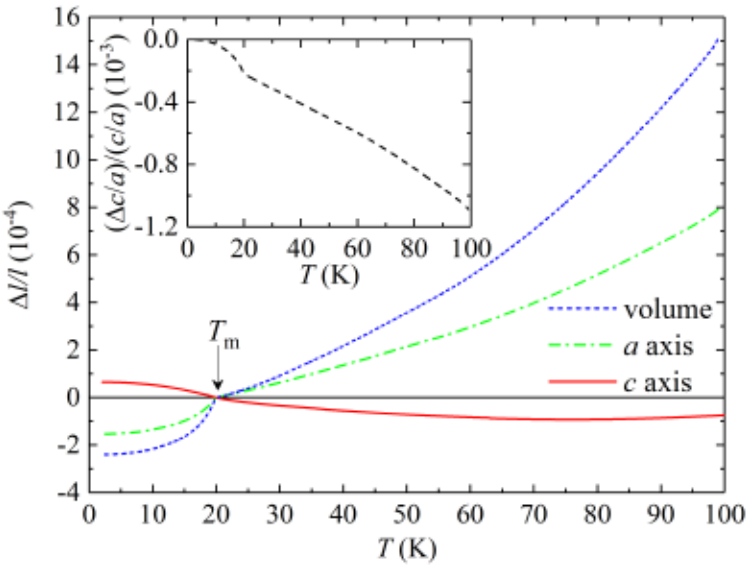

Figure 8.3: Linear thermal expansion for the a and c axis and volume change measured without applied external magnetic field. The inset shows c/a as a function of temperature. The curve is normalized to be equal to 0 at 2 K.

There is obviously a large anisotropy of the thermal expansion over the entire temperature range. The linear thermal expansion along the a axis shows a continuous decrease from 100 K down to the ordering temperature$T_m \approx 20.1$ K, where it bends down rapidly pointing at a large contraction of the unit cell along the a axis (-1.5×10^{-4} between T_m and 2 K). On the other hand, the thermal expansion along the c axis shows a broad minimum around 75 K followed by an increase at lower temperatures. The ordering temperature appears as an inflection point and the c-axis expansion below 20 K is 6.6×10^{-5}. The volume thermal expansion is calculated using Equation (3.14). The obtained relative volume change shows a large reduction below T_m(-2.3×10^{-4} between T_m and 2 K) as shown in Figure 8.3. The continuous character of the linear thermal expansion at T_m points to a second-order transition.

The linear thermal-expansion coefficients α_i are defined by Equation (3.9). The calculated linear thermal-expansion coefficients are plotted in Figure 8.4 together with the volume thermal-expansion coefficient defined by Equation (3.15). It is also useful to determine the temperature dependence of the c/a ratio. Therefore, the following temperature coefficient $\alpha_{c/a} = \alpha_c - \alpha_a$ is defined. Both quantities are plotted in Figure 8.4.

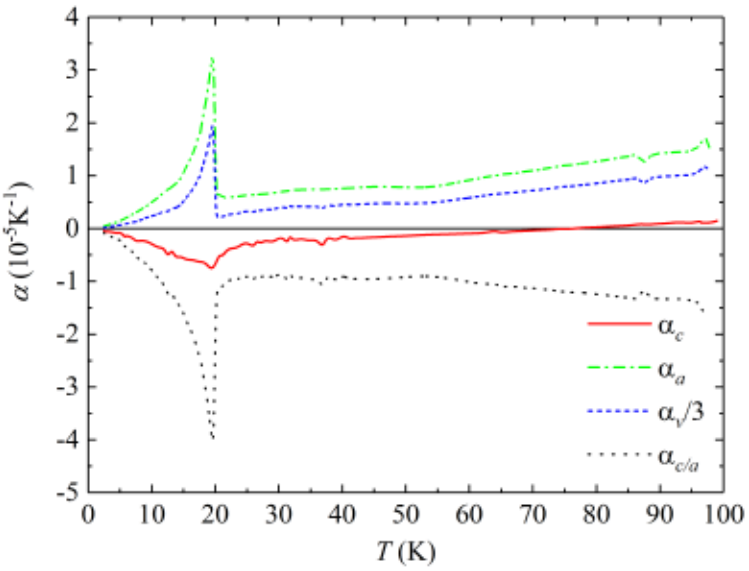

Figure 8.4: Linear thermal-expansion coefficients for the a and c axis together with the $\alpha_{c/a}$. Note that the volume dependence is plotted as $\alpha_v/3$.

The linear thermal-expansion coefficient for the c axis becomes negative below 75 K where the minimum of its relative length change occurs. There are sharp peaks at T_m for all measured curves and a small change of the slope above 50 K visible in α_a coefficient that is projected in the remaining computed quantities. Integration of the $\alpha_{c/a}$ coefficient along the whole temperature range results in the relative temperature dependence of the c/a ratio, see inset in Figure 8.3.

The temperature dependence of this ratio is monotonous and decreasing nearly linear above T_m. The slope increases below the T_m, emphasizing again the prominent contraction of the a axis.

As will be discussed below, ultra-pure samples of the isostructural compound URu_2Si_2 studied by synchrotron x-ray diffraction show a small orthorhombic distortion when entering the hidden-order state [163]. The size of the distortion and/or sample quality are possible reasons why it was not observed by the thermal-expansion measurements [144,164].

In order to test the presence of a lattice distortion in UAu_2Si_2 the thermal expansion also along the a axis and [110][5] direction was measured. The corresponding thermal expansions and the linear thermal-expansion coefficients are plotted in Figure 8.5.

[5]Miller indices notation is used for this direction for its self-explanatory meaning, while for simplicity a and c are used for the [100] and [001] directions, respectively throughout the whole chapter.

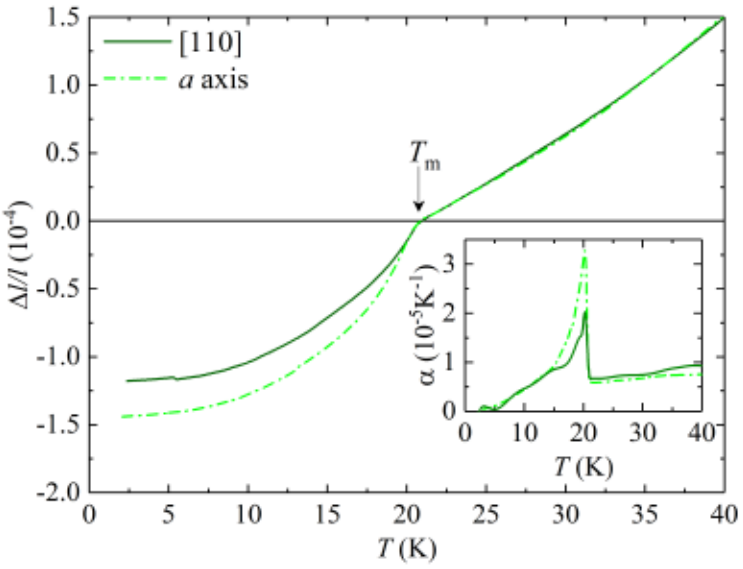

Figure 8.5: Linear thermal expansion in the tetragonal plane measured along the a axis and along the [110] direction. The inset shows the corresponding thermal-expansion coefficient for both directions.

An anisotropy of the thermal expansion is clearly observed in the basal plane. An undistorted tetragonal plane would show the same relative length changes for the a axis and for the [110] direction (face diagonal).

The thermodynamic relation for second-order phase transitions known as Ehrenfest relation can be used for estimation of the pressure dependence of the ordering temperature based on the jumps in the specific heat $\Delta(C_p/T)$ and the thermal-expansion coefficient $\Delta\alpha$ at T_m (see Equation (3.19)) with the known molar volume V_m for UAu_2Si_2 being $5.45 \times 10^{-5}\,m^3\,mol^{-1}$ using the unit-cell parameters from the neutron-diffraction work[52].

The jump in the specific heat of UAu_2Si_2 is $\Delta(C_p/T) = 554\,mJ \cdot mol^{-1} \cdot K^{-2}$. The jumps of the thermal-expansion coefficients at T_m and the corresponding hydrostatic-pressure and uniaxial-pressure derivatives of T_m predicted using Equation (3.19) are shown in Table 8.1.

Table 8.1: Jumps of the thermal-expansion coefficients $\Delta\alpha_i$ at T_m and the corresponding hydrostatic-pressure and uniaxial-pressure derivatives of T_m predicted using Ehrenfest relation.

	$\Delta\alpha_i\,(K^{-1})$	$\frac{dT_m}{dp}\,(K \cdot GPa^{-1})$
a	$2.69(8) \times 10^{-5}$	2.7(1)
c	$-4.4(1) \times 10^{-6}$	-0.44(1)
Volume	$4.9(1) \times 10^{-5}$	4.9(1)

The magnetization at various temperatures from 2 to 50 K was measured as

function of magnetic field up to 14 T applied along the c axis. The results are shown in Figure 8.6. This was followed by high-field measurements in pulsed magnetic fields up to ~ 58 T. The magnetization data up to 13 K show a low-field inflection point in the hysteretic part of the curve labeled as $\mu_0 H_1$. Another step-like feature is present at higher field and is labeled as $\mu_0 H_2$. Unlike the low-field transition, the $\mu_0 H_2$ anomaly can be traced to temperatures above T_m and is clearly distinguishable even at 40 K. The magnetization isotherms in the vicinity of T_m show another field-induced step-like transition at higher fields. Similar transitions were observed in the previous work on a different single crystal [39]. However, the anomalies labeled as $\mu_0 H_m$ were much less pronounced probably due to lower crystal quality. The values of characteristic fields at different temperatures have been determined using plots of $\mathrm{d}\mu/\mathrm{d}\mu_0 H$ vs. $\mu_0 H$ shown in Figure 8.7 for results at 2 and 19 K.

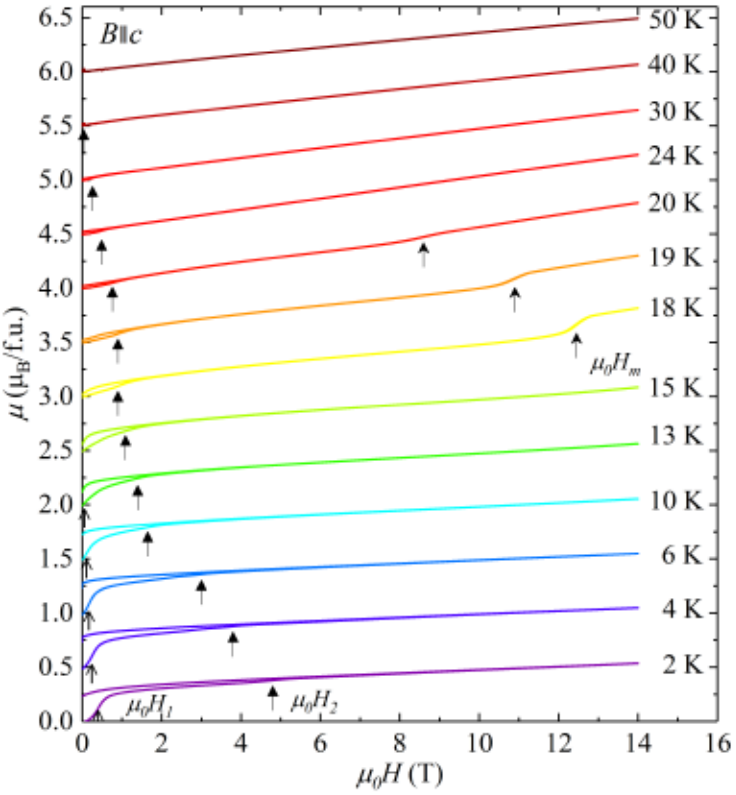

Figure 8.6: Magnetization curves measured with the field applied along the c axis up to 14 T. The curves are consecutively shifted by $0.5\,\mu_\mathrm{B}$/f.u. along the magnetization axis. The three types of arrows mark the $\mu_0 H_1$, $\mu_0 H_2$, and $\mu_0 H_m$, respectively.

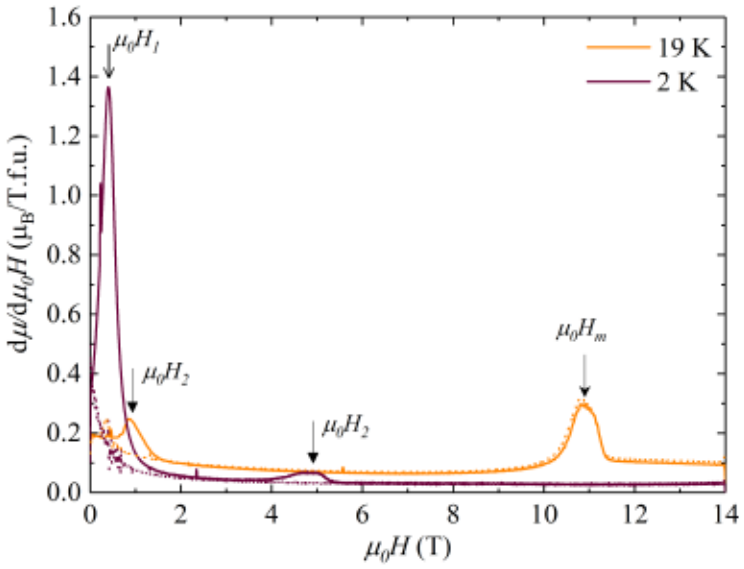

Figure 8.7: Field derivatives of the magnetization data at 2 and 19 K depicting the determination of $\mu_0 H_1$, $\mu_0 H_2$, and $\mu_0 H_m$. The solid lines correspond to field-up and dotted lines to field-down sweeps.

Further magnetization measurements in pulsed fields were performed to track the metamagnetic transition $\mu_0 H_m$. The measured magnetization was scaled using the static-field data obtained at 2 K and a small linear background was subtracted to give the correct absolute values. Results of the high-field measurement are plotted in Figure 8.8. A clear metamagnetic transition at $\mu_0 H_m$ is visible on all measured isotherms up to 20.1 K. The metamagnetic transition is most probably of spin-flip type[28] as one would expect for the system with large magnetocrystalline anisotropy. The low-temperature curves also show significant hystereses ($\Delta\mu_0 H_m$) between the up and down sweeps. The hysteresis narrows with increasing temperature and disappears around 16 K when $\mu_0 H_m \sim 16$ T. The temperature dependence of $\Delta\mu_0 H_m$ is shown in Figure 8.13(b).

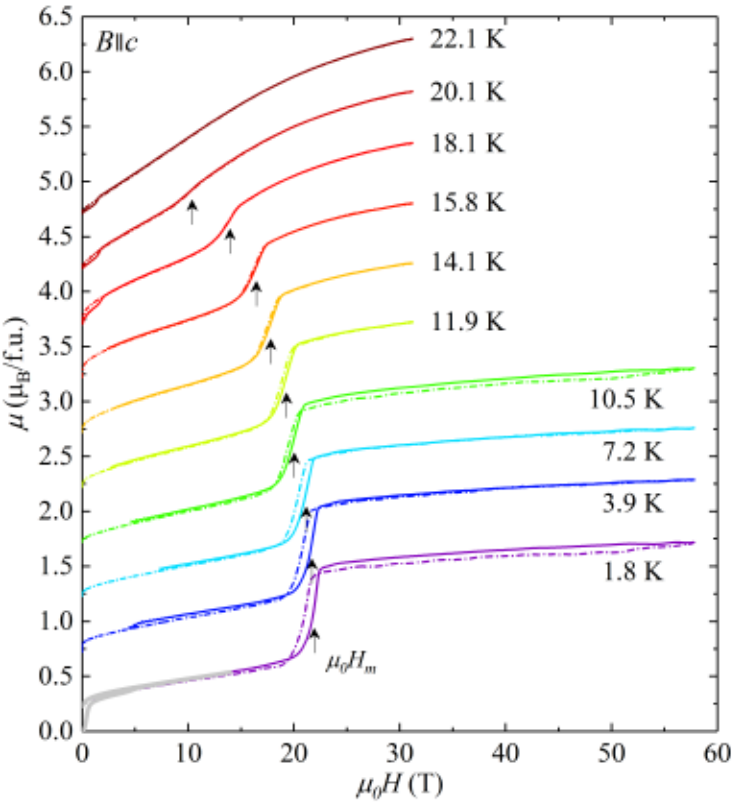

Figure 8.8: Magnetization measured in pulsed fields applied along the c axis up to $\approx 58\,\mathrm{T}$. The curves are consecutively vertically shifted by $0.5\,\mu_\mathrm{B}$/f.u.. The solid lines correspond to field-up and dash-dotted lines to field-down sweeps. The arrows mark the $\mu_0 H_\mathrm{m}$ transitions. The gray curve overlapping data at $1.8\,\mathrm{K}$ are the static-field data at $2\,\mathrm{K}$ up to $14\,\mathrm{T}$ shown in Figure 8.6.

The longitudinal magnetostriction was measured at various temperatures with magnetic fields up to $9\,\mathrm{T}$ applied along the tetragonal c axis, see Figure 8.9.

As in the magnetization data, anomalies at $\mu_0 H_1$ and $\mu_0 H_2$ can be clearly observed. Figure 8.10 shows how these fields were determined.

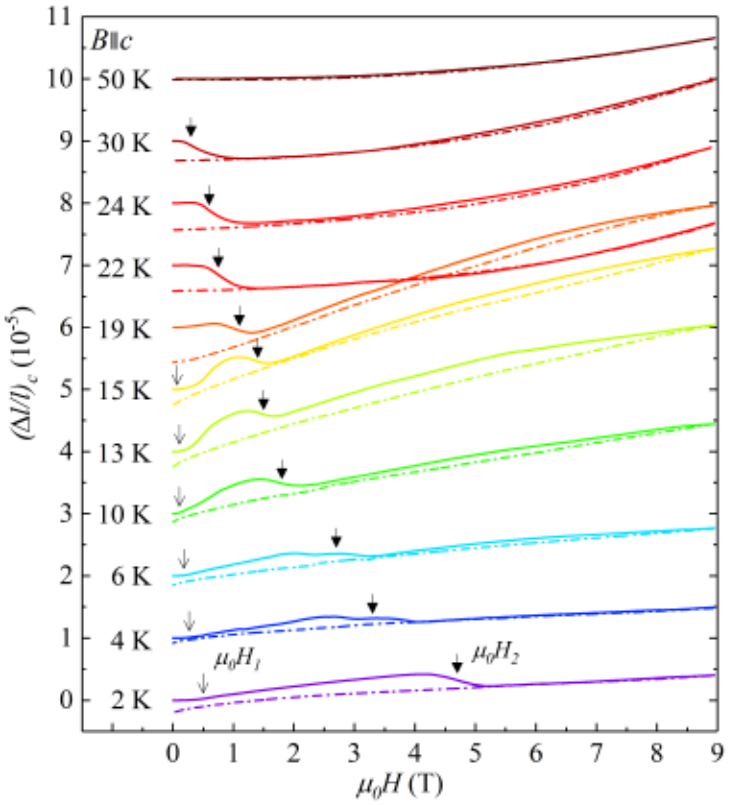

Figure 8.9: Longitudinal magnetostriction measured along the c axis. The solid lines correspond to field-up sweeps and dash-dotted lines to field-down sweeps. The curves are vertically shifted for better clarity.

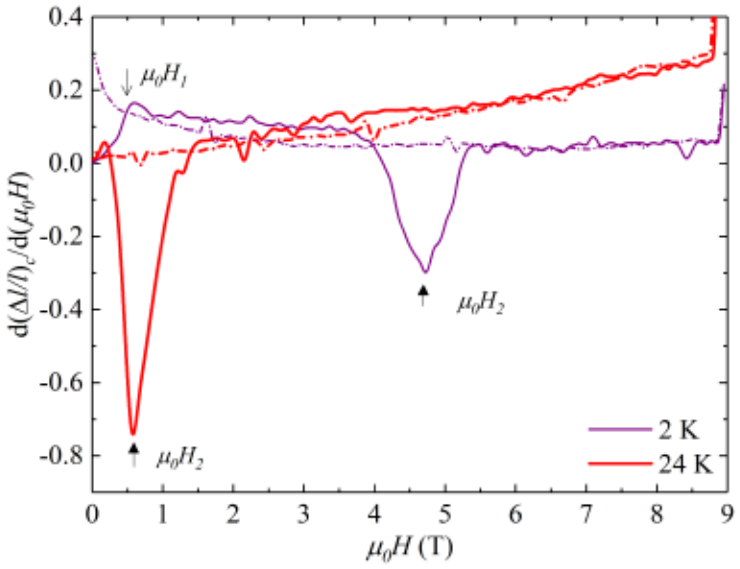

Figure 8.10: Field derivatives of the magnetostriction data at 2 and 24 K showing the determination of $\mu_0 H_1$ and $\mu_0 H_2$. The solid lines correspond to field-up scans and dash-dotted lines to field-down sweeps.

There is a significant change of the shape of the magnetostriction curves when UAu_2Si_2 crosses T_m, going from a concave to a convex curvature. Consequently further measurements of the longitudinal magnetostriction along the c axis up to 14 T at selected temperatures close to T_m were conducted. These isotherms show the high-field anomaly as a pronounced sharp drop at $\mu_0 H_m$ (see Figure 8.11), as determined from the magnetization measurements.

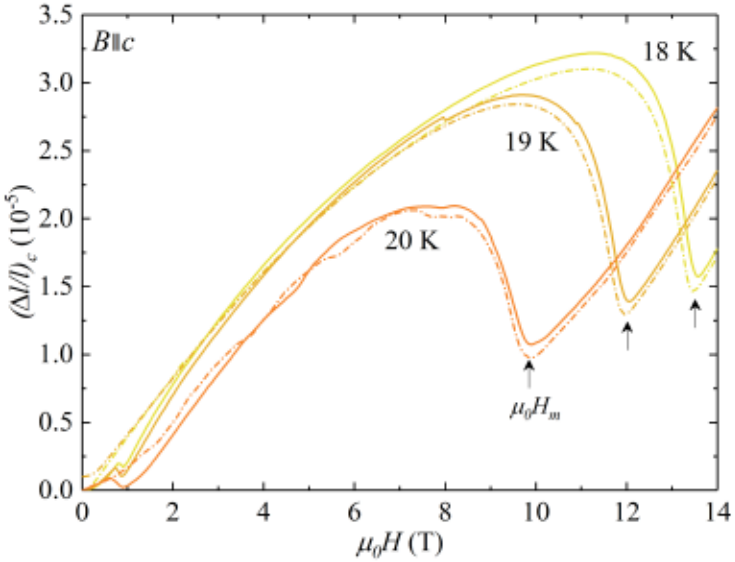

Figure 8.11: Longitudinal magnetostriction measured with the fields up to the 14 T applied along the c axis.

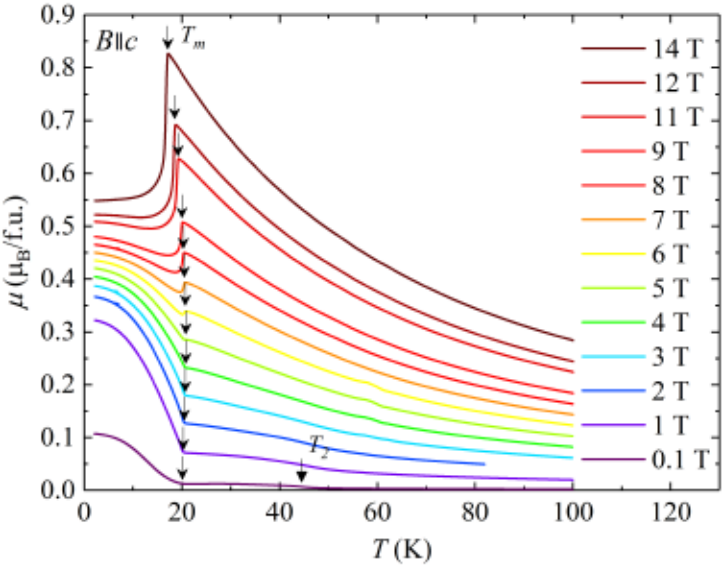

Figure 8.12: Temperature dependence of the magnetization along the c axis. The arrows mark the T_m and T_2 transitions.

The temperature dependence of the magnetization in various fields up to 14 T applied along the c axis were also measured. These data agree with the previous results obtained on a different single crystal [39]. The anomaly labeled as T_m, determined from the upturn of the magnetization for curves below 5 T and from the peak at higher fields, can be clearly seen. There is also another transition marked as T_2 that can be distinguished only in the low-field data at 0.1 T (see Figure 8.12).

The whole set of anomalies observed in the magnetization, magnetostriction and thermal-expansion measurements allows to construct the magnetic phase diagram as plotted in Figure 8.13(a). Figure 8.13(b) shows the temperature dependence of the hysteresis of the $\mu_0 H_m$ transition.

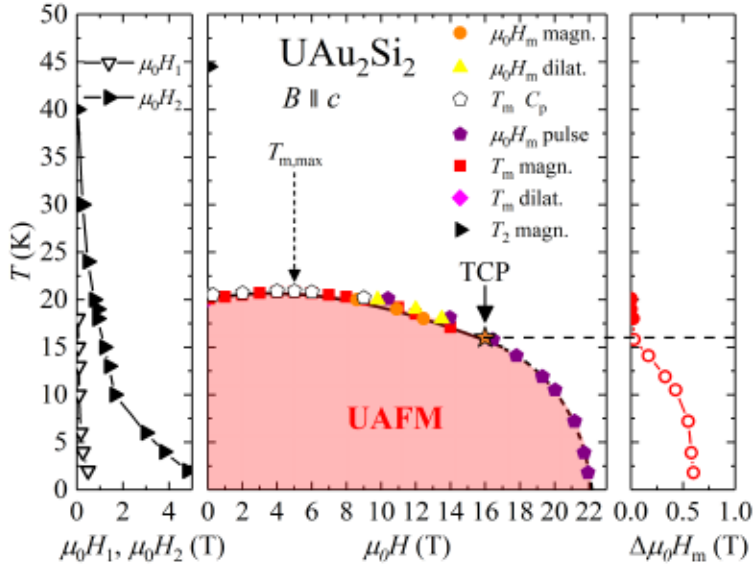

Figure 8.13: (middle panel) Magnetic phase diagram of UAu_2Si_2 constructed using the results of the specific-heat - C_p, magnetization and dilatometric (thermal expansion, magnetostriction) measurements. The star marks the tricritical point - TCP. (left panel) Temperature dependences of $\mu_0 H_1$, and $\mu_0 H_2$. (right panel) Temperature dependence of the hysteresis of the metamagnetic transition $\mu_0 H_m$ resulting from the pulsed-field measurements - open symbols and from the static-field measurements - full symbols.

8.2.3 Uranium spin density investigation by polarized neutrons

Further investigation of the phase diagram of UAu_2Si_2 (see Figure 8.13) was done using the neutron-diffraction techniques. As the previous neutron diffraction experiment was performed in zero magnetic field and revealed the ground state of the compound [52] the further polarized neutron diffraction experiment was performed on the D3 diffractometer at ILL, Grenoble using the wavelength of $\lambda = 0.85$ Å with the applied magnetic field along the c axis (magnetic easy axis). The main concept of the flipping ratios measurement using polarized neutron beam is the same as in the chapter 7.2.7 and further details of the technique are described in 6.2. As

the principle of the flipping ratio measurement of each (h, k, l) reflection requires the non-zero structure factor F_N it can be performed only on the (h, k, l) (h, k, l integer) reflections - i.e. not on the magnetic ones resulting from the non-integer propagation vector of the UAFM structure. Thus obtained information describes the ferromagnetic component and/or the field induced moment on the magnetic ion. The structural information for the refinement of the polarized neutron data were taken from the previous study on D10 diffractometer at ILL [52].

The external magnetic field was applied to be parallel with the magnetic easy axis c. Sets of the flipping ratios R were collected at four different conditions. The first condition was set to 2 K and 3 T after cooling at zero field. Internal agreement factor of the measured 50 inequivalent reflections was 1.28 %. The external magnetic field was consequently increased up to 9 T in order to reach the UAFM phase. Data set for this measurement counted 43 inequivalent reflections with the internal agreement factor of 1.06 %. Then the sample was warmed up above 60 K in order to be safely above the T_2 transition and consequently cooled down to reach this phase at 24 K and with the applied field of 0.3 T. Obtained 24 inequivalent reflections exhibited the internal agreement factor of 0.33 %. The last condition was in the paramagnetic phase at 24 K with the applied external field of 9 T.

Maximum entropy method (MAXENT)

The data were treated in the similar way as described in the chapter 7.2.7 and its principle is summarized in 6.2. Uniform distribution of the magnetic moment within the unit cell was used as an initial condition for all four measurement conditions. The results are plotted using the VESTA software[120]. Convenient tetragonal structure of UAu_2Si_2 (see Figure 8.1) allows to represent the spin-density distribution as a projection along the c axis to the basal $a - a$ plane. Spin-density maps for all measured conditions are summarized in Figure 8.14.

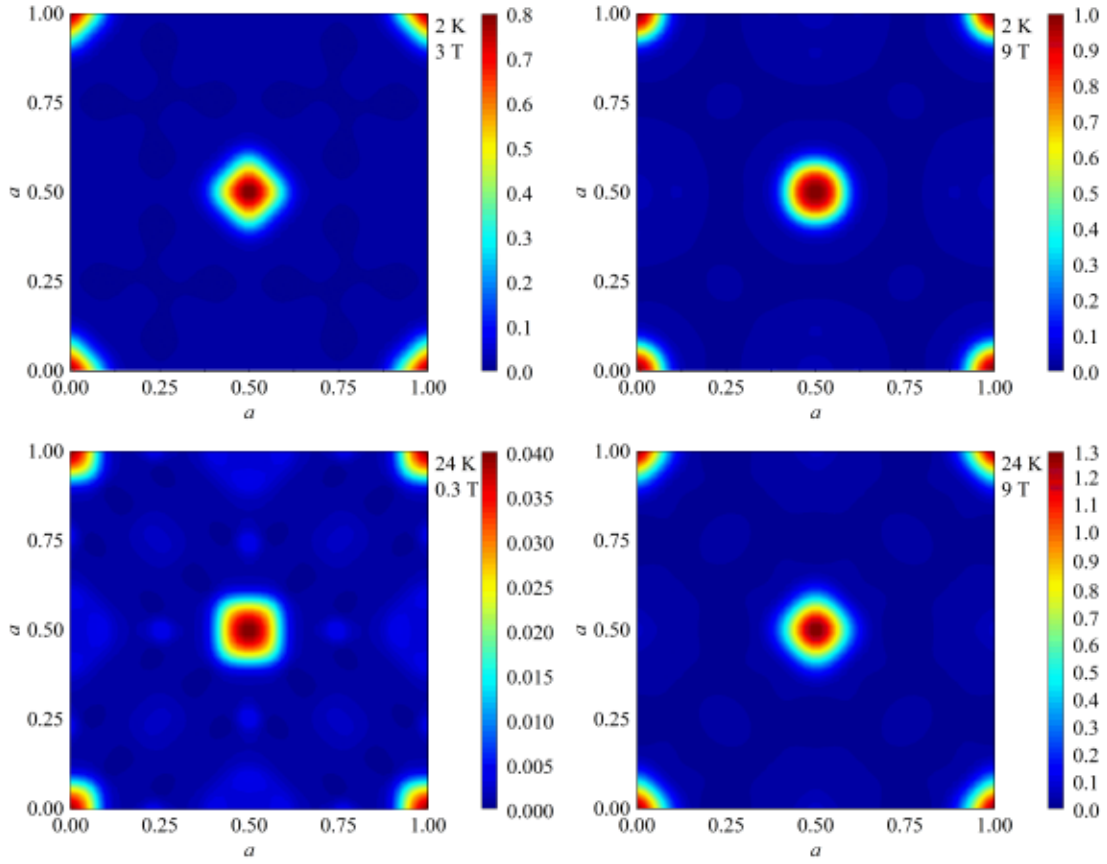

Figure 8.14: Spin-density map projections along the c axis for different conditions resulting from the MAXENT calculations. Unit of the density is $\mu_B \cdot Å^{-2}$ for all maps.

The main difference of the spin-density maps is a remarkable change of the local symmetry of the magnetic distribution around the U ion (center and corners of the projected unit cell). At 2 K and 3 T, the density has square-like shape with the corners pointing to the {100} directions. Increased magnetic field up to 9 T leads to the almost isotropic distribution around the U position. Qualitatively different distribution was observed at 24 K and 0.3 T, where the square-like density has corners pointing to the {110} directions. Calculated spin-density maps for the paramagnetic range at 24 K and 9 T strongly resembles the 2 K, 3 T conditions.

Magnetic moments for each condition obtained from the spherical integration of the density values around the U site are summarized in Table 8.2. The obtained magnetic moments μ showed saturation around ~ 1.2 Å. This value was chosen as the limit for integration r_{max}. The integrated magnetic moments as a function of the radius are plotted in Figure 8.15.

Direct refinement of the flipping ratios

Initial study using the maximum entropy method revealed the anisotropic distribution of the spin-densities. However, the dipolar approximation still can be used as a

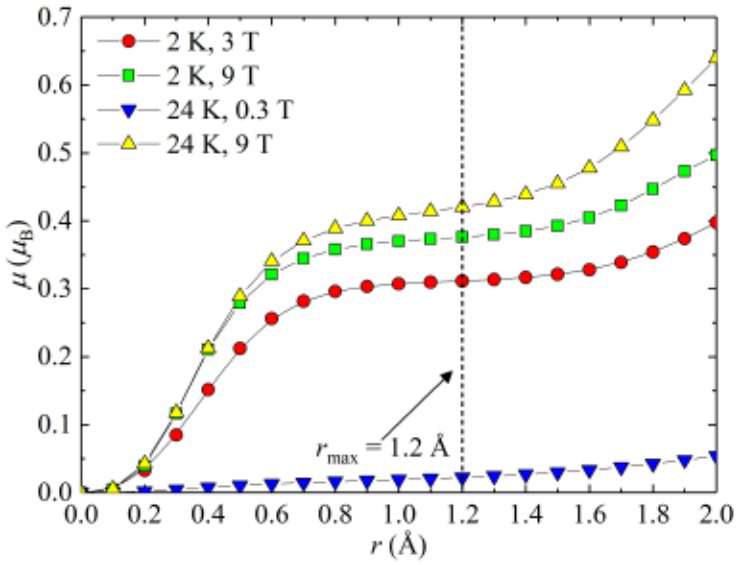

Figure 8.15: Integrated magnetic moment μ from the MAXENT spin density maps as a function of the sphere radius r up to the limit r_{max}.

useful tool for separation of the spin μ_S and orbital μ_L component of the magnetic moment, as was described in Section 7.2.7. The least squares refinement of the model was performed using the FullProf/WinPlotr [41,42] software. The magnetic form factor for the model is characterized by Equation (6.21) using the tabulated values of $\langle j_0(\boldsymbol{r})\rangle$ and $\langle j_2(\boldsymbol{r})\rangle$ corresponding to the uranium U^{3+} or U^{4+} [122]. Resulting fits were very similar using U^{3+} and U^{4+} form factor, as they have comparable shape. Presented following results are thus assuming U^{3+}. The measured and calculated flipping ratios for all conditions are compared in Figure 8.16. Values of the spin and orbital contribution for each condition are summarized in Table 8.2.

Table 8.2: Magnetic moments obtained by MAXENT and from the direct fitting of the flipping ratios using dipolar approximation for four different conditions. All values are in the μ_B.

	MAXENT				Dipolar approximation			
	3 T 2 K	9 T 2 K	0.3 T 24 K	9 T 24 K	3 T 2 K $\chi^2 = 0.47$	9 T 2 K $\chi^2 = 0.308$	0.3 T 24 K $\chi^2 = 0.67$	9 T 24 K $\chi^2 = 1.05$
Atom	μ	μ	μ	μ	μ_S μ_L μ	μ_S μ_L μ	μ_S μ_L μ	μ_S μ_L μ
U	0.31(3)	0.38(3)	0.022(5)	0.42(3)	-0.30(4) 0.60(3) 0.31(3)	-0.52(2) 0.84(3) 0.32(3)	0.00(2) 0.03(1) 0.03(1)	-0.40(3) 0.82(2) 0.42(2)
μ_{bulk}	0.39(1)	0.48(1)	0.013(2)	0.48(1)	0.39(1)	0.48(1)	0.013(2)	0.48(1)
μ_{diff}	0.08(3)	0.10(3)	-0.009(5)	0.06(3)	0.08(3)	0.16(3)	-0.02(1)	0.06(2)

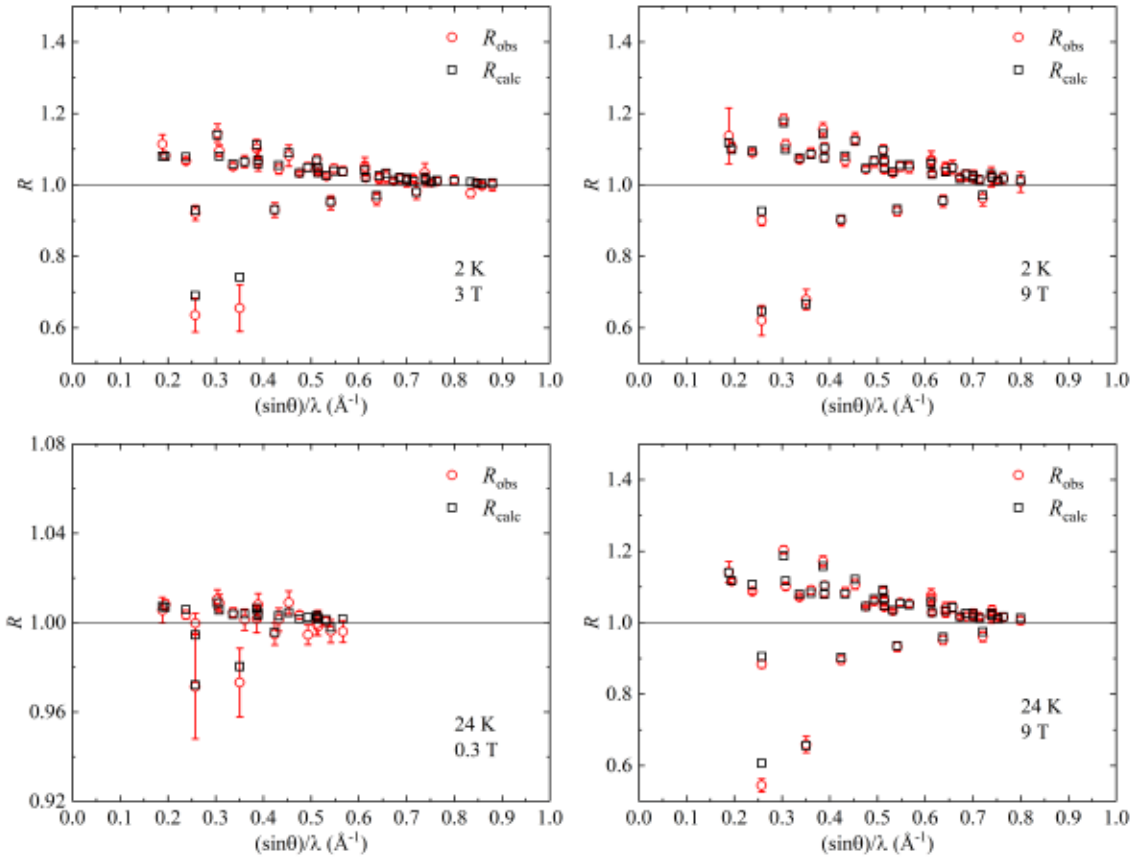

Figure 8.16: Flipping ratios measured at four different conditions compared with the calculated values using the dipolar approximation.

8.2.4 Neutron-diffraction of phase transitions in high magnetic fields

Additional detailed study of the magnetic structure at higher magnetic fields was performed at HFM-EXED diffractometer at BERII, Berlin. The static external magnetic field was again applied along the magnetic easy axis c, stabilized for every measurement point. Both absorption and extinction corrections together with the Vanadium calibration were applied. The limited cone of the magnet for the diffracted beam allowed only two structural reflections (-200) and (-110) (less visible on the reciprocal space maps) to be observed. List of observable magnetic reflections resulting from the previously determined propagation vector $\boldsymbol{k} = \left(\frac{2}{3}00\right)$ counted $\left(-\frac{2}{3}00\right)$, $\left(-\frac{4}{3}00\right)$, $\left(-1\frac{1}{3}0\right)$ and $\left(-1-\frac{1}{3}0\right)$. The map of the accessible reciprocal space is plotted in Figure 8.17. It also shows the difference between the ordered UAFM state (represented by the condition of 2 K and 3 T) and the state above the metamagnetic transition (2 K and 24 T). Absence of the magnetic reflections above the metamagnetic transition clearly demonstrates transformation to the high-field polarized paramagnetic regime (PPM).

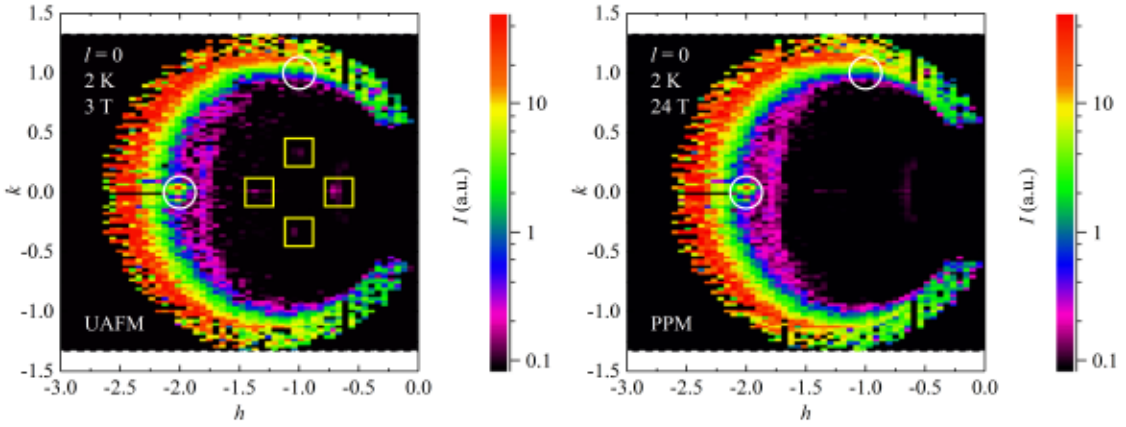

Figure 8.17: Reciprocal space maps $(h, k, 0)$ measured at 2 K at the UAFM state at 3 T (left) and at the high-field PPM regime at 24 T (right). Structural reflections are marked by white circles and magnetic reflections by yellow squares.

Set of measurements performed at 2 K with the varied field from 0 T up to 24 T and back to 0 T clarified constant propagation vector for these conditions. Field dependence after zero field cooling of the measured intensities of the magnetic and structural reflections is plotted in Figure 8.18 and 8.19, respectively.

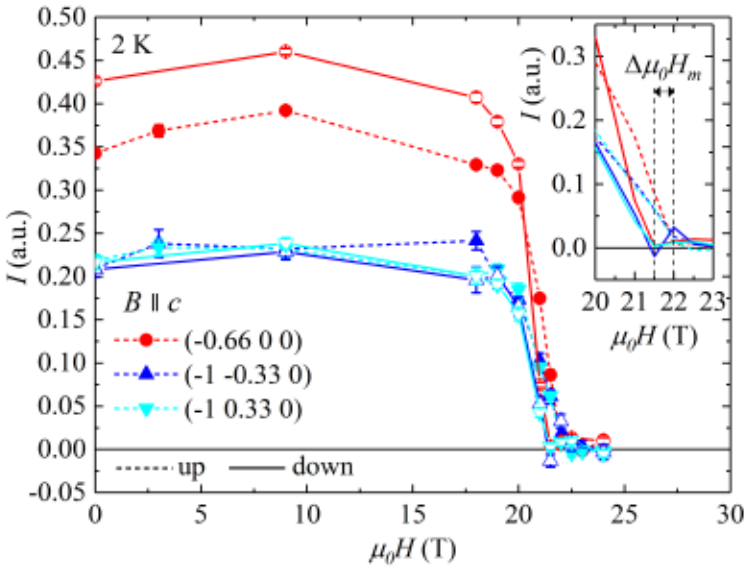

Figure 8.18: Field-up (dashed lines and full symbols) and field down (solid lines and open symbols) measurement (applied along the c axis) of the diffracted intensities for the set of magnetic reflections at 2 K. The inset shows the region around transition $\mu_0 H_m$ with the marked hysteresis $\Delta\mu_0 H_m$.

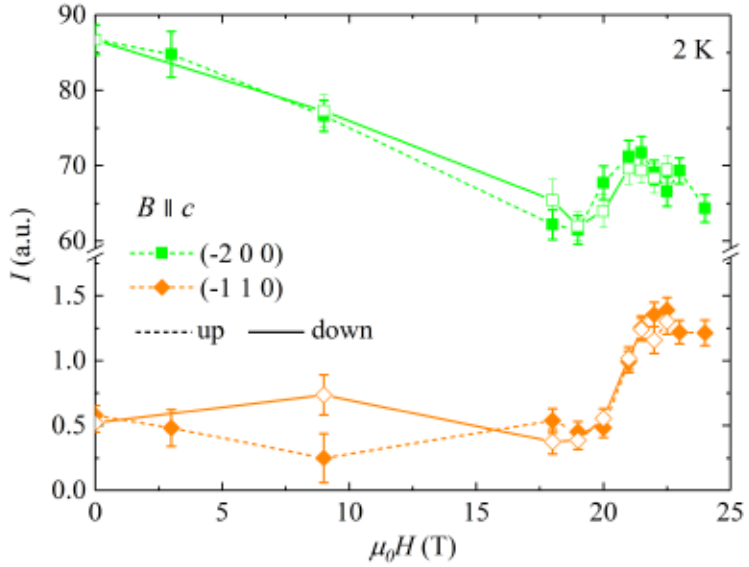

Figure 8.19: Field-up (dashed lines and full symbols) and field down (solid lines and open symbols) measurement (applied along the c axis) of the diffracted intensities for the set of structural reflections at 2 K.

Field-up measurement of the intensities of all magnetic reflections show initial increase followed by the sudden drop at the critical field around $\mu_0 H_m \approx 22$ T. The intensity of all the magnetic reflections is zero above this threshold, within the

measurement limits, in agreement with the high-field PPM phase. Consequent measurement with the step-like decreasing of the magnetic field revealed clear hysteresis as the intensity of the magnetic reflections starts to increase again around $21.5\,\mathrm{T}$ (see inset of Figure 8.18). Width of the hysteresis is $\Delta\mu_0 H_m \approx 0.5\,\mathrm{T}$ in agreement with the high-field magnetization measurements (see Figure 8.8 and 8.13). The structural reflection(-110) has rather constant field dependence within the the ordered state (see Figure 8.19). The high-field PPM regime is connected with the reduction of the magnetic unit cell to the same size as the structural one. It leads to the dramatic increase of the intensity of (-110) reflection that has a small nuclear structure factor. The field down sweep follows the dependence from the field up measurement with less pronounced hysteresis. More significant field dependence can be observed in the case of (-200) reflection. Its intensity is continuously decreasing towards the critical field above which it enhances as a sign of the reduced magnetic unit cell.

8.2.5 Hydrostatic-pressure effects

As the calculations using the Ehrenfest relation predict a rather dramatic positive effect of hydrostatic pressure on the ordering temperature ($\approx 4.9(1)\,\mathrm{K}\cdot\mathrm{GPa}^{-1}$) it was necessary to verify this hypothesis. For that purpose, the magnetization was measured in a field of $0.1\,\mathrm{T}$ applied along the c axis under hydrostatic pressures up to $\sim 1\,\mathrm{GPa}$ (see Figure 8.20). The measured data were corrected for the diamagnetic contribution of the pressure cell. The shape of the ambient pressure curve differs from those obtained under pressure. This can be an effect of a slightly different orientation of the sample in the pressure cell. Contrary to the prediction, only a small shift of the transition temperature T_m was observed with applied pressure (see inset of Figure 8.20). The transition temperature T_m is again defined by the upturn of the magnetization curve. The resulting small ratio of the pressure change of the ordering temperature is $\mathrm{d}T_\mathrm{m}/\mathrm{d}p \approx 0.6(1)\,\mathrm{K}\cdot\mathrm{GPa}^{-1}$. A larger effect is visible in the reduction of the spontaneous magnetic moment μ_spont with the slope $\mathrm{d}\mu_\mathrm{spont}/\mathrm{d}p \approx -0.019(6)\,\mu_\mathrm{B}/\,(\mathrm{f.u.}\cdot\mathrm{GPa})$.

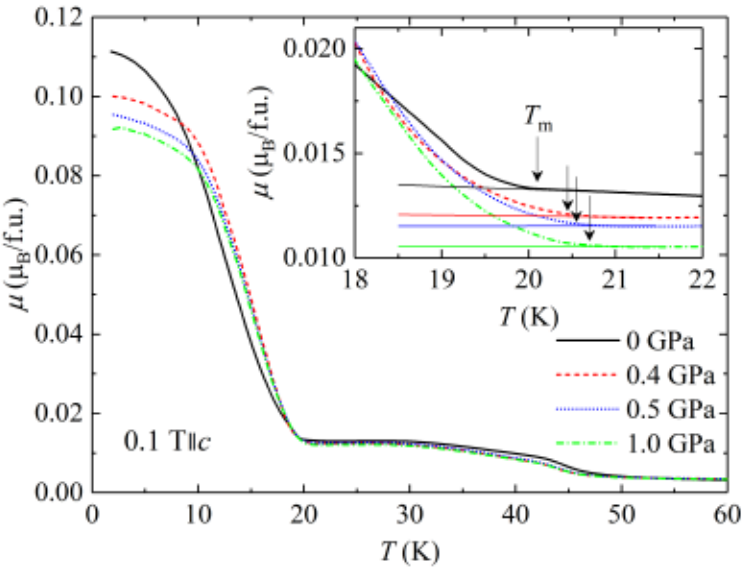

Figure 8.20: Magnetization in a magnetic field of 0.1 T applied along the c axis under various hydrostatic pressures up to 1.0 GPa. The inset shows the region near T_m marked by the arrows. The curves in the inset are vertically shifted for clarity.

The exact position of T_m is difficult to determine from the low-field magnetization curves and it is not visible in zero magnetic field. Thus, the thermal expansion was measured using strain gauges under hydrostatic pressure. This setup is enable to resolve length changes of the order of 10^{-6}. It is needed to measure a standard material (usually copper) at exactly the same conditions to obtain absolute values of the length change with varying temperature and pressure. Nevertheless, the correction function of the strain gauges is known to be smooth [165]. It is, thus, possible to track some large and well-defined features connected with phase transitions even without the proper calibration. The strain-gauge was glued to the sample to be sensitive for the length change along the a axis and the magnetic field was applied in the perpendicular direction along the c axis. The relative change of the strain gauge resistance measured at 1.65 GPa in various magnetic fields is plotted in Figure 8.21, together with a sketch of the geometry of the experiment. The large upturn at low temperatures is a consequence of the temperature dependence of the strain gauge itself[165].

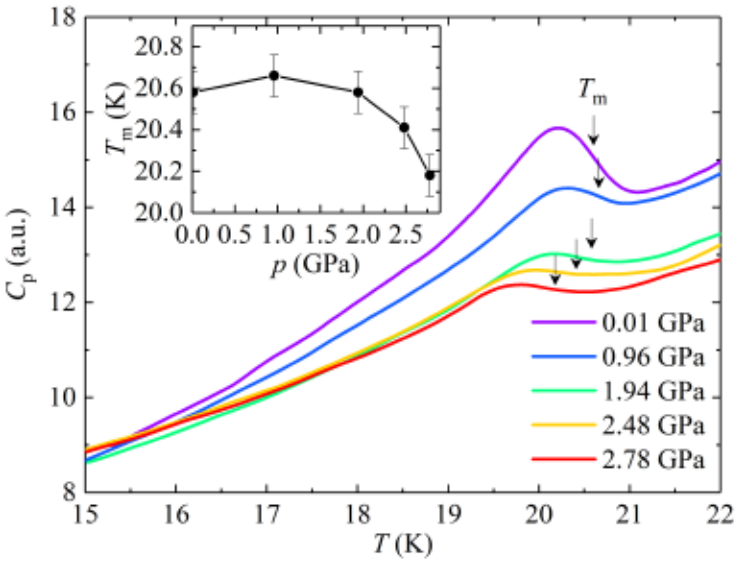

Figure 8.21: Relative change of the strain-gauge resistance active along the a axis measured under the hydrostatic pressure of 1.65 GPa and with various external magnetic fields up to 14 T applied along the c axis (with a step of 2 T). The curves are relative to the resistance value at 2 K and are vertically shifted for clarity. The drawing sketches the geometry of the experiment. The inset shows the field dependence of T_m at 1.65 GPa and ambient pressure. Latter data are taken from magnetization measurements.

The field dependence of T_m at 1.65 GPa is plotted in the inset of Figure 8.21. Compared to the data at the ambient pressure, there is an obvious increase of the ordering temperatures up to the highest magnetic field. At 0 T, $T_{m,1.65\,GPa} = 20.6\,K$ which gives a pressure change of the ordering temperature of $dT_m/dp \approx 0.36\,K \cdot GPa^{-1}$.

8.3 Discussion

The heat capacity of UAu_2Si_2 shows clear second order phase transition at $T_m \approx 20.5\,K$ (see Figure 8.2). Applied magnetic field along the c axis initially raises the transition temperature. It peaks around 5 T and is suppressed by higher fields. The observed magnetic entropy S_{mag} that is connected with the transition equals to $\approx 1.09R\ln 2$. The Sommerfeld coefficient is estimated as $\gamma \approx 193\,mJ \cdot mol^{-1} \cdot K^{-2}$ and decreases with the applied field in the similar way as for the high field phase of URu_2Si_2[166] pointing on the lowering of the effective electron mass.

The thermal-expansion measurements on a UAu_2Si_2 single crystal revealed a large anisotropy which is mainly due to magnetic contributions. The ordered state below T_m is connected with a dramatic lattice contraction in the basal plane (a axis). This together with the relatively small expansion of the c axis leads to the ground state volume collapse (Figure 8.3). This behavior strongly resembles the case of the isostructural heavy-fermion compound URu_2Si_2 entering the hidden-order

state at 17.5 K[144]. The linear thermal-expansion coefficient for the a axis consequently exhibits a sharp positive anomaly at the ordering temperature whereas the c-axis anomaly is negative and less pronounced (Figure 8.4). The volume thermal-expansion coefficient of URu_2Si_2 also exhibits a sharp and positive peak at 17.5 K that can be translated to a volume decrease in the ground state. A very similar behavior for both compounds can be found in the temperature dependence of the c/a ratio. Both materials show an upturn below the ordering temperature, accenting the contraction in the basal plane, and nearly linear temperature dependence at higher temperatures up to 40 K. Nevertheless, the c/a ratio of URu_2Si_2 has a pronounced minimum around 60 K, that is not visible for UAu_2Si_2 which shows a linear temperature dependence up to 100 K. Even though the overall character of the thermal expansion of URu_2Si_2 and UAu_2Si_2 is qualitatively similar, it does differ quantitatively. The step in the volume thermal-expansion coefficient $\alpha_v^* = (\alpha_a + \alpha_b + \alpha_c)/3$ is $\sim 2.5 \times 10^{-6}\,\mathrm{K}^{-1}$ for URu_2Si_2[144] and almost an order of magnitude larger ($\sim 1.6 \times 10^{-5}\,\mathrm{K}^{-1}$) for UAu_2Si_2. It is believed, that anomalies in the thermal-expansion coefficient of the order of 10^{-4}, 10^{-5} can be connected with a structural transitions[144] as in the case of UPd_3[167]. In that sense, URu_2Si_2 does not evidence a structural change in the hidden-order state. Nevertheless, there is a list of studies which suggest the breaking of the fourfold rotational symmetry of the tetragonal c axis[168–173], whereas the high-resolution x-ray backscattering[174] and thermal–expansion data[144,164] do not confirm this. However, lattice-symmetry breaking from the fourfold tetragonal to twofold orthorhombic structure was unambiguously observed by high-resolution synchrotron x-ray diffraction measurements in zero field[163]. The fact that this distortion is observed only in ultra-pure samples may explain the long list of more or less unsuccessful attempts to observe this.

As the thermal-expansion coefficients of UAu_2Si_2 are even one order of magnitude larger (i.e., $\sim 10^{-5}$) the possibility of some kind of lattice distortion should be seriously considered. The thermal-expansion measurements show an anisotropic expansion in the basal plane breaking the fourfold symmetry with respect to the c axis. The body-centered room-temperature tetragonal structure of UAu_2Si_2 belongs to the $I4/mmm$ space group. It has 15 maximal non-isomorphic subgroups and only two of them have no fourfold symmetry along the c axis. These are the orthorhombic $Fmmm$ and $Immm$ space groups. The same space groups were also considered in the synchrotron x-ray diffraction study of URu_2Si_2[163]. The $Fmmm$ space group was found to describe the system in the hidden-order state.

The measurement of thermal expansion, as a macroscopic quantity, is not sufficient to properly describe the space group of the distorted structure, even though it is more sensitive to detect distortions than diffraction studies. In that sense, high-resolution x-ray diffraction experiments are needed to resolve the structure of UAu_2Si_2 in the ordered state. The recent results from an ultrasonic study show a Curie-type softening in the transverse $(C_{11} - C_{12})/2$ mode toward T_m, that could also point to orthorhombic distortion at T_m[175]. In the analogy with the URu_2Si_2, there was also observed softening of the same mode suggesting that the Γ_{3g} (B_{1g}) -type lattice instability is innate in these systems[164,176].

The large ground-state volume collapse of UAu_2Si_2 indicates initial positive pres-

sure dependence of the ordering temperature of $dT_m/dp \approx 4.9(1)\,K \cdot GPa^{-1}$, according to the Ehrenfest relation. Uniaxial pressure applied along the a axis should have a positive effect as well ($\approx 2.7(1)\,K \cdot GPa^{-1}$). On the other hand, uniaxial pressure along the tetragonal c axis should lower T_m at a rate of $\approx -0.44(1)\,K \cdot GPa^{-1}$. These findings qualitatively agree with the experimentally confirmed behavior of URu_2Si_2 where the predicted pressure dependences are approximately eight times smaller. Ehrenfest-relation estimates give a pressure dependence of the hidden-order transition of $1.4\,K \cdot GPa^{-1}$(Ref.[144]) and high-pressure resistivity measurements show an experimental initial slope of $1.01\,K \cdot GPa^{-1}$ (Ref.[177]). The estimated pressure changes of the ordering temperature of the hidden order of URu_2Si_2 and the AFM state of UAu_2Si_2 are largely different. A similar dramatic change of the dT/dp values was observed for the $U(Ru,Fe)_2Si_2$ system, where doping of Fe leads to a change of the hidden order to "large-moment antiferromagnetism" [147]. However, our measurement of the magnetization under hydrostatic pressure up to $1.0\,GPa$ show only a weak pressure dependence of T_m (Figure 8.20). The estimated slope is $dT_m/dp \approx 0.6(1)\,K \cdot GPa^{-1}$. The lowering of the spontaneous magnetization with increasing pressure $d\mu_{spont}/dp \approx -0.019(6)\,\mu_B/(f.u. \cdot GPa)$ was also observed. The thermal-expansion measurement of the a axis under hydrostatic pressure up to $1.65\,GPa$ revealed a small increase of T_m at zero magnetic field to $T_{m,1.65\,GPa} = 20.6\,K$. Applying magnetic fields along the c axis results in a similar shape of the phase boundary as for the ambient-pressure state, but shifted to slightly higher temperatures. The obtained slope of the pressure dependence of the ordering temperature is $dT_m/dp \approx 0.36\,K \cdot GPa^{-1}$, even smaller than the value obtained from the magnetization measurements. The observed inconsistency with the expected trend from the Ehrenfest relation is rather unexpected. It may be caused by a structural distortion that takes place at T_m. In that case Equation (3.14) is not valid and the real volume change can be different, i.e., possibly smaller. Another question is the applicability of the Ehrenfest relation itself. Although it is widely and successfully used to characterize the pressure dependence (both positive and negative) of AFM [178,179] and FM[178,180,181] second-order phase transitions, it may strictly be applied only for the superconducting transitions[182]. And even for some superconductors the predicted pressure dependence determined by use of the Ehrenfest relation differs from the experimental findings, such as in the case of $PuCoGa_5$[183] by an order of magnitude or even by sign in the layered iron-based superconductors of the $Ba(Fe_{1-x}Co_x)_2As_2$ series[184]. Both of these systems exhibit very anisotropic thermal-expansion coefficients, similar as for UAu_2Si_2.

The magnetization isotherms (Figure 8.6 and 8.8) clearly and reproducibly show anomalies at $\mu_0 H_1$, $\mu_0 H_2$, and $\mu_0 H_m$ in line with the previous study on a different single crystal[39]. However, a much sharper character of the step-like transition at $\mu_0 H_m$ was found. It is suggested, that the deviation from the linear dependence of the magnetization, that was marked as $\mu_0 H_m$ in the Ref.[39] is a low-field sign of the step-like transition which takes place at higher fields. This transition was previously not observed, possibly due to a lower crystal quality or slightly improper orientation of the c axis with respect to the applied field.

The magnetostriction measurements (Figure 8.9 and 8.11) with field applied along

the c axis reproduce the transitions observed in the magnetization data. The transition at T_2 is reflected in the thermal-expansion data only by a small slope change in α_a, α_v and $\alpha_{c/a}$ around 50 K (Figure 8.4). The size of the relative length change of the c axis at the $\mu_0 H_2$ feature, is of the order of 10^{-6}. This provides an evidence of bulk character of this hysteresis, which can be traced up to $\sim$ 40 K as in the magnetization data.

A larger relative length contraction of the c axis ($\sim 10^{-5}$) takes place at $\mu_0 H_m$. It resembles the c-axis contraction at the field-induced phase transition of URu_2Si_2[185].

Lets now discuss the revised magnetic phase diagram of UAu_2Si_2 (Figure 8.13). The high-field magnetization measurements show that the temperature dependence of the hysteresis of the $\mu_0 H_m$ transition vanishes around 16 K (and 16 T) where the transition changes its character from step like to continuous. This is attributed to the change of the order of the phase transition from first order (in higher fields) to second order (in lower fields). Such a point is usually referred to as a tricritical point (TCP)[28]. This point is marked by a star in the phase diagram in Figure 8.13(a). Similar tricritical points have recently been reported in the uranium-based antiferromagnets UNiAl[186], USb_2[187], UN[188], $UIrSi_3$[189] and also for UIrGe[190] as will be closely described in the next part of this thesis. The critical field, where the transition temperature T_m is suppressed to 0 K in UAu_2Si_2 is extrapolated to be about 22 T.

The spin-density maps obtained from the polarized neutron diffraction in the applied magnetic field revealed dramatic changes of the symmetry of the magnetic moment distribution around the U position. Large difference is observed even within the UAFM phase between the 2 K, 3 T and 2 K, 9 T where the square-like shape of the projected distribution changes from the configuration with the corners pointing towards {100} directions to the distribution rotated by 45° with more isotropic-like shape. The later type of distribution, being even more square-shaped, with corners towards {110} directions was determined for the temperature 24 K and 0.3 T. This results must be taken with caution, as it has to be noticed that such condition, specially the low applied external field, means small induced magnetic moment and brings the used method of the flipping-ratios measurements to the vicinity of its experimental reliability. Nevertheless, the set of obtained flipping-ratios (different from unity) shows that the polarization of the incident beam persist even in such small applied external magnetic field. The high-field PPM regime, represented by 24 K and 9 T measurement, represent by its spacial distribution of the moment the 2 K, 3 T case. Very similar change of the spin-density distribution was observed in the sister URu_2Si_2 compound[191,192]. The field-induced PPM regime of URu_2Si_2 (25 K 9.6 T) is also characterized by square-like distribution of the magnetic moment with corners towards the {100} directions. On the other hand, the pattern obtained in the hidden-order state (rotated by 45° compared to the PPM case) is comparable with the UAFM (2 K, 9 T) state of UAu_2Si_2. This shape change of the magnetization distribution in URu_2Si_2 is explained as the fingerprint of the dotriacontapole (rank five multipole) order in this compound. Such multipolar order study of UAu_2Si_2 is desired as it could bring another evidence of the intimate connection of these compound as well as have direct impact on the study of its complex phase diagram.

The high-field neutron diffraction experiment confirmed the hysteresis of the metamagnetic transition form the UAFM phase towards the PPM regime at $\approx 22\,\mathrm{T}$ for $2\,\mathrm{K}$ (Figure 8.18). Increase of the intensities of the structural reflections above the metamagnetic transition points on the recovery of the magnetic unit cell to the size of the structural one (Figure 8.19).

9 Magnetic-field-induced phenomena in an antiferromagnet UIrGe

9.1 Introduction

The members of the family of UTX compounds (T = transition metal, X = p element) with orthorhombic structure show a variety of magnetic properties. Most of these compounds exhibit the TiNiSi-type structure[22]. This arrangement is the ordered type of the more complex $CeCu_2$-type structure where uranium atoms occupy the cerium positions. An important hallmark of this structure is the zig-zag chain of the uranium ions that stretches along the a axis (see Figure 9.1). This segment also exhibits the shortest inter-uranium distance d_{U-U}, and, as was mentioned in Section 2.2, the magnetic easy axis is expected to be perpendicular to this direction. Most of the orthorhombic UTX compounds thus have the magnetic easy axis along the c or b direction and the a direction is typically the magnetic hard axis.

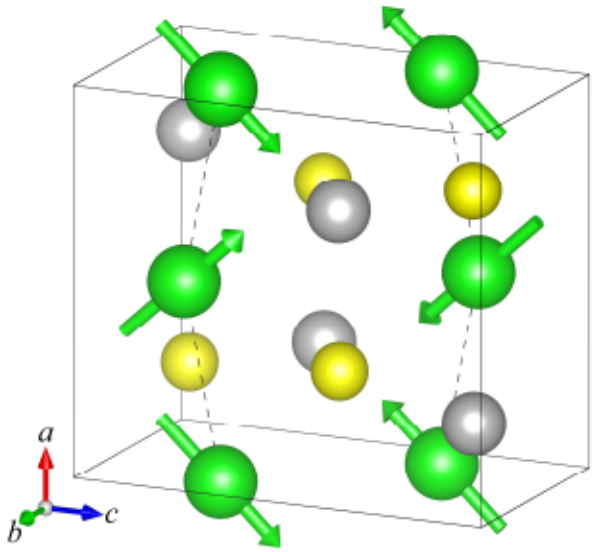

Figure 9.1: Structure of UIrGe. U ions are green, Ir gray and Ge are yellow. The zig-zag chain of the U ions is marked by the dashed line. The arrows show the directions of the magnetic moments according to Ref. [193]

Earlier studies of the UIrGe compound report antiferromagnetic order in the range of $16 - 18\,\mathrm{K}$[53,194,195] in polycrystalline samples. The first work on a single crystal showed comparable results of the heat capacity and the susceptibility measurement and thus confirmed antiferromagnetic order below $15.8\,\mathrm{K}$ but with an additional transition at $14.1\,\mathrm{K}$[196]. The electrical resistivity exhibited a dramatic increase in the ordered state for the current applied along all three orthorhombic axes which is in disagreement with the previous reports[195,197,198]. However, neither the two distinct transitions[199,200] nor the enhanced low-temperature resistivity[201] were confirmed by further studies on different single crystals. A recent study of the

electrical transport properties under hydrostatic pressure revealed very low initial pressure dependence of T_N up to 7 GPa. Further increasing of the applied pressure leads to significant lowering of the Néel temperature which consequently drops to zero around 11 GPa. The temperature dependence of the electrical resistivity at this critical pressure shows a variation of the residual resistivity ρ_0, an enhanced parameter a and a lowering of the antiferromagnetic gap Δ (as described by Equation (3.25))[201].

Metamagnetic transitions were observed for magnetic fields applied along the c axis and b axis and no transition up to 51 T was observed for the a axis[199,202,203]. An earlier study of heat capacity and electrical resistivity in high magnetic fields proposes a phase diagram with two different metamagnetic transitions for the magnetic field applied along the b and c axis[203]. However, the single crystal used in that work was the same as in Ref.[196] showing two transitions in the heat capacity and a strange increase of the electrical resistance in the ordered state, as mentioned above. Later magnetization measurements together with the heat capacity data up to 16 T were used for construction of a new magnetic phase diagram of UIrGe, with a critical field of $\mu_0 H_{c,crit.} \approx 14$ T for the c axis, and $\mu_0 H_{b,crit.} \approx 21$ T for the b axis[199]. This phase diagram exhibit only single metamagnetic phase transition for the c and b axis, respectively, compared to the one in Ref.[203].

A neutron-diffraction experiment on a powder sample[204] was not able to detect any magnetic signal in the ordered state. Further studies on the single-crystalline samples found a propagation vector $(0, 0, 0)$[193]. The symmetry analysis allows eight possible magnetic structures for the moments on U ions. Seven of them lead to the antiferromagnetic ground state and only two were compatible with the measured data. Both proposed magnetic structures have a zero component of the magnetic moment in the b direction, so the U moments are confined to the $a-c$ plane. Better agreement of the measured intensities and model was achieved for the structure with alternating sign of the a component of the U magnetic moment within the zigzag chain, while the c component stays aligned in the chain (see Figure 9.1). The magnetic structure above the metamagnetic transition for the c axis was found to be fully polarized in the direction of the applied magnetic field[205]. This "field-induced ferromagnetic" phase has no component of the magnetic moment in the a direction, compared to the "canted field-induced ferromagnetic" structure of UNiGe[205,206].

This chapter is focused on heat-capacity, magnetization, thermal-expansion, magnetostriction and electrical-resistivity measurements which were performed on a single crystal in magnetic fields up to 14 T. The obtained results confirm the character of the phase diagram presented in Ref.[199] by other bulk measurements and disprove the suggested form from Ref.[203]. A precise thermal-expansion study reveals the mechanism that stands behind the moderate initial pressure dependence of the Néel temperature reported in Ref.[201] that was confirmed by measurement of heat capacity under hydrostatic pressure.

9.2 Results

9.2.1 Field dependence of T_N - heat capacity and susceptibility study

Heat capacity measurements were performed in magnetic fields up to 14 T applied along the c axis and the b axis. The magnetic transition to the ordered state at zero magnetic field is manifested by a lambda-shaped peak at $T_N = 16.5$ K (see Figure 9.2). It agrees well with the previously published data on the singlecrystalline samples[199,200,207] and it is sharper and better defined than transitions published in Refs.[194,196,203]. The reduced step of the heat capacity at T_N is $\Delta c(T)/T \approx 739\,\mathrm{mJ \cdot mol^{-1} \cdot K^{-2}}$. The magnetic field applied along the c axis leads to the gradual shift of the transition to the lower temperatures and also to the change of its character. Initially, it becomes sharper and higher, while around 8 T it starts to lower its height and gets broader again as it gradually gets closer to the expected critical field $\mu_0 H_{c,crit.} \approx 14$ T[199] as can be seen from the Figure 9.2.

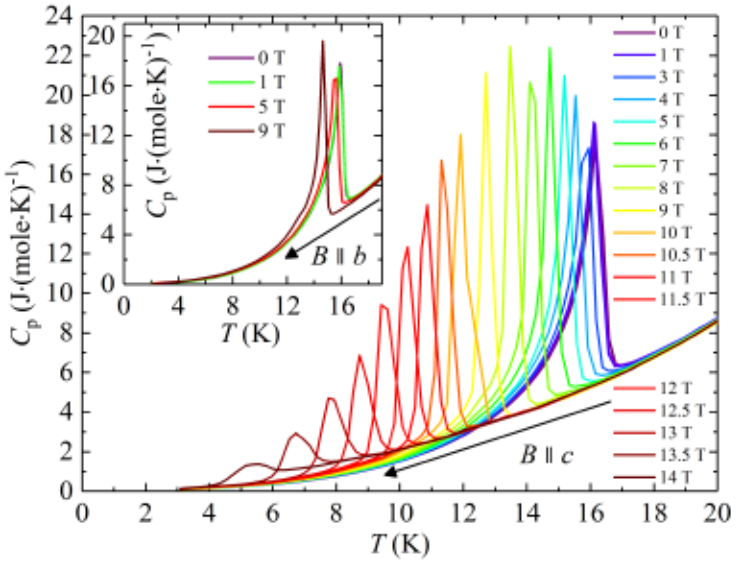

Figure 9.2: Heat capacity of UIrGe measured at various magnetic fields applied along the c axis and b axis (inset). The arrows show the trend of the increased field on the transition temperature.

The effect for the magnetic field applied along the b axis is very similar. As the critical field for this direction is higher $\mu_0 H_{b,crit.} \approx 21$ T[199], also the change of the transition shape is less pronounced up to the highest applied field of 9 T, see inset of Figure 9.2.

The large anisotropy of UIrGe is pronounced in the different temperature dependence of the static magnetic susceptibility (see Figure 9.3). The hard-magnetic axis a exhibits very low susceptibility (not shown) but still with a visible step at T_N. The b axis has a significant maximum in susceptibility at T_{max} well above T_N, here presented only for 7 T scan (see inset of Figure 9.3). Recent studies showed dependence of this anomaly upon the magnetic field applied along b axis[190]. In

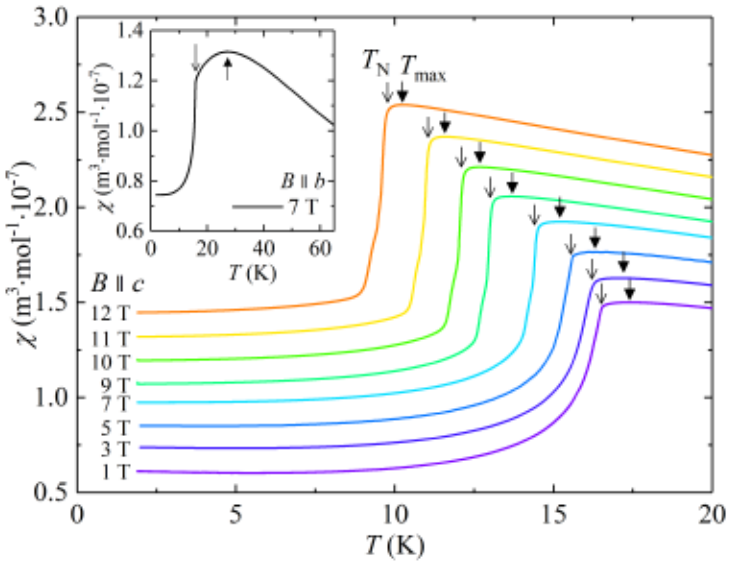

Figure 9.3: Temperature dependence of the static magnetic susceptibility at various external magnetic fields applied along the c and b axis (inset). Two types of arrows mark the T_{N} and T_{max}. The curves are vertically shifted by $0.5 \times 10^{-7}\,\mathrm{m^{-3}} \cdot \mathrm{mol^{-1}}$.

the case of the c axis, these T_{N} and T_{max} anomalies are much less pronounced, but still distinguishable as a clear maximum (T_{max}) and a large drop (T_{N}). The mutual distance of these characteristic temperatures is decreased by the applied magnetic field (see Figure 9.15).

9.2.2 Field dependence of the metamagnetic transition H_{m} - magnetization measurements

The magnetization measurements were performed at various temperatures from 1.9 K up to 16 K in magnetic fields up to 14 T applied along the b and c axis. The hard magnetization direction was measured up to 9 T at 1.9 K. It clearly shows a linear dependence in agreement with the previous report [199]. All curves with the magnetic field applied along the c direction show a clear metamagnetic transition in the temperature range from 6 K up to 16 K. The transition for the 1.9 K isotherm is expected to take place at a magnetic field above 14 T. The observed transitions show a two-step character with a different slope of the two parts, which can be clearly observed below 14.5 K. The arrows in Figure 9.4 show the position of the inflection point in the high field part of the transition, marked as $\mu_0 H_{\mathrm{m}}$.

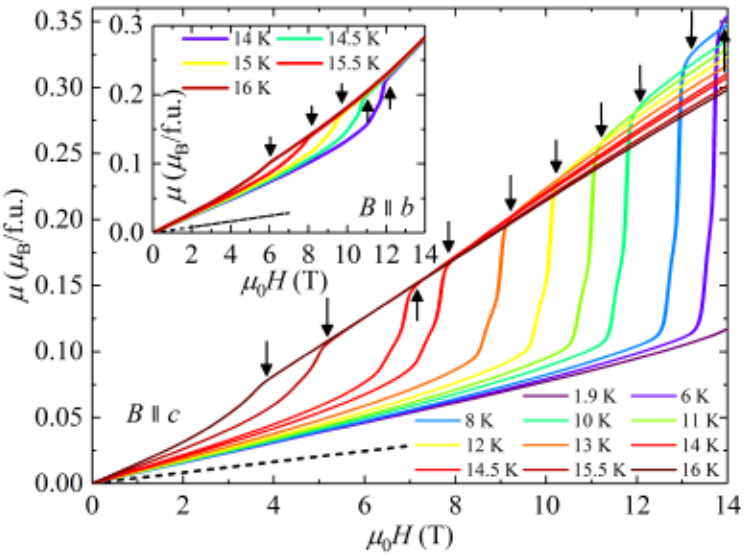

Figure 9.4: Magnetization measured with the field applied along the c axis and b axis (inset). The arrows mark the position of the metamagnetic transition $\mu_0 H_m$. The dashed lines are the data for the magnetization measured with the field applied along the hard magnetization direction a.

Another general trend for these transitions is the gradual change of their character from abroad second-order type transitions at higher temperature (above around 14.5 K and 5 T) to a steep first-order type below 14.5 K.

The magnetization measured with the magnetic field applied along the b axis is plotted in the inset of Figure 9.4. It also exhibits metamagnetic transitions in the measured temperature range from 16 K to 14 K with increasing magnetic field. Such transitions are all of the second-order type in this specific high-temperature range. Their character is again resembling the two-step transition of the c-axis metamagnetism.

9.2.3 Magnetostriction and magnetoresistance induced by metamagnetic transition

The measurement of the highly anisotropic longitudinal and transversal magnetostriction was performed up to 14 T. Results for the magnetic field applied along the c axis at 14.5 K are plotted in Figure 9.5 in comparison with the corresponding magnetization curve. They have very similar character with the two-step and first-order type transition that takes place below 7 T. This transition is manifested as a contraction of the c axis of the unit cell.

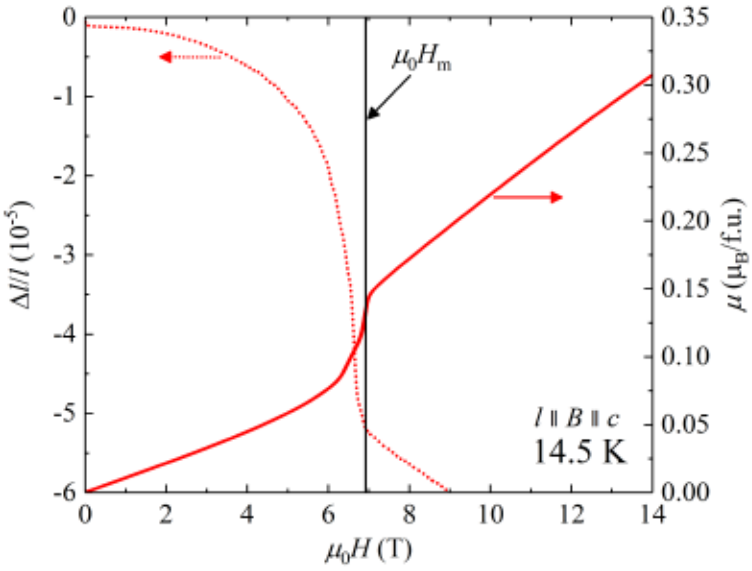

Figure 9.5: Longitudinal magnetostriction for the c direction measured at 14.5 K (left axis, dotted line) compared with the magnetization curve at the same temperature (right axis, solid line). The vertical line marks the position of the $\mu_0 H_m$ transition.

The magnetostriction was also measured at 2 K for the a, b and c axis without any trace of the metamagnetic transition (see Figure 9.6). There is a small positive and almost linear trend for the magnetic hard axis a up to 14 T. The other remaining directions show a steady contraction of a very similar shape. The effect of the magnetic field applied parallel to all three directions on the length of the magnetic easy axis c is shown in Figure 9.7.

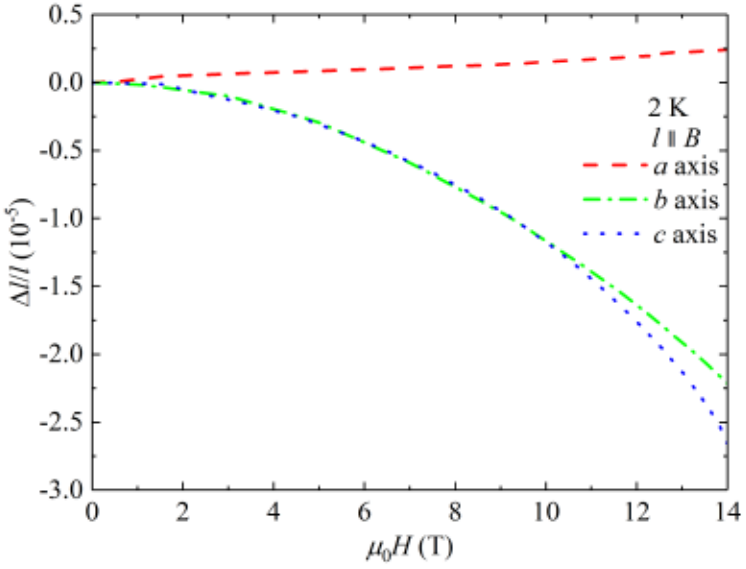

Figure 9.6: Magnetostriction at 2 K for the a, b and c axis measured up to 14 T.

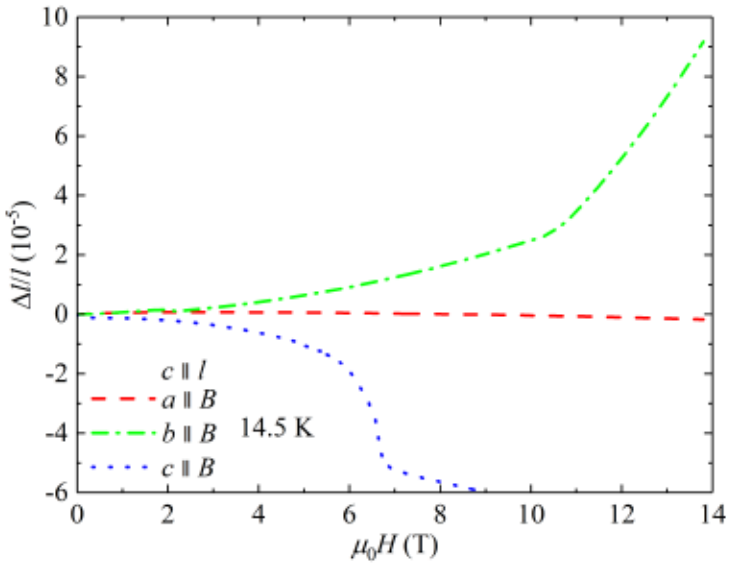

Figure 9.7: Magnetostriction of the c axis for the magnetic field applied along the a, b and c axis at 14.5 K.

A magnetic field applied along the hard magnetization direction a has almost no effect on the length of the c axis. The metamagnetic transition for the field applied along the b axis above 10 T is connected with the expansion of the c axis. Step-like shortening for the longitudinal configuration of the c axis is the same as in Figure 9.5.

The electrical resistivity measured between 350 K and 2 K shows large anisotropy for the electrical current applied along all different directions (see Figure 9.8). The a axis case exhibits a large initial increase of resistivity upon lowering the temperature. It grows till 22 K, where it reaches a broader local maximum. A sharp peak resides directly below T_N (i.e. its maximum is at 15.9 K). The ordered state is manifested as a huge drop of the resistivity. Another interesting feature is a shallow minimum at 7 K, that is positioned directly below this steep decrease (see inset of Figure 9.8). The resistivity then increases slightly again, reaching $\rho_{0,a} = 177\,\mu\Omega\cdot\mathrm{cm}$. The residual-resistivity ratio (RRR), between the values at 350 K and 2 K for this direction is the lowest among all directions reaching the value $\mathrm{RRR}_a = 1.9$. The b axis has broad maximum at 215 K followed by a monotonous decrease with a pronounced knee at T_N. The residual resistivity is $\rho_{0,b} = 42\,\mu\Omega\cdot\mathrm{cm}$ with the $\mathrm{RRR}_b = 8$. The initial trend of the resistivity for the c axis is increasing upon lowering the temperature till a maximum at 34 K. It gradually decreases at lower temperatures and has a steeper slope below T_N. The residual resistivity is $\rho_{0,c} = 90\,\mu\Omega\cdot\mathrm{cm}$ with the $\mathrm{RRR}_c = 3.5$.

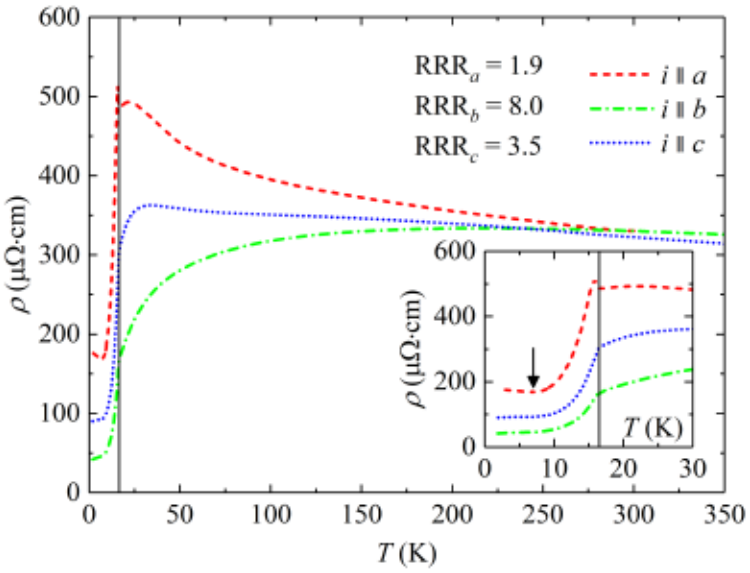

Figure 9.8: Electrical resistivity measured along the a, b and c axis. The vertical line indicates the position of T_N. The inset shows the low-temperature details with the arrow at the position of the minimum for the a axis.

The effect of a magnetic field applied along the c axis on the electrical resistivity for all three directions of the current is plotted in Figure 9.9. The largest effect on the resistivity is visible along the a axis. It continuously lowers the maximum above T_N, smears out the peak anomaly below T_N and dramatically deepens the minimum at lower temperatures. The effect for the b and c axis is less pronounced. It lowers the resistivity above T_N and creates a minimum at 5 K.

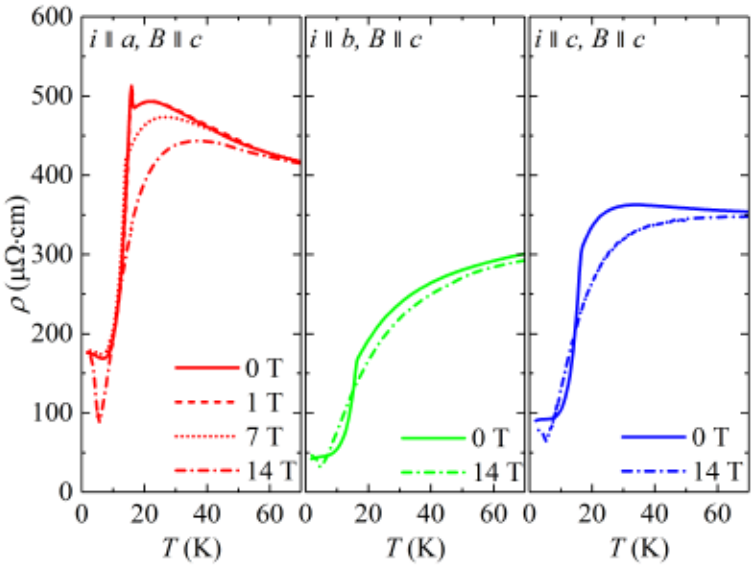

Figure 9.9: Electrical resistivity of the a, b and c axis under an applied magnetic field along the c axis.

The magnetoresistance was measured for various geometries and temperatures. All combinations of the direction of the electrical current and magnetic field up to 14 T(except for the magnetic field pointing along the hard magnetization direction a) are plotted in Figure 9.10.

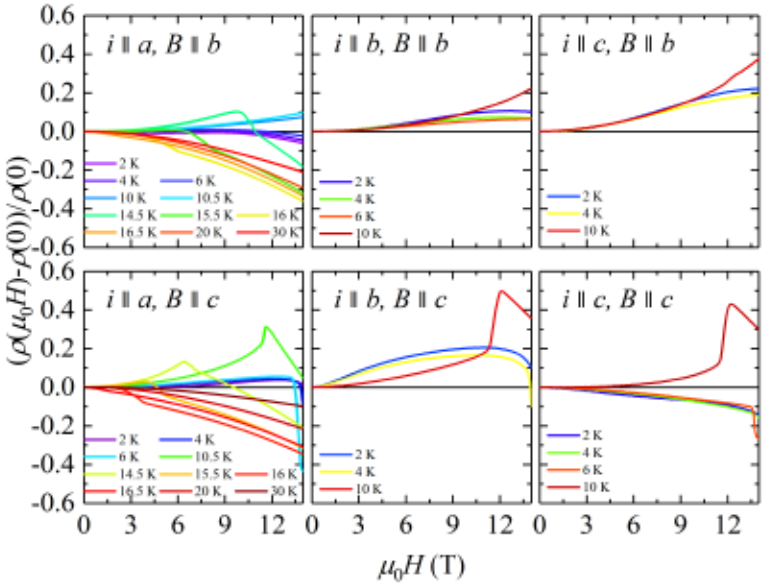

Figure 9.10: Magnetoresistance for various orientations of the electrical current and magnetic field up to 14 T.

Applying the field along the c axis leads to the largest drop of the electrical resistivity for the electrical current along the a axis at low temperatures ($2\,\mathrm{K} - 6\,\mathrm{K}$). Continuous increasing the temperature leads to the emergence of a sharp maximum followed by a linear drop. This anomaly is present also for other geometries.

9.2.4 Anisotropic thermal expansion and pressure induced phenomena

The thermal expansion of UIrGe was measured along the three orthorhombic axes. The linear thermal expansion for the a, b and c direction is plotted in Figure 9.11 on a relative scale. The data sets are vertically shifted to be equal to 0 at $T_\mathrm{N} = 16.5\,\mathrm{K}$. The transition temperature T_N is manifested as a sharp feature for the b and c axis and as an inflection point for the a direction. The estimated ordering temperature is in very good agreement with heat-capacity measurements and with previous polycrystalline and single-crystalline studies of UIrGe[53,194,195,197,198,200,201].

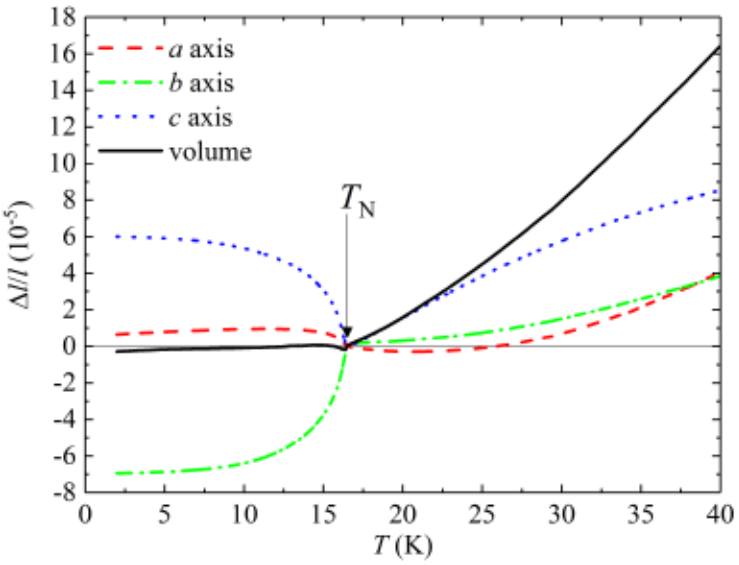

Figure 9.11: Linear thermal expansion of UIrGe for the a (dashed line), b (dashed-dotted line) and c axis (dotted line), together with the calculated volume change (solid line).

The huge anisotropy is evident for all three major crystallographic directions of the unit cell. The smallest effect is for the a axis where a shallow minimum at 21 K precedes the inflection point at T_N. The a axis then starts to increase and below 11.5 K it steadily contracts, resulting in a final small positive length change (6.6×10^{-6} between T_N and 2 K). The unit-cell variation along the b axis is monotonously decreasing in the whole measured temperature range. The pronounced knee at the Néel temperature is followed by a huge contraction that reaches -7×10^{-5} at 2 K (compared to the value at T_N). The initial shortening of the c axis at higher temperature is terminated by the sharp anomaly located at T_N. The following lattice increase exhibits a very similar, but inverse, shape as was observed for the contraction of the b axis. The relative lattice expansion for the c axis at 2 K is 6×10^{-5}. All transitions are continuous i.e. of second-order type. Estimation of the volume change of the orthorhombic structure can be achieved by summing the measured orthogonal components for all three directions. The very similar shape of the opposite lattice changes with comparable sizes leads to an almost zero volume change below T_N (2.7×10^{-6} between T_N and 2 K).

As the character of the heat-capacity transition is dramatically changed for the applied field along the b and c axis, it might be useful to map this effect on the thermal expansion as well. See Figure 9.12 for the thermal expansion measured along the c and b axis with the magnetic field applied parallel to these directions.

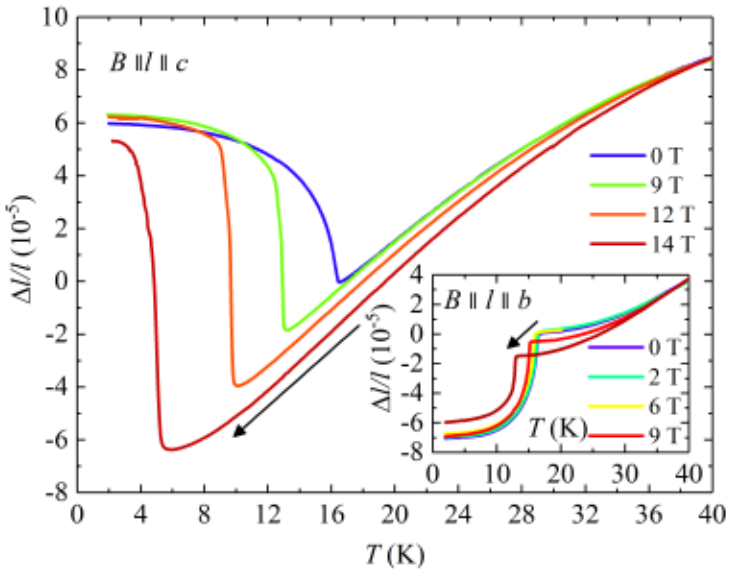

Figure 9.12: Linear thermal expansion along the c and b axis (inset) with the magnetic field applied parallel to these directions. The arrows show the trend of the increased field on the shift of the transitions.

The initial second-order type transition that takes place at $0\,\mathrm{T}$ for the c axis is changed in a step-like, first-order type character in an applied magnetic field of $12\,\mathrm{T}$. The transition itself is shifted to lower temperatures. A similar effect can be observed for the length change of the b axis with the magnetic field applied parallel as well. In this case, the character of the transition stays unchanged up to $9\,\mathrm{T}$. Absolutely no change of neither the shape, nor the position of the transition along the hard magnetic axis a was observed for an applied parallel magnetic field up to $14\,\mathrm{T}$ (not shown).

An overall picture of the calculated linear thermal-expansion coefficients for the a, b, and c axis at zero field is shown in Figure 9.13.

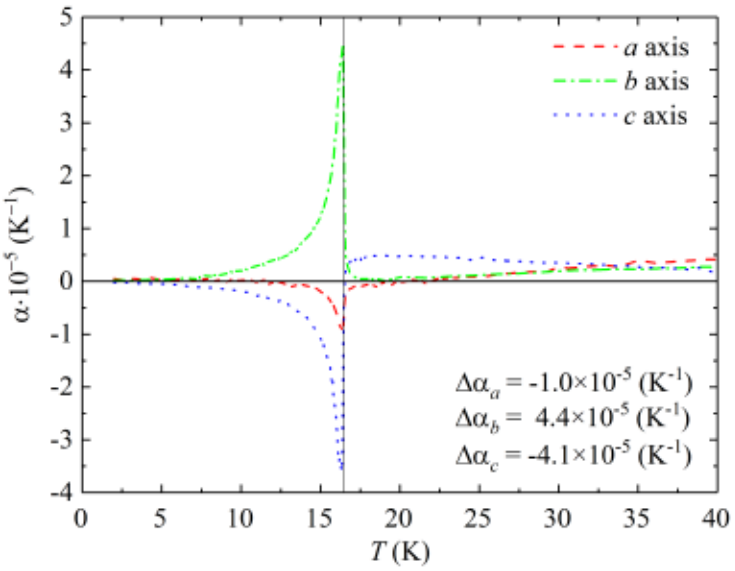

Figure 9.13: Linear thermal expansion coefficients for the a, b and c axis. The vertical line marks the position of T_N.

As the character of the transition at T_N in zero field is second order, the thermodynamic Ehrenfest relation (see Equation (3.19)) can be used. It can give an estimation of the hydrostatic pressure effect using the volume-thermal-expansion coefficient, or for the uniaxial pressure dependences when the linear-thermal-expansion coefficients α_a, α_b or α_c are used. The appropriate steps of the thermal-expansion coefficients at T_N together with the expected pressure dependences are summarized in Table 9.1. It provides a value for the hydrostatic-pressure dependence of T_N reaching only $\frac{dT_m}{dp} = -0.32(5)\,\mathrm{K \cdot GPa^{-1}}$.

Table 9.1: Jumps $\Delta\alpha_i$ of the thermal-expansion coefficients at T_N and the corresponding hydrostatic-pressure and uniaxial-pressure derivatives of T_N predicted using the Ehrenfest relation for UIrGe.

	$\Delta\alpha_i\,(\mathrm{K^{-1}})$	$\frac{dT_m}{dp}\,(\mathrm{K \cdot GPa^{-1}})$
a	$-1.0(1) \times 10^{-5}$	-0.46(5)
b	$4.4(1) \times 10^{-5}$	2.01(5)
c	$-4.1(1) \times 10^{-5}$	-1.87(5)
Volume	$-0.7(1) \times 10^{-5}$	-0.32(5)

Heat capacity measurements by steady-state calorimetry under hydrostatic pressure were conducted to verify this low dependence of the ordering temperature. The arbitrary units of the measurement were scaled with ambient pressure data to obtain a full picture of the pressure dependence of the heat capacity (see Figure 9.14). The transition at T_N is shifted to lower temperature by applying external pressure and

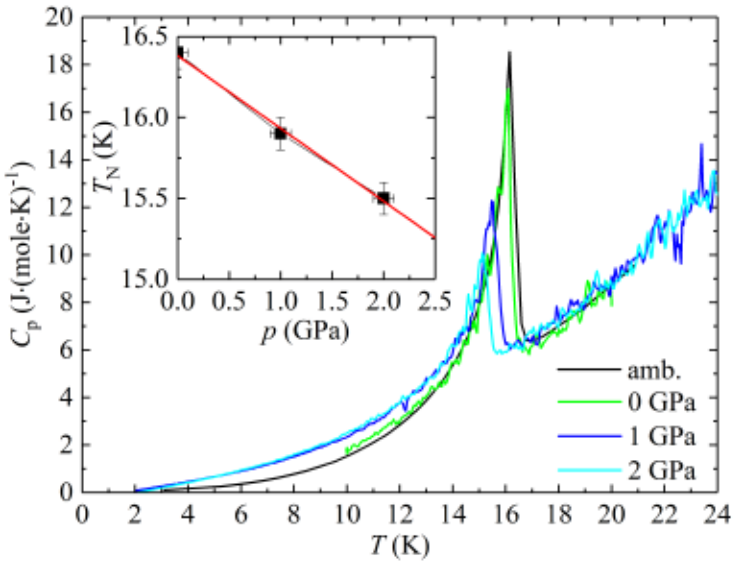

Figure 9.14: Heat capacity of UIrGe measured under hydrostatic pressure up to 2 GPa. The "amb." data are from the heat-capacity measurement at ambient pressure using relaxation method, while the 0 GPa corresponds to the measurement in the closed and not yet loaded pressure cell. The inset shows the pressure dependence of T_N with the corresponding linear fit.

the size of step is decreased. The linear fit of the resulting pressure dependence of T_N gives a slope of $\left(\frac{dT_m}{dp}\right)_{exp} = -0.45(3)\,\mathrm{K}\cdot\mathrm{GPa}^{-1}$ (see inset of Figure 9.14) which is in good agreement with the value estimated from the Ehrenfest relation.

9.3 Discussion

The heat capacity measurements of UIrGe in external magnetic field reveal a strong dependence of the shape and position of the anomaly at T_N when the field is applied along b or c axis. This finding is in agreement with previous reports [199,200] which also show almost no effect when a magnetic field is applied along the hard magnetic axis a. In zero field, the anomaly at $T_N = 16.5\,\mathrm{K}$, connected with the transition to the ordered state, has a clear lambda shape pointing at a second-order magnetic phase transition (see Figure 9.2). An external magnetic field applied along the c axis shifts T_N to lower temperatures and sharpens the anomaly up to 8 T. Further increasing of the applied magnetic field lowers and broadens the anomaly up to the highest value of 14 T. This change of shape can be understood as a sign of the change from an initially second-order magnetic phase transition towards first-order type around 8 T. This interpretation is suggested even for the case of the magnetic field applied along the b axis [190,208] where the same change of shape takes place at 14 T. It is not entirely visible in the data in this study, where the maximum magnetic field applied along b axis was only 9 T (see inset of Figure 9.2). However, the initial trend of sharpening of the transition is already visible at lower fields.

The T_N anomaly itself is manifested as a drop of the susceptibility which is connected with the ground-state antiferromagnetic phase (see Figure 9.3) and it gradually shifts to lower temperatures in applied external magnetic field. Only the effect on the c axis direction was studied in this work as the b-axis case is deeply discussed in Ref.[190]. If the magnetic field is applied along the b axis T_N drop is clearly preceded by a maximum of susceptibility at a higher temperature T_{max} (an illustrative example was measured and is plotted in the inset of Figure 9.3). Further increase of the applied magnetic field along the b axis leads to lowering of T_N (same as for the c-axis case) and, with higher rate, also to a decrease of T_{max}. These two characteristic temperatures merge at the proposed tricritical point (TCP)[190]. For illustrative purpose the field dependence of T_{max} for the b axis from Ref.[190] is added to the magnetic phase diagram in Figure 9.15. Our intention was to follow the characteristic maximum at T_{max} also for the case of the magnetic field applied along the c axis. Despite being very close to T_N, the T_{max} anomaly is clearly visible in the measured magnetic susceptibility for the c direction (see Figure 9.3). Increase of magnetic field leads to a faster shift of T_{max} towards lower temperatures than of T_N, but both anomalies seem not to merge up to the highest applied fields as the susceptibility still exhibits a maximum above the Néel temperature. Nevertheless, the mutual distance of T_N and T_{max} is less than 0.5 K above 9 T so these characteristic temperature appear to merge in the phase diagram in Figure 9.15.

Another sign of the change of the order of the magnetic transition for the magnetic field applied along the c axis is the broad character of the magnetization curves above 14.5 K (i.e. 8 T) and the step-like dependence with observable hysteresis below this temperature (see Figure 9.4). This is in agreement with previous reports[199] and the same effect was observed for the magnetic field along the b axis[190,199]. This onset of step-like magnetization for the case of the b axis takes place below 13 K (i.e. above 14 T)[190]. It is thus beyond the instrumental abilities of this part of study, leaving only observable signs of the change of the b axis transition in the inset of Figure 9.4.

The longitudinal magnetostriction for the c axis, measured on the border between the first- and second-order type of transition at 14.5 K, fully correlates with the field-induced metamagnetic transition and is manifested as a large contraction (see Figure 9.5). It clearly demonstrates that the unit cell is shortened along the c axis when the magnetic moments are all aligned within this direction (in the high-field polarized phase). Similar behavior is valid for the longitudinal magnetostriction along b as it also contracts when approaching the metamagnetic transition (see Figure 9.6). Contrary to this, an obvious elongation of c axis is visible when the magnetic field is applied perpendicular to the b direction trying to align the moments. (see Figure 9.7).

The magnetoresistance for various combinations of the applied current and magnetic field reveal a common sign of the metamagnetic transition in UIrGe. As the temperature of the measured isotherms is reaching the phase boundary with applied external field, it results in a dramatic increase of electrical resistivity. After the phase transition, the electrical resistivity drops rapidly. This effect is more clearly visible for the magnetic field applied along the c axis (see lower row of Figure 9.10) as the applied field of 14 T is large enough to induce these step-like drops. The

largest increase of the electrical resistivity before the transition is visible for the electrical current applied along the b axis on the 10 K isotherm. It is increased by 50% at 12 T as the fluctuation of the magnetic moments slightly below the metamagnetic transition leads to such enormous magnetoresistance. On the other hand, the largest decrease of 45% right after the metamagnetic transition can be found for the electrical current applied along the a direction for the 6 K isotherm at 13 T. In this case, scattering of the conduction electrons in the field-induced and aligned magnetic phase is much lower compared to the AFM state. As can be seen from the case with magnetic field applied along the b axis (see upper row of Figure 9.10), a similar scenario can be expected at higher fields.

The temperature dependence of the electrical resistivity is strongly anisotropic (see Figure 9.8). The largest electron scattering is observed for current applied along the direction of the a axis above the ordering temperature where the resistivity has a broad local maximum at 22 K. Directly above T_N is a very sharp peak, followed by a large drop at lower temperatures. The electrical resistivity then goes through a shallow minimum at the lowest temperatures 7 K. This direction shows the lowest $RRR_a = 1.9$ compared to the other two directions. The b-axis electrical resistivity has a broad maximum and higher temperature, i.e. 215 K followed by knee at T_N and the highest $RRR_b = 8$. The last direction c has has a characteristic maximum at 34 K and intermediate $RRR_c = 3.5$. The electrical resistivity of UIrGe seems to be strongly sample dependent and all scattering processes probably largely depend on the quality of the single crystals. The results of the present study are not in agreement with the first report of the electrical-resistivity measurements where a large low-temperature upturn was observed[196]. Nevertheless, it shows reasonable agreement with the latest study of the electrical properties[201] with subtle differences. This is mostly the absence of the sharp peak above T_N for the electrical resistivity measured along the a direction and the missing shallow minimum at the lower temperatures below T_N. It is suggested, that these features strongly correlate with the RRR of the measured samples, as it reaches a value of 50 in Ref.[201], compared to 8 in the present study. This scenario can be also illustrated by the temperature dependence of the electrical resistivity in applied magnetic field, where this minimum is getting deeper with higher field (see Figure 9.9), keeping the residual resistivity almost pinned to a constant value. It might be a sign of a constant low-temperature contribution to the enhanced resistivity which is non-magnetic and rather structural and thus not affected by the applied magnetic field.

The dramatic anisotropy of UIrGe is also manifested by the significantly different thermal expansion of all three orthorhombic axes. Their temperature dependence is varying even above T_N. The hard-magnetic axis a is only slightly elongated in the ordered state (6.6×10^{-6}), while a much more clear positive length change is observed for the c axis (6×10^{-5}). The temperature dependence of the b-axis length change below T_N is negative (-7×10^{-5}) and its shape strongly resembles the inverse of the c axis. Thanks to these major contributions (b and c) of similar size and opposite sign, the resulting volume change in the ordered state is almost zero, being only slightly negative 2.7×10^{-6}. This volume conservation after the magnetic transition is arranged by stretching of the $a - c$ plane (in which the directions of

magnetic moments are confined, see Figure 9.1 and Ref.[193]) and contraction of the b direction. The well-pronounced transition at T_N both for the b and the c axis is shifted towards lower temperature in the longitudinal configuration and steadily adopts the step-like first-order character. For the c axis, it takes place below 9 T (see Figure 9.12) while for the b axis only the initial tendency of the shape change is visible up to 9 T (see inset of Figure 9.12) as a higher magnetic field would be needed. The Ehrenfest relation for the second-order phase transition gives an estimation of the significantly anisotropic uniaxial pressure dependence of the ordering temperature for the a axis ($-0.46(5)\,\mathrm{K\cdot GPa^{-1}}$), the b axis ($2.01(5)\,\mathrm{K\cdot GPa^{-1}}$) and for the c axis ($-1.87(5)\,\mathrm{K\cdot GPa^{-1}}$). Consequently, the calculated hydrostatic-pressure dependence of T_N estimates a negative and relatively small initial slope of $-0.32(5)\,\mathrm{K\cdot GPa^{-1}}$. This estimation was experimentally confirmed by heat-capacity measurements under hydrostatic pressure up to 2 GPa where the T_N anomaly decreases with pressure and is shifted to lower temperature with a slope of $-0.45(3)\,\mathrm{K\cdot GPa^{-1}}$. This is in reasonable agreement with the calculated value, however the initial hydrostatic-pressure dependence in Ref.[201] is even smaller, i.e. $-0.11\,\mathrm{K\cdot GPa^{-1}}$. All these small negative slopes would lead towards an anomalously high critical pressure where T_N would go to 0 K. The latest high pressure study revealed, that the initial dependence changes its slope around 5 GPa and continues in a steep way towards the first-order step-like transition around 12 GPa where the magnetic transition disappears and T_N drops to 0 K[201].

All above listed results were used for construction of the magnetic phase diagram for field applied along the c axis (see Figure 9.15). Much lower importance was given to the b-axis case, but results for this direction of the applied magnetic field are plotted in Figure 9.15 as well and they are combined with the data set of T_{max} taken from Ref.[190]. The extrapolated critical field at 2 K is taken from Ref.[199].

The overall picture of the magnetic phase diagram agrees with previous heat-capacity and magnetization studies both for the b and the c axis[199], and is completed by other bulk-measurement methods (thermal expansion, magnetostriction, magnetoresistance and electrical resistivity). The detailed study of the behavior of UIrGe with the magnetic field applied along the b axis proposes the presence of a tricritical point (TCP) where the high-temperature and low-field phase-boundary changes from second-order towards first-order type for the low-temperature and the high-field part[190]. This property of the metamagnetic transition was described in Ref.[28]. It is proposed that TCP occurs at the same phase point where T_{max} merges with T_N. The nature of the magnetic properties of UIrGe between these characteristic temperatures is connected with the lowered magnetic susceptibility and thus with possible AFM correlations or short-range AFM order. With decreasing temperature (but still above T_N), these AFM correlations (or AFM short-range order) are enhanced and they reduce the number of paramagnetic moments by the number of AFM coupled moments. This leads to a deviation of the initially paramagnetic susceptibility from the modified Curie-Weiss law and to a gradual decrease (over a broad maximum at T_{max}) towards the sharp drop at T_N. A similar scenario seems to be valid even for the case of the c axis, however with largely reduced energy scale where T_{max} and T_N only differ by 1 K at 1 T. An increase of the magnetic

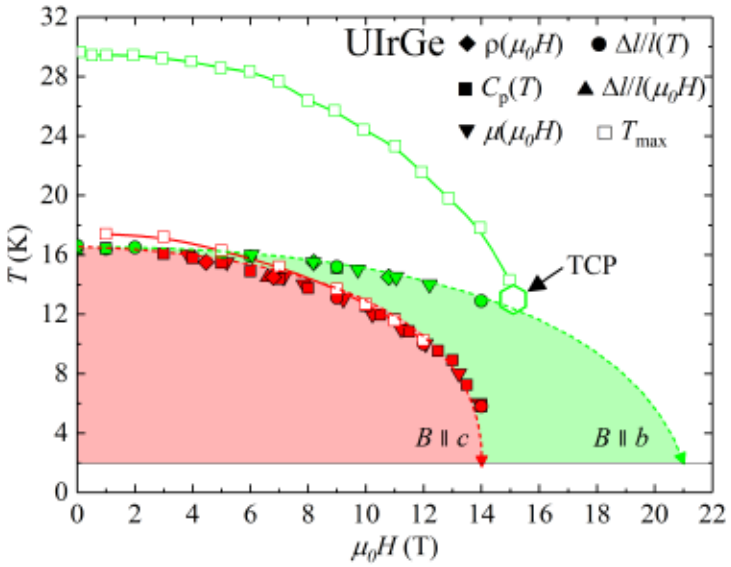

Figure 9.15: Magnetic phase diagram of **UIrGe** for the external magnetic field applied along the c axis (red area) and the b axis (green area). All data points are from magnetoresistance, thermal-expansion, magnetostriction, heat-capacity and magnetization measurements. The arrows mark the extrapolated critical fields at 2 K according to Ref.[199]. Values of T_{max} and TCP for the b axis are taken from Ref.[190]

field applied along the c axis reduces this difference but both temperatures do not completely merge up to the highest applied field (see Figure 9.3). However, T_{max} and T_N are separated only by 0.5 K above 9 T (thus merge in the phase diagram in Figure 9.15) and, in the same region of the magnetic phase diagram the character of the magnetic phase transition is changing from second-order to first-order type, as is demonstrated in the heat-capacity, magnetization and thermal-expansion data. It is thus not possible to undoubtedly propose the presence of a TCP at this position (9 T), in direct analogy with the case of the b axis. Therefore, stronger evidence like measurement of the magnetocaloric effect or the field dependence of heat capacity would be useful for an unquestionable statement about the presence of a TCP even for the magnetic field applied along the c axis. The experimental evidences for the presence of a TCP are quite rare among uranium-based antiferromagnets and, up to now, include only the compounds UNiAl[186], USb_2[187], UN[188], $UIrSi_3$[189] and UAu_2Si_2 - as reported in the previous part of this thesis.

Part V
Conclusions

Results presented in this thesis bring detailed information about three selected uranium-based compounds. All three studied cases are based on the high-quality and well-characterized single crystals which were grown within this work. Common denominator of the three selected compounds is U $5f$-electron magnetism. Rich variety of properties of U-based compounds is demonstrated on different magnetocrystalline anisotropy that is exceptionally low for $U_4Ru_7Ge_6$ on one hand and large for UAu_2Si_2 and UIrGe on the other hand. Combination of macroscopic and microscopic experiments (neutron diffraction) performed within this work allowed to find origin of this behavior. Detailed thermal-expansion measurements performed on all three compounds showed how tiny distortions of the ordered materials can dramatically affect their ground state. In the case of $U_4Ru_7Ge_6$ it leads towards unique establishment of two different U sites. This statement is supported by theoretical calculations and precise polarized-neutron-diffraction experiment. The small distortion of formerly tetragonal lattice of UAu_2Si_2 leads towards an unexpected pressure dependence of its ordering temperature. High-field magnetization, magnetostriction and neutron diffraction investigations of UAu_2Si_2 bring information about the character of metamagnetic transition and about coexistence of the main uncompensated antiferromagnetic ground state with the ferromagnetic component. It was shown, that almost zero volume change for UIrGe stands behind its tiny pressure dependence of Néel temperature. All measurements were performed under various external conditions like high pressure and magnetic field and final magnetic phase diagrams of all three compounds are presented. Magnetic phase diagrams of UAu_2Si_2 and UIrGe contain a tricritical point as a border between the observed first-order and second-order type of phase transition. Such phenomenon is rarely observed for U-based compounds and thus deserves further detailed studies. Continuation of the current project is foreseen mostly on the verge of phase diagrams of all three compounds (i.e. higher pressure, higher field and lower temperature) as well as on the transport properties of UAu_2Si_2 which are not covered in this thesis.

$U_4Ru_7Ge_6$

A single crystal of $U_4Ru_7Ge_6$ was grown for the first time and almost isotropic ferromagnetism in this compound was demonstrated by experiment and by SOI ab initio calculations. This result contrasts with the generally observed huge magnetocrystalline anisotropy in all so far reported ferromagnetic uranium compounds. The ground-state easy-magnetization direction, that is oriented along the [111] axis of the rhombohedrally distorted cubic lattice, was found both by experiment and calculations. The rhombohedral distortion leads to the emergence of two crystallographically inequivalent U sites. This is in agreement with results of calculations providing also different U magnetic moments at inequivalent sites. A change of the easy-magnetization direction and symmetry of the lattice distortion have been ob-

served experimentally at temperatures above $T_r = 5.9\,\mathrm{K}$ to a tetragonal distortion and easy-magnetization along [001], which hold for temperatures up to T_C. This finding is in accordance with the calculated first exited state with the U moment along the [001] direction. The first exited state has been calculated to be $0.9\,\mathrm{meV}$ above the ground state, which is comparable with the value of $k_B T_r (= 0.51\,\mathrm{meV})$. The spin-reorientation transition at T_r is significantly visible in the low-field magnetization, AC susceptibility and thermal expansion data and causes also a weak anomaly at T_r in the temperature dependence of the specific heat and the electrical resistivity. The magnetoelastic interaction induces a very small rhombohedral (tetragonal) distortion of the paramagnetic cubic crystal lattice in case of the [111]([001]) easy-magnetization direction. The very weak magnetocrystalline anisotropy (MA) found in $U_4Ru_7Ge_6$ is the most striking observation for a uranium compound. It is proposed that this is a consequence of a specific environment of each U ion being coordinated by closed Ru and Ge cuboctahedral cages which are preventing the direct $5f$-$5f$ overlap, the key ingredient of the huge MA exhibited by other U-based magnetic compounds.

The observed pressure dependence of T_r and T_C shows their rapid suppression by applied hydrostatic pressure. The critical pressure for T_C is in agreement with a previous study on polycrystalline samples and the verification of the proposed QCP is now in progress as a part of the high-pressure measurements at lower temperatures.

Polarized-neutron diffraction experimentally confirms the presence of distortion of the $U_4Ru_7Ge_6$ cubic lattice in the ferromagnetic state, that was predicted by DFT calculations and thermal-expansion measurements. This transition from the $Im\bar{3}m$ space group to a lower symmetry, most probably described by the $R\bar{3}m$ space group, is caused by the dramatic influence of the SOI on the local symmetry of the U ion site. It results in the emergence of two crystallographically inequivalent U sites, U1 and U2, with remarkably different magnetic moments. It was shown that this effect cannot be observed by usual (unpolarized) neutron diffraction, but it appears clearly in the polarized-neutron-diffraction data. Results of maximum-entropy calculations, together with the model based on dipolar approximation, undoubtedly show the presence of distinct U1 and U2 sites, not only in the ground-state of the compound, but also in the magnetic-field (applied along the easy [111] direction) induced state in the paramagnetic regime. The data suggest a direct connection of the distortion with the magnetic structure, even when field-induced in the paramagnetic state. The large value of the $C_2 \sim 2.5$ parameter of the U2 position suggests an important role of hybridization of $5f$-orbitals with the surrounding Ru $4d$-wavefunctions and is far from the theoretical values for the U^{3+} or U^{4+} free ions. Refinement of the data points to an almost quenched orbital moment at the U1 site. $U_4Ru_7Ge_6$ also exhibits a magnetic moment at the Ru2 position corroborating the strong hybridization of the $5f$ U and $4d$ Ru wave functions.

UAu_2Si_2

A thermal-expansion, magnetostriction and magnetization study was performed to complete a comprehensive magnetic phase diagram for UAu_2Si_2.

The magnetostriction curves measured at higher temperatures confirm the bulk character of the 50 K weak FM phase. The large volume contraction in the UAFM ordered state suggests a large positive pressure dependence of T_m. The linear-thermal-expansion data point at an opposite effect for the uniaxial pressure applied along the tetragonal c axis and within the basal plane. Magnetization measurements in a hydrostatic pressure cell, however, reveal a negligible hydrostatic-pressure effect on T_m, namely $dT_m/dp \approx 0.6(1)\,\mathrm{K \cdot GPa^{-1}}$ in pressures up to 1.0 GPa. An even smaller pressure dependence of the ordering temperature, $dT_m/dp \approx 0.36\,\mathrm{K \cdot GPa^{-1}}$, was obtained from the measurement of the thermal expansion of the a axis under a hydrostatic pressure of 1.65 GPa. These values are much smaller than the prediction from the Ehrenfest relations ($dT_m/dp \approx 4.9(1)\,\mathrm{K \cdot GPa^{-1}}$). Further complex studies involving hydrostatic and uniaxial pressure would be desired to shed more light on the nature of this controversy.

As the order of all the relative length changes is 10^{-5}, it can be expected that some structural changes or distortions of the UAu_2Si_2 unit cell in the ground state can be present. The comparative dilatometry measurements of the linear thermal expansion along the a axis and along the [110] direction clearly show the fourfold symmetry breaking in the basal plane. This may also affect the real low-pressure dependence of the ordering temperature. High-resolution diffraction measurements are needed to find the ground-state space group. Possible candidates are the orthorhombic non-isomorphic subgroups $Fmmm$ and $Immm$, where the first one was found to describe the structure of the high-quality samples of URu_2Si_2 in the hidden-order state. The high-field magnetization measurements revealed a critical field of ≈ 22 T where the ordering temperature T_m is suppressed to 0 K. The hysteresis of this transition emerges at a tricritical point given by $T_m \approx 16$ K and $\mu_0 H_m \approx 16$ T as a sign of the change of the transition from second to first order.

The polarized-neutron diffraction experiments reveal large differences in the spin-density distribution around the U position at various conditions. Further study based on the multipolar order treatment with respect to similarities with URu_2Si_2 are desired and will be part of future research.

High-field neutron diffraction shows a clear transformation of UAFM phase towards the PPM above the metamagnetic transition. An observed hysteresis of the transition at low temperature is in agreement with the high-field magnetization data.

UIrGe

Heat-capacity, magnetization, electrical-resistivity, magnetostriction and thermal-expansion measurements were performed under various external conditions to further study the phase diagram of UIrGe. This particular study was mostly focused on the behavior with the magnetic field applied along the c axis while the case with the magnetic field along b is subject of Ref.[190]. Nevertheless, some comparative measurements were also performed for the configuration with applied magnetic field along b.

The heat-capacity measurements found a strong field dependence of T_N, that is effectively lowered both for the c- and b-axis orientation. A significant change of

the transition-shape at a magnetic field of 8 T applied along the c axis points to a possible change of its character from the second towards the first order. Signs of this change were observed even for the b axis for which this change should happen at higher fields than applied in this study. The sharp drop of the static magnetic susceptibility at T_N, with the field applied along the c axis, is preceded by a maximum at slightly higher temperature T_{max}($\sim$ 1 K for the lowest applied fields). The same pattern was observed also for the b axis but with T_N and T_{max} separated by more than 20 K at the lowest applied fields. This anomaly in the susceptibility is probably connected with some AFM fluctuations or short-range AFM order that lowers the susceptibility even above T_N. The different temperature separation of T_N and T_{max} for the b axis and c axis case points to different energy scales of these effects for both directions. While in the case of magnetic field applied along the b axis, T_N and T_{max} merge at the proposed TCP, for the c-axis case they seem to be separated (although only slightly) up to the highest applied field.

The character of the metamagnetic transition that, is observable on the magnetization curves for the magnetic field applied along the c axis, is changed from the second towards the first-order type around 8 T and 14.5 K, in agreement with the heat-capacity data. Comparable signs of this change were observed for the magnetization with the field applied along the b axis. This metamagnetic transition is connected with a magnetostriction effect in the direction of the applied magnetic field and with a lattice expansion in the perpendicular direction. The length of the hard-magnetic axis a seems to be almost unchanged for magnetic fields up to 14 T.

The large anisotropy of the electrical resistivity is in agreement with the proposed magnetic structure where the largest conduction-electron scattering takes place for the a direction. The residual resistivity for all three directions a, b and c of the current is almost insensitive to the applied magnetic field and is probably connected with lattice imperfections in the single-crystalline samples in agreement with their rather moderate RRRs. Nevertheless, the field dependence of the electrical resistivity close to T_N is significant and leads to a very large magnetoresistance increase below and a decrease above the transition.

The thermal-expansion measurements confirm the large anisotropy of UIrGe with opposite length changes in the ordered state for the b and the c axis. The magnetic hard axis a shows only small elongation and the total volume change below T_N is thus almost zero. The Ehrenfest relation estimates that such a small volume change should lead towards very weak hydrostatic pressure dependence of T_N. This expectation is confirmed by heat-capacity measurements under hydrostatic pressures up to 2 GPa.

Bibliography

[1] J. Klíma and B. Velický, *Kvantová mechanika II* (Univerzita Karlova, nakladatelství Karolinum, 2015).

[2] S. Blundell, "Magnetism in condensed matter," (2001).

[3] M. A. Ruderman and C. Kittel, Phys. Rev. **96**, 99 (1954).

[4] T. Kasuya, Progress of Theoretical Physics **16**, 45 (1956).

[5] K. Yosida, Phys. Rev. **106**, 893 (1957).

[6] I. Dzialoshinskii, J. Exp. Theor. Phys. **5** (1957).

[7] T. Moriya, Phys. Rev. **120**, 91 (1960).

[8] L. Néel, Rev. Mod. Phys. **25**, 58 (1953).

[9] S. Ogawa and N. Sakamoto, J. Phys. Soc. Jpn. **22**, 1214 (1967).

[10] F. R. d. Boer, C. J. Schinkel, J. Biesterbos, and S. Proost, J. Appl. Phys. **40**, 1049 (1969).

[11] P. Coleman, *Introduction to Many-Body Physics* (Cambridge University Press, Cambridge, 2015).

[12] J. L. Smith and E. A. Kmetko, Journal of the Less Common Metals **90**, 83 (1983).

[13] H. H. Hill, pp. 1 – 19.

[14] H. L. Skriver, O. K. Andersen, and B. Johansson, Phys. Rev. Lett. **41**, 42 (1978).

[15] H. L. Skriver, O. K. Andersen, and B. Johansson, Phys. Rev. Lett. **44**, 1230 (1980).

[16] B. Johansson and H. L. Skriver, J. Magn. Magn. Mater. **29**, 217 (1982).

[17] D. D. Koelling, B. D. Dunlap, and G. W. Crabtree, Phys. Rev. B **31**, 4966 (1985).

[18] T. Gasche, M. S. S. Brooks, and B. Johansson, J. Phys.: Condens. Matter **7**, 9499 (1995).

[19] M. S. S. Brooks and P. J. Kelly, Phys. Rev. Lett. **51**, 1708 (1983).

[20] V. Sechovsky, L. Havela, F. R. de Boer, and E. Brück, J. Alloys Compd. **181**, 179 (1992).

[21] V. Sechovský, L. Havela, H. Nakotte, F. R. de Boer, and E. Brück, J. Alloys Compd. **207-208**, 221 (1994).

[22] V. Sechovský and L. Havela, "Chapter 1 magnetism of ternary intermetallic compounds of uranium," in *Handbook of Magnetic Materials*, Vol. Volume 11 (Elsevier, 1998) pp. 1–289.

[23] L. Landau, E. Lifshits, and L. Pitaevskii, *Electrodynamique des milieux continus* (Ed. Librairie du Globe, 1969).

[24] B. Widom, J. Chem. Phys. **43**, 3892 (1965).

[25] H. Stanley, *Introduction to phase transitions and critical phenomena* (Oxford University Press, 1971).

[26] P. Weiss, J. Phys. Theor. Appl. **6**, 661 (1907).

[27] R. B. Griffiths, Phys. Rev. Lett. **24**, 715 (1970).

[28] E. Stryjewski and N. Giordano, Adv. Phys. **26**, 487 (1977).

[29] N. Ashcroft and N. Mermin, *Solid State Physics* (Holt, Rinehart and Winston, 1976).

[30] G. R. Stewart, Rev. Mod. Phys. **56**, 755 (1984).

[31] G. K. White, Nature **187**, 927 (1960).

[32] H. Wada, K. Yoshimura, G. Kido, M. Shiga, M. Mekata, and Y. Nakamura, Solid State Commun. **65**, 23 (1988).

[33] P. G. De Gennes and J. Friedel, J. Phys. Chem. Solids **4**, 71 (1958).

[34] S. Legvold, "Transport properties," in *Magnetic Properties of Rare Earth Metals*, edited by R. J. Elliott (Springer US, Boston, MA, 1972) pp. 335–381.

[35] N. H. Andersen and H. Smith, Phys. Rev. B **19**, 384 (1979).

[36] V. Sechovský, L. Havela, K. Prokeš, and A. V. Andreev, "Anomalous magnetic and related electronic properties of uranium intermetallic compounds," in *Electron Correlations and Materials Properties*, edited by A. Gonis, N. Kioussis, and M. Ciftan (Springer US, Boston, MA, 1999) pp. 97–113.

[37] K. Kadowaki and S. B. Woods, Solid State Commun. **58**, 507 (1986).

[38] Y. Haga, T. Honma, E. Yamamoto, H. Ohkuni, Y. Ōnuki, M. Ito, and N. Kimura, Japanese Journal of Applied Physics **37**, 3604 (1998).

[39] C. Tabata, N. Miura, K. Uhlířová, M. Vališka, H. Saito, H. Hidaka, T. Yanagisawa, V. Sechovský, and H. Amitsuka, Phys. Rev. B **94**, 214414 (2016).

[40] H. Rietveld, J. Appl. Crystallogr. **2**, 65 (1969).

[41] T. Roisnel and J. Rodriguez-Carvajal, in *EPDIC 7 - Seventh European Powder Diffraction Conference*, edited by R. Delhez and E. Mittemeijer (Trans Tech Publications, 2000).

[42] J. Rodriguez-Carvajal, Physica B **192**, 55 (1993).

[43] A. A. Menovsky, J. Magn. Magn. Mater. **76-77**, 631 (1988).

[44] B. Lloret, B. Buffat, B. Chevalier, and J. Etourneau, J. Magn. Magn. Mater. **67**, 232 (1987).

[45] S. A. M. Mentink, G. J. Nieuwenhuys, A. A. Menovsky, and J. A. Mydosh, J. Appl. Phys. **69**, 5484 (1991).

[46] S. F. Matar, B. Chevalier, and R. Pöttgen, Solid State Sci. **27**, 5 (2014).

[47] T. T. M. Palstra, A. A. Menovsky, G. J. Nieuwenhuys, and J. A. Mydosh, J. Magn. Magn. Mater. **54-57**, 435 (1986).

[48] L. Rebelsky, M. W. McElfresh, M. S. Torikachvili, B. M. Powell, and M. B. Maple, J. Appl. Phys. **69**, 4810 (1991).

[49] M. S. Torikachvili, R. F. Jardim, C. C. Becerra, C. H. Westphal, A. Paduan-Filho, V. M. Lopez, and L. Rebelsky, J. Magn. Magn. Mater. **104-107**, 69 (1992).

[50] K. J. Lin, J. S. Hwang, C. S. Wur, R. Hsu, and C. Tien, Solid State Commun. **103**, 185 (1997).

[51] M. Saran and S. P. McAlister, J. Magn. Magn. Mater. **75**, 345 (1988).

[52] C. Tabata, M. Klicpera, B. Ouladdiaf, H. Saito, M. Vališka, K. Uhlířová, N. Miura, V. Sechovský, and H. Amitsuka, Phys. Rev. B **96**, 214442 (2017).

[53] R. Troć and V. H. Tran, J. Magn. Magn. Mater. **73**, 389 (1988).

[54] Y. Skourski, M. D. Kuz'min, K. P. Skokov, A. V. Andreev, and J. Wosnitza, Phys. Rev. B **83**, 214420 (2011).

[55] J. Kamarád, Z. Machátová, and Z. Arnold, Rev. Sci. Instrum. **75**, 5022 (2004).

[56] R. Bachmann, F. J. D. Jr., T. H. Geballe, R. L. Greene, R. E. Howard, C. N. King, H. C. Kirsch, K. N. Lee, R. E. Schwall, H. U. Thomas, and R. B. Zubeck, Rev. Sci. Instrum. **43**, 205 (1972).

[57] P. F. Sullivan and G. Seidel, Phys. Rev. **173**, 679 (1968).

[58] Y. Kraftmakher, *Modulation Calorimetry: Theory and Applications* (Springer Berlin Heidelberg, 2004).

[59] M. Míšek, *Magnetic and transport properties of f-electron compounds under extreme conditions*, Phd thesis (2013).

[60] M. Rotter, H. Müller, E. Gratz, M. Doerr, and M. Loewenhaupt, Rev. Sci. Instrum. **69**, 2742 (1998).

[61] G. Brändli and R. Griessen, Cryogenics **13**, 299 (1973).

[62] R. Pott and R. Schefzyk, J. Phys. E: Sci. Instrum. **16**, 444 (1983).

[63] H. Müller and M. Rotter, *Capacitance Dilatometer DIL20-11 Users Manual* (2012).

[64] J. X. Boucherle, J. Y. Henry, R. J. Papoular, J. Rossat-Mignod, J. Schweizer, F. Tasset, and G. Uimin, Physica B **192**, 25 (1993).

[65] R. Pike and P. Sabatier, *Scattering, Two-Volume Set* (2002).

[66] D. M. Collins, Nature **298**, 49 (1982).

[67] M. Sakata and M. Sato, Acta Crystallographica Section A **46**, 263 (1990).

[68] K. Momma, T. Ikeda, A. A. Belik, and F. Izumi, Powder Diffr. **28**, 184 (2013).

[69] S. F. Gull and J. Skilling, *Quantified Maximum Entropy, MemSys5 Users' Manual* (Maximum Entropy Data Consultants Ltd., Suffolk, 1999).

[70] J. Nocedal, Math. Comp. **35**, 773 (1980).

[71] E. Prince and I. U. o. Crystallo, *International Tables for Crystallography, Mathematical, Physical and Chemical Tables* (John Wiley and Sons, 2004).

[72] T. S. Koritsanszky and P. Coppens, Chem. Rev. **101**, 1583 (2001).

[73] F. Bloch and G. Gentile, Zeitschrift für Physik **70**, 395 (1931).

[74] J. H. van Vleck, Phys. Rev. **52**, 1178 (1937).

[75] J. F. Herbst, Rev. Mod. Phys. **63**, 819 (1991).

[76] M. D. Kuz'min and A. M. Tishin, "Chapter three theory of crystal-field effects in 3d-4f intermetallic compounds," in *Handbook of Magnetic Materials*, Vol. Volume 17, edited by K. H. J. Buschow (Elsevier, 2007) pp. 149–233.

[77] M. S. S. Brooks, Physica B+C **130**, 6 (1985).

[78] O. Eriksson, M. S. S. Brooks, and B. Johansson, Phys. Rev. B **41**, 9087 (1990).

[79] O. Eriksson, M. S. S. Brooks, and B. Johansson, Phys. Rev. B **41**, 7311 (1990).

[80] L. Severin, L. Nordström, M. S. S. Brooks, and B. Johansson, Phys. Rev. B **44**, 9392 (1991).

[81] M. R. Norman and D. D. Koelling, Phys. Rev. B **33**, 3803 (1986).

[82] M. R. Norman, B. I. Min, T. Oguchi, and A. J. Freeman, Phys. Rev. B **38**, 6818 (1988).

[83] F. A. Wedgewood and M. Kuzneitz, J. Phys. C: Solid State Phys. **5**, 3012 (1972).

[84] G. H. Lander, J. Faber, A. J. Freeman, and J. P. Desclaux, Phys. Rev. B **13**, 1177 (1976).

[85] J. Faber and G. H. Lander, Phys. Rev. B **14**, 1151 (1976).

[86] G. H. Lander, M. H. Mueller, D. M. Sparlin, and O. Vogt, Phys. Rev. B **14**, 5035 (1976).

[87] A. Delapalme, G. H. Lander, and P. J. Brown, J. Phys. C: Solid State Phys. **11**, 1441 (1978).

[88] O. Eriksson, B. Johansson, M. S. S. Brooks, and H. L. Skriver, Phys. Rev. B **40**, 9508 (1989).

[89] V. Sechovský, Z. Smetana, G. Hilscher, E. Gratz, and H. Sassik, Physica B+C **102**, 277 (1980).

[90] J. M. Fournier, A. Boeuf, P. Frings, M. Bonnet, J. v. Boucherle, A. Delapalme, and A. Menovsky, Journal of the Less Common Metals **121**, 249 (1986).

[91] P. H. Frings, J. J. M. Franse, A. Menovsky, S. Zemirli, and B. Barbara, J. Magn. Magn. Mater. **54**, 541 (1986).

[92] M. Wulff, G. H. Lander, B. Lebech, and A. Delapalme, Phys. Rev. B **39**, 4719 (1989).

[93] B. Lebech, M. Wulff, and G. H. Lander, J. Appl. Phys. **69**, 5891 (1991).

[94] M. S. S. Brooks, O. Eriksson, B. Johansson, J. J. M. Franse, and P. H. Frings, J. Phys. F: Met. Phys. **18**, L33 (1988).

[95] G. Busch and O. Vogt, Journal of the Less Common Metals **62**, 335 (1978).

[96] C. F. Buhrer, J. Phys. Chem. Solids **30**, 1273 (1969).

[97] O. Eriksson, M. S. S. Brooks, B. Johansson, R. C. Albers, and A. M. Boring, J. Appl. Phys. **69**, 5897 (1991).

[98] B. R. Cooper, R. Siemann, D. Yang, P. Thayamballi, and A. Banerjea, *Hybridization-induced anisotropy in cerium and actinide systems* (North-Holland, Netherlands, 1985).

[99] B. R. Cooper, G. J. Hu, N. Kioussis, and J. M. Wills, J. Magn. Magn. Mater. **63**, 121 (1987).

[100] B. Chevalier, B. Buffat, B. Lloret, B. Czeska, J. Etourneau, A. Sulpice, J. Odin, J. Chaussy, J. Peyrard, P. Lejay, and R. Tournier, **1**, 41 (1986).

[101] S. K. Dhar, R. J. Begum, P. Raj, P. Suryanarayana, L. C. Gupta, and R. Vijayaraghavan, Solid State Commun. **83**, 965 (1992).

[102] J. G. Park and B. R. Coles, J. Phys.: Condens. Matter **6**, 1425 (1994).

[103] E. Colineau, F. Wastin, E. J. Higgins, and J. Rebizant, J. Alloys Compd. **317–318**, 336 (2001).

[104] H. Hidaka, S. Takahashi, Y. Shimizu, T. Yanagisawa, and H. Amitsuka, J. Phys. Soc. Jpn. **80**, SA102 (2011).

[105] M. Vališka, M. Diviš, and V. Sechovský, Phys. Rev. B **95**, 085142 (2017).

[106] M. Vališka, M. Klicpera, P. Doležal, O. Fabelo, A. Stunault, M. Diviš, and V. Sechovský, Phys. Rev. B **97**, 125128 (2018).

[107] M. B. Brodsky, Rep. Prog. Phys. **41**, 1547 (1978).

[108] E. Du Trémolet de Lacheisserie, D. Gignoux, and M. Schlenker, *Magnetism* (Springer, 2005).

[109] K. Koepernik and H. Eschrig, Phys. Rev. B **59**, 1743 (1999).

[110] J. P. Perdew and Y. Wang, Phys. Rev. B **45**, 13244 (1992).

[111] J. P. Perdew, K. Burke, and M. Ernzerhof, Phys. Rev. Lett. **77**, 3865 (1996).

[112] M. W. McElfresh, J. H. Hall, R. R. Ryan, J. L. Smith, and Z. Fisk, Acta Crystallographica Section C **46**, 1579 (1990).

[113] A. Arrott, Phys. Rev. **108**, 1394 (1957).

[114] A. Arrott and J. E. Noakes, Phys. Rev. Lett. **19**, 786 (1967).

[115] H. Yamada, Phys. Lett. A **55**, 235 (1975).

[116] E. P. Wohlfarth, J. Appl. Phys. **39**, 1061 (1968).

[117] R. Viswanathan, J. Phys. F: Met. Phys. **4**, L57 (1974).

[118] A. V. Andreev, "Chapter 2 thermal expansion anomalies and spontaneous magnetostriction in rare-earth intermetallics with cobalt and iron," in *Handbook of Magnetic Materials*, Vol. Volume 8 (Elsevier, 1995) pp. 59–187.

[119] I. Aroyo Mois, M. Perez-Mato Juan, C. Capillas, E. Kroumova, S. Ivantchev, G. Madariaga, A. Kirov, and H. Wondratschek, "Bilbao crystallographic server: I. databases and crystallographic computing programs," (2006).

[120] K. Momma and F. Izumi, J. Appl. Crystallogr. **44**, 1272 (2011).

[121] J. C. Slater, The Journal of Chemical Physics **41**, 3199 (1964).

[122] P. J. Brown, "Magnetic form factors," in *International Tables for Crystallography*, Vol. C, edited by E. Prince (Wiley, 2006) Book section 4.4, pp. 454–461.

[123] A. J. Freeman, J. P. Desclaux, G. H. Lander, and J. Faber, Phys. Rev. B **13**, 1168 (1976).

[124] L. Paolasini, J. Paixao, G. H. Lander, A. Delapalme, N. Sato, and T. Komatsubara, J. Phys.: Condens. Matter **5**, 8905 (1993).

[125] E. R. Callen and H. B. Callen, Phys. Rev. **129**, 578 (1963).

[126] P. Durga, K. P. Arjun, V. K. Pecharsky, and J. K. A. Gschneidner, J. Phys.: Condens. Matter **25**, 396002 (2013).

[127] M. Shimizu, Physica B **159**, 26 (1989).

[128] P. Mohn, K. Schwarz, and D. Wagner, Physica B **161**, 153 (1990).

[129] V. H. Tran, R. Troc, G. André, F. Bourée, and M. Kolenda, J. Phys.: Condens. Matter **12**, 5879 (2000).

[130] G. van der Laan and B. T. Thole, Phys. Rev. B **53**, 14458 (1996).

[131] G. H. Lander, M. S. S. Brooks, and B. Johansson, Phys. Rev. B **43**, 13672 (1991).

[132] K. Kaneko, N. Metoki, N. Bernhoeft, G. H. Lander, Y. Ishii, S. Ikeda, Y. Tokiwa, Y. Haga, and Y. Ōnuki, Phys. Rev. B **68**, 214419 (2003).

[133] A. Hiess, F. Boudarot, S. Coad, P. J. Brown, P. Burlet, G. H. Lander, M. S. S. Brooks, D. Kaczorowski, A. Czopnik, and R. Troc, EPL (Europhysics Letters) **55**, 267 (2001).

[134] R. C. Maglic, G. H. Lander, M. H. Mueller, and R. Kleb, Phys. Rev. B **17**, 308 (1978).

[135] A. Hjelm, O. Eriksson, and B. Johansson, Phys. Rev. Lett. **71**, 1459 (1993).

[136] A. Hjelm, J. Trygg, O. Eriksson, B. Johansson, and J. Wills, Phys. Rev. B **50**, 4332 (1994).

[137] J. A. Paixão, G. H. Lander, A. Delapalme, H. Nakotte, F. R. d. Boer, and E. Brück, EPL (Europhysics Letters) **24**, 607 (1993).

[138] M. S. S. Brooks, O. Eriksson, and B. Johansson, J. Phys.: Condens. Matter **1**, 5861 (1989).

[139] M. Taupin, J. P. Sanchez, J. P. Brison, D. Aoki, G. Lapertot, F. Wilhelm, and A. Rogalev, Phys. Rev. B **92**, 035124 (2015).

[140] K. Prokeš, A. de Visser, Y. K. Huang, B. Fåk, and E. Ressouche, Phys. Rev. B **81**, 180407 (2010).

[141] A. Hariki, A. Hausoel, G. Sangiovanni, and J. Kuneš, Phys. Rev. B **96**, 155135 (2017).

[142] N. Kernavanois, B. Grenier, A. Huxley, E. Ressouche, J. P. Sanchez, and J. Flouquet, Phys. Rev. B **64**, 174509 (2001).

[143] P. Burlet, R. Troc, D. Kaczorowski, H. Noël, and J. Rossat-Mignod, J. Magn. Magn. Mater. **130**, 237 (1994).

[144] A. de Visser, F. E. Kayzel, A. A. Menovsky, J. J. M. Franse, J. van den Berg, and G. J. Nieuwenhuys, Phys. Rev. B **34**, 8168 (1986).

[145] A. de Visser, J. J. M. Franse, and J. Flouquet, Physica B **161**, 324 (1990).

[146] G. Motoyama, N. Yokoyama, A. Sumiyama, and Y. Oda, J. Phys. Soc. Jpn. **77**, 123710 (2008).

[147] S. Ran, C. T. Wolowiec, I. Jeon, N. Pouse, N. Kanchanavatee, B. D. White, K. Huang, D. Martien, T. DaPron, D. Snow, M. Williamsen, S. Spagna, P. S. Riseborough, and M. B. Maple, Proceedings of the National Academy of Sciences **113**, 13348 (2016).

[148] A. V. Andreev, Y. Skourski, D. I. Gorbunov, and K. Prokeš, Physica B (2017), https://doi.org/10.1016/j.physb.2017.06.025.

[149] A. V. Andreev, S. Yasin, Y. Skourski, A. A. Zvyagin, S. Zherlitsyn, and J. Wosnitza, Phys. Rev. B **87**, 214409 (2013).

[150] F. Honda, G. Oomi, A. V. Andreev, V. Sechovský, and A. A. Menovsky, Physica B **259-261**, 256 (1999).

[151] A. Szytuka, S. Siek, J. Leciejewicz, A. Zygmunt, and Z. Ban, J. Phys. Chem. Solids **49**, 1113 (1988).

[152] T. D. Matsuda, N. Metoki, Y. Haga, S. Ikeda, K. Kaneko, E. Yamamoto, and Y. Onuki, J. Phys.: Condens. Matter **15**, S2023 (2003).

[153] L. Chełmicki, J. Leciejewicz, and A. Zygmunt, J. Phys. Chem. Solids **46**, 529 (1985).

[154] L. Chełmicki, J. Leciejewicz, and A. Zygmunt, Solid State Commun. **48**, 177 (1983).

[155] H. Ptasiewicz-Bak, J. Phys. F: Met. Phys. **11**, 1225 (1981).

[156] T. Honma, H. Amitsuka, S. Yasunami, K. Tenya, T. Sakakibara, H. Mitamura, T. Goto, G. Kido, S. Kawarazaki, Y. Miyako, K. Sugiyama, and M. Date, J. Phys. Soc. Jpn. **67**, 1017 (1998).

[157] A. J. Dirkmaat, T. Endstra, E. A. Knetsch, G. J. Nieuwenhuys, J. A. Mydosh, A. A. Menovsky, F. R. de Boer, and Z. Tarnawski, Phys. Rev. B **41**, 2589 (1990).

[158] T. D. Matsuda, Y. Haga, S. Ikeda, A. Galatanu, E. Yamamoto, H. Shishido, M. Yamada, J.-I. Yamaura, M. Hedo, Y. Uwatoko, T. Matsumoto, T. Tada, S. Noguchi, T. Sugimoto, K. Kuwahara, K. Iwasa, M. Kohgi, R. Settai, and Y. Ōnuki, J. Phys. Soc. Jpn. **74**, 1552 (2005).

[159] F. Honda, N. Metoki, T. D. Matsuda, Y. Haga, and Y. Ōnuki, J. Phys.: Condens. Matter **18**, 479 (2006).

[160] R. Troć, M. Samsel-Czekała, J. Stępień-Damm, and B. Coqblin, Phys. Rev. B **85**, 224434 (2012).

[161] T. T. M. Palstra, A. A. Menovsky, J. v. d. Berg, A. J. Dirkmaat, P. H. Kes, G. J. Nieuwenhuys, and J. A. Mydosh, Phys. Rev. Lett. **55**, 2727 (1985).

[162] C. Tabata, Y. Ihara, S. Shimmura, N. Miura, H. Hidaka, T. Yanagisawa, and H. Amitsuka, ArXiv e-prints (2017).

[163] S. Tonegawa, S. Kasahara, T. Fukuda, K. Sugimoto, N. Yasuda, Y. Tsuruhara, D. Watanabe, Y. Mizukami, Y. Haga, T. D. Matsuda, E. Yamamoto, Y. Onuki, H. Ikeda, Y. Matsuda, and T. Shibauchi, Nat. Commun. **5**, 4188 (2014).

[164] K. Kuwahara, H. Amitsuka, T. Sakakibara, O. Suzuki, S. Nakamura, T. Goto, M. Mihalik, A. Menovsky, A. de Visser, and J. M. Franse, J. Phys. Soc. Jpn. **66**, 3251 (1997).

[165] J. Kamarád, K. Kamenev, and Z. Arnold, "Strain gage method of volume measurements under hydrostatic pressure," in *High Pressure Science and Technology, Proceedings of the Joint XV AIRAPT and XXXIII EHPRG International Conference*, edited by W. A.Trzeciakowski (World Scientific, 1996) Book section Instrumentation and Experimental Techniques, pp. 51–53.

[166] G. W. Scheerer, W. Knafo, D. Aoki, G. Ballon, A. Mari, D. Vignolles, and J. Flouquet, Phys. Rev. B **85**, 094402 (2012).

[167] H. R. Ott, K. Andres, and P. H. Schmidt, Physica B+C **102**, 148 (1980).

[168] R. Okazaki, T. Shibauchi, H. J. Shi, Y. Haga, T. D. Matsuda, E. Yamamoto, Y. Onuki, H. Ikeda, and Y. Matsuda, Science **331**, 439 (2011).

[169] T. Shibauchi, H. Ikeda, and Y. Matsuda, Philos. Mag. **94**, 3747 (2014).

[170] S. Tonegawa, K. Hashimoto, K. Ikada, Y. H. Lin, H. Shishido, Y. Haga, T. D. Matsuda, E. Yamamoto, Y. Onuki, H. Ikeda, Y. Matsuda, and T. Shibauchi, Phys. Rev. Lett. **109**, 036401 (2012).

[171] S. Tonegawa, K. Hashimoto, K. Ikada, Y. Tsuruhara, Y. H. Lin, H. Shishido, Y. Haga, T. D. Matsuda, E. Yamamoto, Y. Onuki, H. Ikeda, Y. Matsuda, and T. Shibauchi, Phys. Rev. B **88**, 245131 (2013).

[172] S. Kambe, Y. Tokunaga, H. Sakai, T. D. Matsuda, Y. Haga, Z. Fisk, and R. E. Walstedt, Phys. Rev. Lett. **110**, 246406 (2013).

[173] S. C. Riggs, M. C. Shapiro, A. V. Maharaj, S. Raghu, E. D. Bauer, R. E. Baumbach, P. Giraldo-Gallo, M. Wartenbe, and I. R. Fisher, Nat. Commun. **6**, 6425 (2015).

[174] C. Tabata, T. Inami, S. Michimura, M. Yokoyama, H. Hidaka, T. Yanagisawa, and H. Amitsuka, Philos. Mag. **94**, 3691 (2014).

[175] T. Yanagisawa, to be published .

[176] T. Yanagisawa, S. Mombetsu, H. Hidaka, H. Amitsuka, M. Akatsu, S. Yasin, S. Zherlitsyn, J. Wosnitza, K. Huang, and M. Brian Maple, J. Phys. Soc. Jpn. **82**, 013601 (2012).

[177] E. Hassinger, G. Knebel, K. Izawa, P. Lejay, B. Salce, and J. Flouquet, Phys. Rev. B **77**, 115117 (2008).

[178] J. J. Neumeier, A. L. Cornelius, and K. Andres, Phys. Rev. B **64**, 172406 (2001).

[179] G. M. Schmiedeshoff, S. M. Hollen, S. L. Bud'ko, and P. C. Canfield, AIP Conference Proceedings **850**, 1297 (2006).

[180] A. Gasparini, Y. K. Huang, J. Hartbaum, H. v. Löhneysen, and A. de Visser, Phys. Rev. B **82**, 052502 (2010).

[181] S. Sakarya, N. H. van Dijk, A. de Visser, and E. Brück, Phys. Rev. B **67**, 144407 (2003).

[182] A. Pippard, *Elements of Classical Thermodynamics:For Advanced Students of Physics* (Cambridge University Press, 1964).

[183] R. Eloirdi, C. Giacobbe, P. A. Celdran, N. Magnani, G. H. Lander, J. C. Griveau, E. Colineau, K. Miyake, and R. Caciuffo, Phys. Rev. B **95**, 094517 (2017).

[184] M. S. da Luz, J. J. Neumeier, R. K. Bollinger, A. S. Sefat, M. A. McGuire, R. Jin, B. C. Sales, and D. Mandrus, Phys. Rev. B **79**, 214505 (2009).

[185] V. F. Correa, S. Francoual, M. Jaime, N. Harrison, T. P. Murphy, E. C. Palm, S. W. Tozer, A. H. Lacerda, P. A. Sharma, and J. A. Mydosh, Phys. Rev. Lett. **109**, 246405 (2012).

[186] E. Brück, H. P. Van der Meulen, A. A. Menovsky, F. R. De Boer, P. F. De Châtel, J. J. M. Franse, J. A. A. J. Perenboom, T. T. J. M. Berendschot, H. Van Kempen, L. Havela, and V. Sechovský, J. Magn. Magn. Mater. **104-107**, 17 (1992).

[187] R. L. Stillwell, I. L. Liu, N. Harrison, M. Jaime, J. R. Jeffries, and N. P. Butch, Phys. Rev. B **95**, 014414 (2017).

[188] K. Shrestha, D. Antonio, M. Jaime, N. Harrison, D. S. Mast, D. Safarik, T. Durakiewicz, J. C. Griveau, and K. Gofryk, Sci. Rep. **7**, 6642 (2017).

[189] J. Valenta, F. Honda, M. Vališka, P. Opletal, J. Kaštil, M. Míšek, M. Diviš, L. Sandratskii, J. Prchal, and V. Sechovský, Phys. Rev. B **97**, 144423 (2018).

[190] J. Pospíšil, Y. Haga, Y. Kohama, A. Miyake, S. Kambe, N. Tateiwa, M. Vališka, P. Proschek, J. Prokleška, V. Sechovský, M. Tokunaga, K. Kindo, A. Matsuo, and E. Yamamoto, Phys. Rev. B **98**, 014430 (2018).

[191] E. Ressouche, R. Ballou, F. Bourdarot, D. Aoki, V. Simonet, M. T. Fernandez-Diaz, A. Stunault, and J. Flouquet, Phys. Rev. Lett. **109**, 067202 (2012).

[192] F. Bourdarot, S. Raymond, and L.-P. Regnault, Philos. Mag. **94**, 3702 (2014).

[193] K. Prokeš, H. Nakotte, V. Sechovský, M. Mihalik, and A. V. Andreev, Physica B **350**, E199 (2004).

[194] A. P. Ramirez, B. Batlogg, and E. Bucher, J. Appl. Phys. **61**, 3189 (1987).

[195] K. H. J. Buschow, E. Brück, R. G. van Wierst, F. R. de Boer, L. Havela, V. Sechovsky, P. Nozar, E. Sugiura, M. Ono, M. Date, and A. Yamagishi, J. Appl. Phys. **67**, 5215 (1990).

[196] K. Prokeš, T. Tahara, T. Fujita, H. Goshima, T. Takabatake, M. Mihalik, A. A. Menovsky, S. Fukuda, and J. Sakurai, Phys. Rev. B **60**, 9532 (1999).

[197] B. Chevalier, B. Lloret, P. Gravereau, B. Buffat, and J. Etourneau, J. Magn. Magn. Mater. **75**, 13 (1988).

[198] V. H. Tran, R. Troć, and D. Badurski, J. Magn. Magn. Mater. **87**, 291 (1990).

[199] S. Yoshii, A. V. Andreev, E. Brück, J. C. P. Klaasse, K. Prokeš, F. R. d. Boer, M. Hagiwara, K. Kindo, and V. Sechovský, J. Phys. Conf. Ser. **51**, 151 (2006).

[200] V. Sechovský, J. Vejpravová, A. V. Andreev, F. Honda, K. Prokeš, and E. Šantavá, Physica B **359-361**, 1126 (2005).

[201] J. Pospíšil, J. Gouchi, Y. Haga, F. Honda, Y. Uwatoko, N. Tateiwa, S. Kambe, S. Nagasaki, Y. Homma, and E. Yamamoto, J. Phys. Soc. Jpn. **86**, 044709 (2017).

[202] S. Chang, H. Nakotte, A. M. Alsmadi, A. H. Lacerda, M. H. Jung, M. Mihalik, K. Prokeš, J. C. P. Klaasse, E. Brück, and F. R. De Boer, International Journal of Modern Physics B **16**, 3041 (2002).

[203] S. Chang, M. H. Jung, H. Nakotte, E. Brück, J. C. P. Klaasse, M. Mihalik, A. H. Lacerda, K. Prokeš, M. S. Torikachvili, and A. J. Schultz, J. Appl. Phys. **89**, 7186 (2001).

[204] V. H. Tran, F. Bourée, G. André, and R. Troc, Solid State Commun. **98**, 111 (1996).

[205] K. Prokeš, V. Sechovský, F. R. d. Boer, and A. V. Andreev, J. Phys.: Condens. Matter **20**, 104221 (2008).

[206] K. Prokeš, P. F. de Châtel, E. Brück, F. R. de Boer, K. Ayuel, H. Nakotte, and V. Sechovský, Phys. Rev. B **65**, 144429 (2002).

[207] K. Prokeš, M. Bartkowiak, O. Rivin, O. Prokhnenko, T. Förster, S. Gerischer, R. Wahle, Y. K. Huang, and J. A. Mydosh, Phys. Rev. B **96**, 121117 (2017).

[208] J. Pospíšil, Y. Haga, S. Kambe, Y. Tokunaga, N. Tateiwa, D. Aoki, F. Honda, A. Nakamura, Y. Homma, E. Yamamoto, and T. Yamamura, Phys. Rev. B **95**, 155138 (2017).

List of Figures

List of Tables

List of Publications

1. J. Pospíšil, Y. Haga, Y. Kohama, A. Miyake, S. Kambe, N. Tateiwa, **M. Vališka**, P. Proschek, J. Prokleška, V. Sechovský, M. Tokunaga, K. Kindo, A. Matsuo, and E. Yamamoto. Magnetic field induced phenomena in UIrGe in fields applied along the b axis. *Phys. Rev. B,* **98**, 014430, 2018

2. J. Valenta, F. Honda, **M. Vališka**, P. Opletal, J. Kaštil, M. Míšek, M. Diviš, L. Sandratskii, J. Prchal, and V. Sechovský. Antiferromagnetism and phase transitions in noncentrosymmetric UIrSi3. *Phys. Rev. B*, **97**(14), 144423, 2018

3. **M. Vališka**, M. Klicpera, P. Doležal, O. Fabelo, A. Stunault, M. Diviš, and V. Sechovský. Effect of lattice distortion on uranium magnetic moments in U4Ru7Ge6 studied by polarized neutron diffraction. *Phys. Rev. B*, **97**(12), 125128, 2018

4. A. Bartha, **M. Vališka**, M. Míšek, P. Proschek, J. Kaštil, M. Dušek, V. Sechovský, and J. Prokleška CePd2Ga3 and CePd2Zn3 - Kondo lattices and magnetic behaviour. *Physica B*, **536**, 413417, 2018

5. D. Savchenko, R. Tarasenko, **M. Vališka**, J. Kopeček, L. Fekete, K. Carva, V. Holý, G. Springholz, V. Sechovský, and J. Honolka. Local moment formation and magnetic coupling of Mn dopants in Bi2Se3: A low-temperature ferromagnetic resonance study. *Physica B*, **536**, 604613, 2018

6. Ch, Tabata, M. Klicpera, B. Ouladdiaf, H. Saito, **M. Vališka**, K. Uhlířová, N. Miura, V. Sechovský, and H.Amitsuka. Neutron diffraction study on single-crystalline UAu2Si2. *Phys. Rev. B*, **96**(21), 214442, 2017

7. **M. Vališka**, M. Diviš, and V. Sechovský. Uranium ferromagnet with negligible magnetocrystalline anisotropy: U4Ru7Ge6. *Phys. Rev. B*, **95**(8), 085142, 2017

8. **M. Vališka**, J. Warmuth, M. Michiardi, M. Vondráček, A. S. Ngankeu, V. Holý, V. Sechovský, G. Springholz, M. Bianchi, J. Wiebe, P. Hofmann, and J. Honolka. Topological insulator homojunctions including magnetic layers: The example of n-p type (n-qls Bi2Se3/Mn-Bi2Se3) heterostructures. *Appl. Phys. Lett.*, **108**(26), 262402, 2016

9. R. Tarasenko, **M. Vališka**, M. Vondráček, K. Horáková, V. Tkáč, K. Carva, P. Baláž, V. Holý, G. Springholz, V. Sechovský, and J. Honolka. Magnetic and structural properties of Mn-doped Bi2Se3 topological insulators. *Physica B*, **481**, 262267, 2016

10. Ch. Tabata, N. Miura, K.Uhlířová, **M. Vališka**, H. Saito, H. Hidaka, T. Yanagisawa, V.r Sechovský, and H. Amitsuka. Peculiar magnetism of UAu2Si2. *Phys. Rev. B*, **94**(21),214414, 2016

11. J. Pospíšil, P. Opletal, **M. Vališka**, Y. Tokunaga, A. Stunault, Y. Haga, N. Tateiwa, B. Gillon, F. Honda, T. Yamamura, V. Nižňanský, E. Yamamoto, and D. Aoki. Properties and collapse of the ferromagnetism in UCo(1-x)Ru(x)Al studied in single crystals. *J. Phys. Soc. Jpn.*, **85**(3), 034710, 2016

12. M. S. Henriques, D. I. Gorbunov, D. Kriegner, **M. Vališka**, A. V. Andreev, and Z. Matěj. Magneto-elastic coupling across the first-order transition in the distorted Kagome lattice antiferromagnet Dy3Ru4Al12. *J. Magn. Magn. Mater.*, **400**, 125129, 2016

13. **M. Vališka**, P. Opletal, J. Pospíšil, J. Prokleška, and V. Sechovský. Evolution of magnetism in UCoGe and UCoAl with Ru doping. *Adv. Nat. Sci.: Nanosci. Nanotechnol.*, **6**(1),015017, 2015

14. **M. Vališka**, J. Pospíšil, M. Diviš, J. Prokleška, V. Sechovský, and M. M. Abd-Elmeguid. Evolution of ferromagnetic and non-fermi-liquid states with doping: The case of Ru-doped UCoGe. *Phys. Rev. B*, **92**(4), 045114, 2015

15. **M. Vališka**, J. Pospíšil, A.Stunault, Y. Takeda, B. Gillon, Y. Haga, K. Prokeš, M. M. Abd-Elmeguid, G. Nénert, T. Okane, H. Yamagami, L. Chapon, A. Gukasov, A. Cousson, E. Yamamoto, and V. Sechovský. Gradual localization of 5f states in orthorhombic UTX ferromagnets:polarized neutron diffraction study of Ru substituted UCoGe. *J. Phys. Soc. Jpn.*, **84**(8), 084707, 2015

16. **M. Vališka**, J. Pospíšil, G. Nénert, A. Stunault, K. Prokeš, and V. Sechovský. Evolution of Magnetism in UCo,RuGe, *JPS Conference Proceedings. Journal of the Physical Society of Japan* **3**, 2014

17. **M. Vališka**, J. Pospíšil, G. Nénert, A. Stunault, K. Prokeš, and V. Sechovský. Magnetism in UCo0.88Ru0.12Ge studied by polarized neutrons. *Acta Phys. Pol. A*, **126**(1), 330, 2014

18. J. Valenta, J. Prchal, R. Khasanov, M. Kratochvílová, M. Míšek, **M. Vališka**, and V. Sechovský. Presence of parimagnetism in HoCo 2 under hydrostatic pressure. *J. Phys. Conf. Ser.*, **500**(18), 182041, 2014

19. **M.Vališka**, J. Pospíšil, J. Prokleška, M. Diviš, A. Rudajevová, I. Turek, and V. Sechovský. Influence of symmetry on Sm magnetism studied on SmIr2Si2 polymorphs. *J. Alloys Compd.*, **574**, 459 466, 2013

20. **M. Vališka**, J. Pospíšil, J. Prokleška, M. Diviš, A. Rudajevová, and V. Sechovský. Superconductivity in the YIr2Si2 and LaIr2Si2 polymorphs. *J. Phys. Soc. Jpn.*, **81**(10),104715, 2012.